Universiteit Utrecht

Department of Earth Sciences
Mantle dynamics and theoretical geophysics

On the implementation and benchmarking of a viscoelastic-plastic rheology in a long term tectonics code and its influence on subduction evolution.

Master's Thesis

by Loes Cornelis

Supervisors:
Dr. Cedric Thieulot
Prof. Dr. Wim Spakman

Utrecht, September 2016

Abstract

The rheology of the Earth is often assumed to be viscoplastic in numerical mantle-lithosphere models. Doing so, the possibly important elastic behaviour of the lithosphere is neglected. Several studies determining the influence of elasticity on subduction indicate that it is likely to play an important role in the cold, high-stress regions of the lithosphere. In order to study the influence of elasticity on subduction dynamics, a viscoelastic-plastic numerical code is developed in this work. A thorough overview of the theory behind a viscoelastic-plastic rheology is presented and issues that arise when implementing elasticity are discussed. These issues concern, for instance, the effect of using nodal versus elemental quantities and difficulties that arise due to the time dependence of elasticity. A new viscoelastic-plastic code is successfully developed and benchmarked extensively. Furthermore, the novel combination of elasticity and the field advection approach instead of the marker-in-cell method is studied. We find that the combination is a valid approach which can be applied on state-of-the art numerical models.

Acknowledgements

Contents

1 Introduction

Since the formulation of the theory of plate tectonics and evidence was found for the sinking of lithosphere into the mantle (through the observation of deep earthquakes), research on subduction zones has been a hot topic. Due to the fact that most processes in a subduction zone take place underneath the Earth's crust and that the timescales at which they take place span much longer than human lifespan, geological observations alone are not sufficient to understand these processes. Several methods to study the inner workings of subduction have been developed in the past decades.

Snapshots of the current thermal state of the mantle are made using seismic tomography. These indirect observations estimate the spatial configuration of a subducting plate and can be used as boundary conditions and constraints when modelling the subduction zones. Where mantle tomography and seismological imaging only provide information on the current state of the Earth, geodynamical modelling can be used to develop a dynamic and kinematic understanding of subduction processes.

The growth in computational power over the past decades has enabled the development of 2D and 3D numerical models with increasingly sophisticated methods to represent the Earths processes and kinematics with increasing accuracy. Realistically modelling subduction processes and producing fully self-sustainable plate tectonics remains, even after four decades of experience, challenging. This is for example due to computational difficulties arising from resolution problems, the large viscosity contrasts involved and unrealistic representations of domain boundaries (e.g. free surface, no slip). Problems also arise when describing the rheology of the materials involved in a subduction zone: the pressure and temperature dependence of materials has to be taken into account, as well as phase transitions and chemical reactions.

Although these material properties are not well constrained, their hypothetical values or ranges can be tested using numerical modelling. Using simple numerical models, the influence of physical parameters or material descriptions can be isolated which will result in estimated possible ranges which are thought to lead to Earthly conditions.

1.1 A general introduction to numerical modelling

The dynamics of the lithosphere and mantle can be described by solving the classical momentum conservation equation (1) and the energy or heat transport equation (2).

$$\nabla \cdot \sigma + \mathbf{f} = 0 \tag{1}$$

$$\rho c_p \left(\frac{\partial T}{\partial t} + \mathbf{v} \cdot \boldsymbol{\nabla} T \right) = \boldsymbol{\nabla} \cdot (k \boldsymbol{\nabla} T) + H \tag{2}$$

Here, $\boldsymbol{\sigma}$ represents the stress tensor and $\mathbf{f}$ the forcing component present in the system. This forcing term often represents the gravity acting upon density variations. ρ, c_p and k are respectively the material density, heat capacity and heat conductivity. H represents a thermal source/sink term, $\mathbf{v}$ the velocity and T the temperature. The momentum conservation equation and heat transport equation are solved under the following assumptions:

- The stress tensor is symmetrical due to the moment of equilibrium.

- The Boussinesq approximation is adopted enabling the neglection of density changes due to pressure variations.

- All inertial terms in the momentum conservation equation can be ignored due to the Prandtl number approaching infinity ($Pr \to \infty$).

- Mass conservation is assumed through the use of incompressibility of materials (3).

$$\nabla \cdot \mathbf{v} = 0 \tag{3}$$

Choices regarding the material properties and rheology and the assumptions made therein are an important contributor to the further development of the governing equations and greatly influence the results of the model.

The choice of rheology results in the use of different constitutive relations. For subduction modelling, viscous, viscoplastic, viscoelastic and viscoelastic-plastic rheologies are currently used. The use of a viscoplastic rheology is often adopted (e.g. (Solomatov and Moresi, 1996; Solomatov, 2004; Thieulot, 2011; Schellart and Moresi, 2013; Bello et al., 2015)). This rheological description is often chosen over a description including elasticity due to its simpler nature as it does not require the implementation of a stress memory of the material. In the past decades, the use of a viscoelastic or viscoelastic-plastic rheology has become more frequent and is now widely used (e.g. (Funiciello et al., 2003; Capitanio and Morra, 2012; Farrington et al., 2014; Fourel et al., 2014)) however, little is

known about the effect of incorporating elasticity (See Section 1.2 for a more thorough discussion). Besides the choice of deformation mechanism, one has to decide to incorporate the dependence of viscosity on temperature and stress (e.g. Newtonian or non-Newtonian).

Lastly a choice has to be made regarding the complexity of the model. Modelling the subduction process as realistically as possible on a large scale, is challenging and requires computational power currently not available. This means that highly realistic models are often used to study regional effects in a subduction zone such as the mantle wedge or fluid and melt transport. When modelling large-scale subduction dynamics, simplified models are used in order to keep the resolution of the model (and the size of the calculations) under control. This means that small details, local processes and petrological effects cannot be modeled. One thus has to decide whether to focus on high detail, small scale regional subduction tectonics, or on a simplified, large scale subduction zone.

1.2 The possible importance of elasticity in subduction modelling

In order to numerically model the Earth, the description of the deformation of its materials has to be described by either viscous, elastic, plastic or a combination of these three modes of deformation. When observed on a short timescale, seconds to centuries, the mantle exhibits elastic behaviour as is observed from the propagation of seismic waves through the mantle. However, when observed over the geological timescale the mantle is often assumed to behave viscous shown by the convection in the mantle on geological timescale. During numerical modelling of the mantle on long time scales, it is thus best characterized by a viscous material.

The lithosphere is often described as a rigid lid overlying the viscous mantle. This outer shell succumbs at yield stresses through brittle failure or creep mechanisms which are represented by a plastic rheology. An important characteristic of the lithosphere is its elastic response as is observed during flexure. A material can behave elastically when stresses are stored subsequently longer than the time of deformation. The lithosphere is thought to store stresses over millions of years (see Section 3.1) making the elastic response a possibly important part of the rheological description of the lithosphere as this time scale overlaps with the tectonic deformation time scale. Elasticity is often incorporated in studies on lithospheric surface deformation, but in mantle convection models which include the lithosphere elasticity is often neglected and the mantle-lithosphere system is described as viscoplastic. Billen (2008) justifies this simplification by stating that the the elastic response of the lithosphere and mantle can be ignored over long periods of time, greater than one million year. As previously mentioned, this assumption is valid for the mantle, but is possibly wrong where the lithosphere is considered as the time frame of the storage of stresses and the time of deformation overlaps. An overview of the research towards the role of elasticity in subduction modelling and mantle dynamics is given below.

1.3 Review on elasticity in a geodynamical setting

Elasticity is often incorporated in the rheological descriptions of geodynamical research while its influence is not studied (Morra and Regenauer-Lieb, 2006; Royden and Husson, 2006; Bonnardot et al., 2008; Capitanio et al., 2009; Capitanio and Morra, 2012). In contrast, several systematic studies towards the influence of elasticity on geodynamical modelling have been performed. Harder (1991); Moresi et al. (2002); Muhlhaus and Regenauer-Lieb (2005); Thielmann and Popov (2015) studied the influence of elasticity on mantle convection and showed that elasticity does not affect the convection style and velocity for Earth's range of parameters. However, they did find that the stress distribution in the overlying lid is significantly affected as it is distributed over a thicker layer in comparison to the viscous case. As the stress distribution plays an important role in subduction initiation, the use and prediction of a correct stress field is of utmost importance.

Kaus and Becker (2007); Furuichi et al. (2008) investigated the effect of elasticity on gravitational instabilities and concluded that elasticity can significantly speed up the growth of the instabilities but again, this effect is negligible for Earthly parameters. Kaus and Becker (2007) also found that incorporating elasticity leads to a significantly altered response and stress build-up in the overlying crust.

When considering subduction dynamics, the influence of elasticity on its evolution has been studied by Moresi et al. (2002); Funiciello et al. (2003); Fourel et al. (2014); Farrington et al. (2014). Moresi et al. (2002) showed that the incorporation of elasticity leads to a more realistic slab geometry. The sinking slab is then straighter and has a backward rolling evolution. Funiciello et al. (2003) studied the role of rheology on slab dynamics with a specific focus on elasticity. They found that elasticity is required to give long term bending strength to the slab, to obtain realistic trench retreat velocities and to produce a realistic trench profile. They concluded that elasticity stabilizes the subduction process and is a necessary ingredient to produce slab coherency. Fourel et al. (2014) and Farrington et al. (2014) focused on the effect of elasticity on slab bending and unbending. Both groups found that the storage of elastic stresses plays an important role in the energy transfer in the slab and facilitates bending and unbending.

9

The discussion above highlights the probable importance of elasticity in subduction dynamics. It has been shown to be negligible in the hot mantle during convection, but an important ingredient for accurate predictions of lithospheric stresses. Funiciello et al. (2003); Fourel et al. (2014); Farrington et al. (2014) showed that it cannot be ignored in the bending and unbending region of a subduction zone while it can be ignored in the straight down going part of the slab (Funiciello et al., 2003). These conclusions indicate that elasticity is negligible in hot regions such as the mantle and low stress areas in the subducting slab and is likely to play an important role in cold parts of the lithosphere and the down going slab, as well as in locations with high stresses and strain rates.

Thus the incorporation of elasticity in lithosphere and mantle modelling is an important ingredient towards understanding geodynamics processes. The Mantle Dynamics group at the University of Utrecht currently does not posses a model which includes elasticity and the goal of this research is thus to develop a model that includes a viscoelastic-plastic rheology, such that the contribution of elasticity can be studied at this institute. Besides this, the combination of elasticity and the field advection approach is studied for the first time to enable the implementation of elasticity in codes that are not based on the particle-in-cell method. Because no research has been done towards the implementation of elasticity in field-based codes, it is unknown whether the combination is possible, preventing the implementation of elasticity in codes that are based on the field advection approach such as ASPECT (Bangerth et al., 2016b).

This research has a threefold purpose:

- To outline the theory and implementation concerning a viscoelastic-plastic code

- Developing and extensively benchmarking a viscoelastic-plastic model

- Study the combination of elasticity and the field advection approach

This work presents an overview of the theory behind viscoelastic-plastic rheologies (Section 3 and 4) and presents solutions concerning the issues that arise when implementing elasticity in an existing viscoplastic code (Section 5). Furthermore, Section 6 discusses the theory behind the field advection approach and the combination of elasticity and the field approach is researched in Section 8. Lastly, the viscoelastic-plastic implementation is thoroughly benchmarked in Section 9.
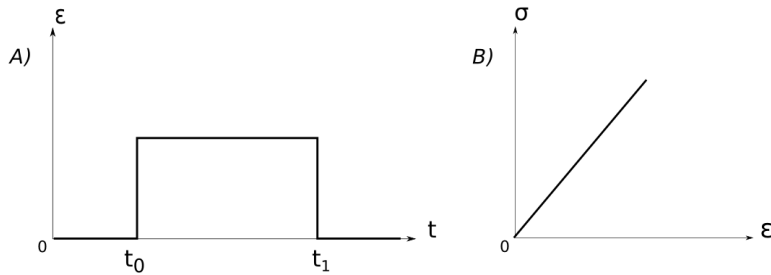
Figure 1: *Elastic behaviour of a material subjected to a stress below the yield strength. a) strain-time diagram showing the arising deformation due to the application of a constant stress applied at t_0 and removed at t_1, b) the linear relation between stress and strain. Adapted from (Ranalli, 1995)*

.

2   A general introduction to elasticity

Elastic behaviour of a material is characterized by a linear instantaneous deformation during the application of the stress and a complete recovery after the removal of the applied stress (Figure 1)(Ranalli, 1995). When a stress is applied which is greater than the yield stress of the material, the elastic behaviour ceases and material failure occurs in the form of ductile or brittle deformation (e.g. Ranalli, 1995).

Ideal elastic behaviour can be described by *Hooke's law.*

$$\sigma_{ij} = C_{ijkl}\varepsilon_{kl} \tag{4}$$

where the Einstein summation convention is assumed, σ_{ij} represents the stress tensor, ε_{kl} the strain tensor and C_{ijkl} the elasticity tensor with 81 elastic coefficients.

When considering an isotropic material, the elastic properties are independent of direction, and the number of independent elastic coefficients is reduced to two resulting in the following constitutive relation for elasticity:

$$\sigma_{ij} = \lambda\varepsilon_{kk}\delta_{ij} + 2\mu\varepsilon_{ij} \tag{5}$$

with δ_{ij} the Kronecker delta, and λ and μ elastic parameters called the *Lamé constants* of which μ represents the elastic shear modulus of a material.

Isotropic materials exhibit two modes of strain. Volumetric strain resulting from normal stresses and shear strain resulting from shear stresses. The total stress σ_{ij} can be separated in these two parts by defining a normal isotropic stress σ_0 and a deviatoric shear stress τ_{ij}.

$$\tau_{ij} = \sigma_{ij} - \frac{1}{3}\sigma_{kk}\delta_{ij} = 2\mu(\varepsilon_{ij} - \frac{1}{3}\varepsilon_{kk}\delta_{ij}) \tag{6}$$

Equation (5) and (6) can be combined to derive a relation between the deviatoric stress and the deviatoric shear strain $\varepsilon'_{ij} = \varepsilon_{ij} - \frac{1}{3}\varepsilon_{kk}\delta_{ij}$. The following relation is then obtained:

$$\tau_{ij} = 2\mu\varepsilon'_{ij} \tag{7}$$

The normal isotropic stress $\sigma_0 = \sigma_{kk}$ is related to the normal strain by

$$\sigma_0 = \left(\lambda + \frac{2}{3}\mu\right)\varepsilon_{kk} \tag{8}$$

3   A numerical formulation for viscoelasticity

The existing viscoplastic FORTRAN code ELEFANT (Thieulot, 2014) is adapted in order to incorporate elastic behaviour of materials. This is done by using a viscoelastic rheology which can model both the viscous and elastic response of materials. ELEFANT is a finite element lithosphere and mantle dynamics code which solves the classical momentum conservation equation (9) in order to find the velocity ($\mathbf{v}$) and pressure (p) fields under the assumption of incompressibility $\nabla \cdot \mathbf{v} = 0$ to account for mass conservation.

$$\nabla \cdot \sigma + \rho\mathbf{g} = \mathbf{0} \tag{9}$$

Here, $\boldsymbol{\sigma}$ represents the stress tensor and $\rho\mathbf{g}$ the body force term in the form of gravity. Due to the Prandtl number $Pr \to \infty$, all inertial terms can be neglected.

When solving equation (9), a relation between the stress and velocity is needed in order to find the primary variable, the velocity $\mathbf{v}$. This relation will be derived in Section 3.2 after an introduction on viscoelasticity is given in the following section.
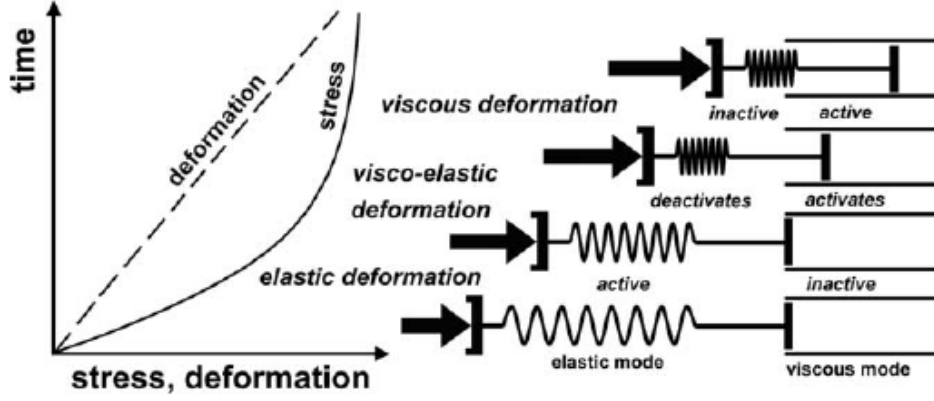
Figure 2: *The viscoelastic Maxwell model defined as an elastic and viscous element connected in series. The rheological behaviour of the material while undergoing a linearly increasing deformation is shown. The magnitude of the applied stress is shown by the length of the arrows. From bottom to top: The initial response of the material is elastic as the spring is shortened. The viscous component then activates and becomes the dominant deformation mechanism causing a stabilization of the stress. This is shown in the left figure. From Gerya (2009).*

3.1 Viscoelasticity

For the implementation of a viscoelastic rheology, an approach introduced by Moresi et al. (2002) is used. This method has been previously used by e.g. Moresi et al. (2007); Gerya and Yuen (2007); Beuchert and Podladchikov (2010); Kaus (2010); Thielmann and Popov (2015); von Tscharner and Schmalholz (2015). Moresi et al. (2002) uses the Maxwell viscoelastic model which assumes that the behaviour of a viscoelastic model can be described by an elastic and viscous element connected in series (shown in Figure 2). The strain rate tensor is therefore defined as a summation of the elastic part of the strain rate $\dot{\boldsymbol{\varepsilon}}^e$ and the viscous strain rate tensor $\dot{\boldsymbol{\varepsilon}}^v$.

$$\dot{\boldsymbol{\varepsilon}} = \dot{\boldsymbol{\varepsilon}}^e + \dot{\boldsymbol{\varepsilon}}^v \tag{10}$$

A strain rate tensor component is defined as:

$$\dot{\varepsilon}_{ij} = \frac{1}{2}\left(\frac{\partial v_i}{\partial x_j} + \frac{\partial v_j}{\partial x_i}\right) \tag{11}$$

with v_i a velocity component. Equation (11) can again be split into an isotropic and deviatoric part.

$$\dot{\varepsilon}'_{ij} = \dot{\varepsilon}_{ij} - \frac{1}{3}\dot{\varepsilon}_{ii}\delta_{ij} \tag{12}$$

As we assumed incompressibility in our model, ($\nabla \cdot \mathbf{v} = 0$, $\dot{\varepsilon}_{ii} = 0$), the expression for viscoelasticity can be simplified and deformation can be solely described by deviators. (Beuchert and Podladchikov, 2010). It has already been shown that for an elastic material, the deviatoric stress is related to the deviatoric strain by the shear modulus μ (7). For a Newtonian viscous medium, the shear viscosity η relates the deviatoric strain rate to the deviatoric stress.

$$\dot{\varepsilon}'_{ij} = \frac{\tau_{ij}}{2\eta} \tag{13}$$

Substituting (7) and (13) into (10), the expression for the total deviatoric strain becomes:

$$\dot{\varepsilon}'_{ij} = \dot{\varepsilon}'^{e}_{ij} + \dot{\varepsilon}'^{v}_{ij} = \frac{\dot{\tau}_{ij}}{2\mu} + \frac{\tau_{ij}}{2\eta} \tag{14}$$

with $\dot{\tau}_{ij}$ the deviatoric stress rate. This stress rate arises due to the fact that an expression for the elastic strain rate is needed (as given for the viscous case). However for the elastic case, there is only a relation between the stress and strain. In order to obtain a strain rate dependence, a time derivation is made of equation (7) to obtain an expression for the elastic strain rate.

The definition for the deviatoric stress rate is often chosen to be independent of reference frame making it objective. Doing so, the stress rate implicitly accounts for whole body rotation which would change the orientation of the stress tensor. In other words, the stress tensor co-rotates with the deformation the material

undergoes, making manual rotation of the stress tensor redundant. Multiple definitions for the objective stress rates exist. The Jaumann corotational stress rate (15) is often used in geodynamic modelling because of its simplicity and the fact that it does not affect the deviatoric properties of the stress tensor which simplify the rheological expressions used (Moresi et al., 2002; Gerya and Yuen, 2007; Farrington et al., 2014; von Tscharner and Schmalholz, 2015). It is given by:

$$\dot{\tau}_{ij} = \frac{D\tau_{ij}}{Dt} + (\tau_{ik}\omega_{kj} - \omega_{ik}\tau_{kj}) \tag{15}$$

Here, $\frac{D\tau_{ij}}{Dt}$ represents the material derivative of τ_{ij} and $\boldsymbol{\omega}$ represents the material spin tensor (the rotation rate, see Appendix A.1). The rotation rate is anti-symmetric and has a zero trace ($\omega_{ii} = 0$). The rotation term ($\tau_{ik}\omega_{kj} - \omega_{ik}\tau_{kj}$) account for the whole body rotation of the tensor. This term needs to be considered only when large deformation occurs (Muhlhaus and Regenauer-Lieb, 2005).

The Jaumann corotational stress rate expression does however have a disadvantage. It has been shown to exhibit spurious softening when the level of stress reaches the same order of magnitude as the shear modulus of the material (Muhlhaus and Regenauer-Lieb, 2005; Beuchert and Podladchikov, 2010). This problem is bypassed when using a material rheology which includes plastic yielding or when using Earthly viscosity and shear modulus values. Then the stress levels will not reach the order of magnitude equal to the shear modulus and no softening arises(Beuchert and Podladchikov, 2010).

$$\omega_{ij} = \frac{1}{2}\left(\frac{\partial v_i}{\partial x_j} - \frac{\partial v_j}{\partial x_i}\right) \tag{16}$$

A viscoelastic material can behave both elastically and viciously. Its response to an applied stress is dependent on the material properties and can be found using the Maxwell time (t_M) of said material. This material constant is defined as the ratio of the material viscosity and shear modulus (17).

$$t_M = \frac{\eta}{\mu} \tag{17}$$

A material can behave elastic when elastic stresses are stored long enough to be released when the applied stresses decrease or cease to exist. The stored stresses in the elastic material can then subsequently be released resulting in an elastic response. The timeframe of stress storage is captured by the Maxwell time. It gives a measure of the duration of relaxation of the stored elastic stresses to $\frac{1}{e}$ of its original value (Beuchert and Podladchikov, 2010). This means that for a Maxwell time significantly larger than the time of deformation, stresses are stored over a longer period than the time of deformation meaning they can be released when deformation ceases. This results in an elastic response of the material. Conversely, in materials whose Maxwell time is shorter than the deformation time, stresses are not preserved resulting in an inelastic viscous behaviour of the material. The behaviour of the mantle and lithosphere can be simplified and described by a viscoelastic rheology which exhibits the behaviour described above.

The lithosphere has, for example, a viscosity of $\sim 10^{25}$ Pa s and a shear modulus of $\sim 10^{11}$ Pa resulting in a Maxwell time of $\sim$3.2 Myrs. This Maxwell time surpasses most geological deformation timescales meaning that the lithosphere behaves elastically. This is observed during flexure of the lithosphere. The mantle, which has a shear modulus of $\sim 10^{11}$ Pa and a viscosity of $\sim 10^{21}$ Pa s, has a Maxwell time which is considerably smaller than that of the lithosphere, namely 310 yr. The process of thermal convection takes place over much longer timescales thus resulting in a viscous behaviour since the stored stresses dissipate before they can be released. Note that seismic waves originating from the lithosphere travel through the mantle on timescales in the order of seconds which is smaller than the Maxwell time. The response of the mantle to the seismic wave propagation is therefore elastic.

3.2   Numerical formulation

The material derivative of the stress in the material derivative in (15) can be approximated by a forward difference scheme. Combining this with the definition of the Jaumann derivative, and the fact that when using a Lagrangian approach, the advection term present in the material derivative can be neglected (von Tscharner and Schmalholz, 2015) this leads to the following definition of the objective stress rate:

$$\dot{\boldsymbol{\tau}}^{t+\Delta t} \approx \frac{\boldsymbol{\tau}^{t+\Delta t} - \boldsymbol{\tau}^t}{\Delta t} - \boldsymbol{\omega}^t\boldsymbol{\tau}^t + \boldsymbol{\tau}^t\boldsymbol{\omega}^t \tag{18}$$

$\boldsymbol{\tau}^{t+\Delta t}$ and $\boldsymbol{\tau}^t$ represent the deviatoric stress tensor at time $t + \Delta t$ and t. $\boldsymbol{\omega}^t$ represents the rotation rate tensor at time t.

Substituting equation (18) into (14) when evaluated at time $t + \Delta t$, the strain rate at that time $\dot{\varepsilon}^{t+\Delta t}$ can be expressed as follows:

$$\dot{\varepsilon}^{t+\Delta t} = \frac{1}{2\mu}\left(\frac{\boldsymbol{\tau}^{t+\Delta t} - \boldsymbol{\tau}^t}{\Delta t} - \boldsymbol{\omega}^t\boldsymbol{\tau}^t + \boldsymbol{\tau}^t\boldsymbol{\omega}^t\right) + \frac{\boldsymbol{\tau}^{t+\Delta t}}{2\eta} \tag{19}$$

Where the primes which indicate the deviatoric strain rate has been dropped. All strain rates used below represent the deviatoric strain rate. Rearranging (19) we can find an expression for the deviatoric stress.

$$\boldsymbol{\tau}^{t+\Delta t} = \frac{2\mu\Delta t}{\left(1 + \frac{\mu\Delta t}{\eta}\right)}\,\dot{\boldsymbol{\varepsilon}}^{t+\Delta t} + \frac{1}{\left(1 + \frac{\mu\Delta t}{\eta}\right)}\boldsymbol{\tau}^t + \frac{\Delta t}{\left(1 + \frac{\mu\Delta t}{\eta}\right)}\left(\boldsymbol{\omega}^t\boldsymbol{\tau}^t - \boldsymbol{\tau}^t\boldsymbol{\omega}^t\right) \tag{20}$$

The expression for the deviatoric stress can be simplified by defining the effective elastic viscosity η_{eff}:

$$\eta_{eff} = \frac{\mu\Delta t}{1 + \frac{\mu\Delta t}{\eta}} = \eta\frac{\Delta t}{\Delta t + \frac{\eta}{\mu}} \tag{21}$$

where $t_M = \eta/\mu$ is captured in the effective viscosity. Substituting equation (21) in (20) leads to the following expression for the deviatoric stress:

$$\boldsymbol{\tau}^{t+\Delta t} = 2\eta_{eff}\,\dot{\boldsymbol{\varepsilon}}^{t+\Delta t} + \frac{\eta_{eff}}{\mu\Delta t}\,\boldsymbol{\tau}^t + \frac{\eta_{eff}}{\mu}\left(\boldsymbol{\omega}^t\boldsymbol{\tau}^t - \boldsymbol{\tau}^t\boldsymbol{\omega}^t\right) \tag{22}$$

When comparing this obtained relation between the stress and the strain rate to the relation corresponding to the viscous case (13), it can be seen that for the viscoelastic relation, a stress memory term has been added to the relation as well as a stress rotation part.

In order to simplify the implementation process, the symmetry of the stress tensor is exploited to express the stress tensor as a vector. Note that the following derivation is done for a 2D configuration. The same reasoning can be applied to obtain 3D relations.

$$\begin{pmatrix}\sigma_{xx}\\\sigma_{yy}\\\sigma_{xy}\end{pmatrix} = \begin{pmatrix}-p\\-p\\0\end{pmatrix} + \begin{pmatrix}\tau_{xx}\\\tau_{yy}\\\tau_{xy}\end{pmatrix} \tag{23}$$

Equation (22) can then be used while assuming the material to be weakly compressible ($p = -\lambda\left(\dot{\varepsilon}_{xx} + \dot{\varepsilon}_{yy}\right)$ with λ the penalty factor) and simplifying the rotation term ($\boldsymbol{\omega}^t\boldsymbol{\tau}^t - \boldsymbol{\tau}^t\boldsymbol{\omega}^t$), equation (23) becomes

$$\begin{pmatrix}\sigma_{xx}^{t+\Delta t}\\\sigma_{yy}^{t+\Delta t}\\\sigma_{xy}^{t+\Delta t}\end{pmatrix} = \lambda\begin{pmatrix}\dot{\varepsilon}_{xx}^{t+\Delta t} + \dot{\varepsilon}_{yy}^{t+\Delta t}\\\dot{\varepsilon}_{xx}^{t+\Delta t} + \dot{\varepsilon}_{yy}^{t+\Delta t}\\0\end{pmatrix} + 2\eta_{eff}\begin{pmatrix}\dot{\varepsilon}_{xx}^{t+\Delta t}\\\dot{\varepsilon}_{yy}^{t+\Delta t}\\\dot{\varepsilon}_{xy}^{t+\Delta t}\end{pmatrix} + \frac{\eta_{eff}}{\mu\Delta t}\begin{pmatrix}\tau_{xx}^t\\\tau_{yy}^t\\\tau_{xy}^t\end{pmatrix} + \frac{\eta_{eff}}{\mu}\begin{pmatrix}2\,\omega_{xy}^t\tau_{xy}^t\\-2\,\omega_{xy}^t\tau_{xy}^t\\\omega_{xy}^t\left(\tau_{yy}^t - \tau_{xx}^t\right)\end{pmatrix} \tag{24}$$

Substituting Equation (11), this becomes:

$$\begin{pmatrix}\sigma_{xx}^{t+\Delta t}\\\sigma_{yy}^{t+\Delta t}\\\sigma_{xy}^{t+\Delta t}\end{pmatrix} = \left[\lambda\begin{pmatrix}1 & 1 & 0\\1 & 1 & 0\\0 & 0 & 0\end{pmatrix} + \eta_{eff}\begin{pmatrix}2 & 0 & 0\\0 & 2 & 0\\0 & 0 & 1\end{pmatrix}\right]\begin{pmatrix}\partial u^{t+\Delta t}/\partial x\\\partial v^{t+\Delta t}/\partial y\\\partial u^{t+\Delta t}/\partial y + \partial v^{t+\Delta t}/\partial x\end{pmatrix} \tag{25}$$
$$+ \frac{\eta_{eff}}{\mu\Delta t}\left[\begin{pmatrix}\tau_{xx}^t\\\tau_{yy}^t\\\tau_{xy}^t\end{pmatrix} + \Delta t\begin{pmatrix}2\,\omega_{xy}^t\tau_{xy}^t\\-2\,\omega_{xy}^t\tau_{xy}^t\\\omega_{xy}^t\left(\tau_{yy}^t - \tau_{xx}^t\right)\end{pmatrix}\right]$$

This can be written as:

$$\begin{pmatrix}\sigma_{xx}^{t+\Delta t}\\\sigma_{yy}^{t+\Delta t}\\\sigma_{xy}^{t+\Delta t}\end{pmatrix} = [\lambda\mathbf{K} + \eta_{eff}\mathbf{C}]\begin{pmatrix}\partial u^{t+\Delta t}/\partial x\\\partial v^{t+\Delta t}/\partial y\\\partial u^{t+\Delta t}/\partial y + \partial v^{t+\Delta t}/\partial x\end{pmatrix} + \frac{\eta_{eff}}{\mu\Delta t}\left[\mathbf{T}^t + \Delta t\mathbf{R}^t\right] \tag{26}$$

Where $\mathbf{T}^t$ represents the stress memory vector and $\mathbf{R}^t$ the Jaumann rotation vector.

3.3   Finite Element implementation

In order to implement the viscoelastic rheology in a finite element code, the Galerkin method is applied to equation (9), for the case $f_i = \rho g_i$.

$$\int_{\Omega_e} \left(\nabla \cdot \sigma_{ij}\right) N_i d\Omega = \int_{\Omega_e} f_i N_i d\Omega \tag{27}$$

14

Where $\Omega_{(e)}$ represents the element volume (3D) or surface (2) and N_i the basis functions corresponding to the Galerkin method. This expression can be integrated by parts, and after dropping the surface term (set to zero by boundary conditions) equation (27) becomes

$$\int_{\Omega_e} \nabla N_i \cdot \sigma_{ij} d\Omega = \int_{\Omega_e} f_i N_i d\Omega \tag{28}$$

The expression for the deviatoric stress (26) can then be substituted in equation (28). In the the finite element method the velocity field is approximated by $\mathbf{u}(x,y) = \sum_i N_i(x,y)\mathbf{u}_i$, making the velocity spatially independent. The velocity is then captured in vector $\mathbf{V}$ to obtain the following expression:

$$\int_{\Omega_e} \mathbf{B}^T \left\{ [\lambda\mathbf{K} + \eta_{eff}\mathbf{C}]\mathbf{B}\mathbf{V}^{t+\Delta t} + \frac{\eta_{eff}}{\mu\Delta t}\left[\mathbf{T}^t + \Delta t\mathbf{R}^t\right] \right\} d\Omega = \int_{\Omega_e} \mathbf{N}_f d\Omega \tag{29}$$

where $\mathbf{N}_f = f_i N_i$ represents the forcing term. Matrix $\mathbf{B}$ is defined as follows:

$$\mathbf{B} = \nabla N_i = \begin{pmatrix} \frac{\partial N_i}{\partial x} & 0 \\ 0 & \frac{\partial N_i}{\partial y} \\ \frac{\partial N_i}{\partial y} & \frac{\partial N_i}{\partial x} \end{pmatrix} \tag{30}$$

All terms from time t are then moved to the right hand side. Due to the independence of space coordinates of the velocity vector, it can be extracted from the integral. This yields

$$\left\{ \int_{\Omega_e} \mathbf{B}^T [\lambda\mathbf{K} + \eta_{eff}\mathbf{C}]\mathbf{B}d\Omega \right\} \mathbf{V}^{t+\Delta t} = \int_{\Omega_e} \mathbf{N}_f - \frac{\eta_{eff}}{\mu\Delta t}\mathbf{B}^T\left[\mathbf{T}^t + \Delta t\mathbf{R}^t\right]d\Omega \tag{31}$$

$$\left\{ \int_{\Omega_e} \lambda\mathbf{B}^T\mathbf{K}\mathbf{B}\,d\Omega + \int_{\Omega_e} \eta_{eff}\mathbf{B}^T\mathbf{C}\mathbf{B}\,d\Omega \right\} \mathbf{V}^{t+\Delta t} = \int_{\Omega_e} \mathbf{N}_f - \frac{\eta_{eff}}{\mu\Delta t}\mathbf{B}^T\left[\mathbf{T}^t + \Delta t\mathbf{R}^t\right]d\Omega \tag{32}$$

which can be used in the finite element part of the code to solve for the velocity field. It can be seen that the right hand side contains the stress memory terms which act as an additional forcing besides the gravity (N_f). Equation (32) can be implemented in the finite element code.

4 A viscoelasto-plastic rheology

The low temperature rocks in the lithosphere deform by brittle failure when a stress above their yield strength is applied. In order to represent this deformation mechanism, a plastic formulation is often adopted.

Plastic deformation is characterized by a nonlinear viscosity which is adapted when local stress values exceed the prescribed yield stress τ_{yield}. The yield stress is often expressed using the yield criterion F which is dependent on the (local) stress, the pressure (P) and material parameters such as the cohesion and the angle of internal friction.

$$F(\boldsymbol{\tau}, P, c, \phi, ...) = 0 \tag{33}$$

When the yield criterion is met ($F \geq 0$), the viscosity is locally adapted to the plastic viscosity η_p to bring the accumulated stress back to the yield stress (F back to zero) and to ensure no stress levels higher than the yield stress are accumulated. For a purely plastic case, the plastic viscosity is found by

$$\eta_p = \frac{\tau_{yield}}{2\dot{\varepsilon}_{II}} \tag{34}$$

Here $\dot{\varepsilon}_{II}$ represents the second invariant of the strain rate

$$\dot{\varepsilon}_{II} = \sqrt{\frac{1}{2}\dot{\varepsilon}_{ij}\dot{\varepsilon}_{ij}} \tag{35}$$

4.1 Numerical formulation of viscoelasto-plasticity

In order to incorporate plastic failure in a viscoelastic code, the expression for the total strain rate (10), is extended by introducing a plastic strain rate part $\dot{\boldsymbol{\varepsilon}}_p$.

$$\dot{\boldsymbol{\varepsilon}} = \dot{\boldsymbol{\varepsilon}^e} + \dot{\boldsymbol{\varepsilon}^v} + \dot{\boldsymbol{\varepsilon}^p} \tag{36}$$

The definitions of the elastic and viscous part are equal to the viscoelastic formulation. The plastic strain rate is described by the plastic flow rule (Moresi et al., 2003; Gerya, 2009).

$$\begin{cases} \dot{\boldsymbol{\varepsilon}^p} = 0 & \text{for } \tau_{II} < \tau_{yield} \\ \dot{\boldsymbol{\varepsilon}^p} = \chi \frac{\tau_{yield}}{2\tau_{II}} & \text{for } \tau_{II} \geq \tau_{yield} \end{cases} \tag{37}$$

where τ_{II} is the second invariant of the stress tensor and χ the unknown plastic multiplier. The second invariant of the stress is defined as

$$\tau_{II} = \sqrt{\frac{1}{2}\tau_{ij}\tau_{ij}} \tag{38}$$

The adopted method for the implementation of plasticity does not affect the formulation and behaviour of viscoelastic materials while stress levels are below the yield stress. This is ensured by the plastic strain rate $\dot{\boldsymbol{\varepsilon}}_p$ equalling zero while the material has not reached the yield stress reducing equation (36) to equation (10).

At $\tau_{II} = \tau_{yield}$, equations (36) and the non-zero part of (37) are combined to include plastic behaviour. Following the same steps leading to equation (19), the following expression for the deviatoric stress for a viscoelasto-plastic rheology is obtained.

$$\boldsymbol{\tau}^{t+\Delta t} = 2\eta'\dot{\boldsymbol{\varepsilon}}^{t+\Delta t} + \frac{\eta'}{\mu\Delta t}\boldsymbol{\tau}^t + \frac{\eta'}{\mu}\left(\boldsymbol{\omega}^t\boldsymbol{\tau}^t - \boldsymbol{\tau}^t\boldsymbol{\omega}^t\right) \tag{39}$$

with η' defined as

$$\eta' = \begin{cases} \eta_{eff} = \eta\dfrac{\Delta t}{\Delta t + \eta/\mu} & \text{for } \tau_{II} < \tau_{yield} \\ \dfrac{\eta\mu\Delta t\tau_{yield}}{\eta\tau_{yield} + \mu\Delta t\tau_{yield} + \chi\eta\mu\Delta t} & \text{for } \tau_{II} \geq \tau_{yield} \end{cases} \tag{40}$$

The upper case characterises viscoelastic behaviour as used in Section 3.2. The viscosity η_{eff} equals the effective viscosity as defined in equation (21). The lower definition for η' is only used when plastic yielding occurs. In both equations, η represents the prescribed material viscosity. As χ is an unknown material parameter, it is difficult to find the appropriate value for η'.

An alternative method to find the appropriate viscosity exploits the fact that after the stresses have surpassed the threshold of the yield stress, the viscosity η' is adapted to bring them back to the yield value ($\tau_{II} = \tau_{yield}$). This results in the following expression (derived from (39)):

$$\tau_{yield} = \eta'\left[2\dot{\varepsilon}_{II} + \frac{1}{\mu\Delta t}\tau_{II}^{old} + \frac{1}{\mu}r_{II}^{old}\right] \quad \text{for} \quad \tau_{II} = \tau_{yield} \tag{41}$$

$$\text{(42)}$$

where r_{II} represents the second invariant of $\boldsymbol{r} = \boldsymbol{\omega}\boldsymbol{\tau} - \boldsymbol{\tau}\boldsymbol{\omega}$. τ_{II}^{old} and r_{II}^{old} are the second invariant of the stress and rotation tensor from the previous time step. The expression of the plastic viscosity then becomes

$$\eta' = \frac{\tau_{yield}}{2\dot{\varepsilon}_{II} + \frac{1}{\mu\Delta t}\tau_{II}^{old} + \frac{1}{\mu}r_{II}^{old}} \tag{43}$$

Substituting this expression in equation (39) and simplifying the equation leads to the following expression for the deviatoric stress

$$\boldsymbol{\tau}^{t+\Delta t} = \frac{\tau_{yield}}{2\dot{\varepsilon}_{II}^{t+\Delta t}} \cdot \left(\mu\Delta t + \frac{\tau_{II}^{t} + \Delta t\ r_{II}^{t}}{2\dot{\varepsilon}_{II}^{t+\Delta t}}\right)^{-1} \left[2\mu\Delta t\ \dot{\boldsymbol{\varepsilon}}^{t+\Delta t} + \boldsymbol{\tau}^{t} + \Delta t\ \mathbf{r}^{t}\right] \tag{44}$$

This expression can be simplified by assuming that after reaching the yield stress, no more stress is accumulated due to the failure of the material and the second invariant of the stress is thus constant $\frac{D\tau_{II}}{Dt} = 0$ (Gerya, 2010) and at yield value. Therefore

$$\tau_{II}^{t} + \Delta t\ r_{II}^{t} = \tau_{yield} \tag{45}$$

Defining the (viscoelastic-)plastic viscosity η_{vep} as follows (equal to the purely plastic or viscoplastic definition)

$$\eta_{vep} = \frac{\tau_{yield}}{2\dot{\varepsilon}_{II}^{t+\Delta t}} \tag{46}$$

and substituting (45) and (46) in equation (44) leads to the final expression for the deviatoric stress tensor.

$$\boldsymbol{\tau}^{t+\Delta t} = 2\eta_{vep}\dot{\varepsilon}^{t+\Delta t}\frac{\mu\Delta t}{\mu\Delta t + \eta_{vep}} + \frac{\eta_{vep}}{\mu\Delta t + \eta_{vep}}\left[\boldsymbol{\tau}^{t} + \Delta t\left(\boldsymbol{\omega}^{t}\boldsymbol{\tau}^{t} - \boldsymbol{\tau}^{t}\boldsymbol{\omega}^{t}\right)\right] \tag{47}$$

The derived expression in (47) can be generalized in order for it to be used during non-plastic deformation.

$$\boldsymbol{\tau}^{t+\Delta t} = 2\eta'\dot{\varepsilon}_{II}^{t+\Delta t}\frac{\mu\Delta t}{\mu\Delta t + \eta'} + \frac{\eta'}{\mu\Delta t + \eta'}\left[\boldsymbol{\tau}^{t} + \Delta t\left(\boldsymbol{\omega}^{t}\boldsymbol{\tau}^{t} - \boldsymbol{\tau}^{t}\boldsymbol{\omega}^{t}\right)\right] \tag{48}$$

where

$$\eta' = \begin{cases} \eta & \text{for } \tau_{II} < \tau_{yield} \quad \text{(viscoelastic case)} \\ \eta_{vep} = \frac{\tau_{yield}}{2\dot{\varepsilon}_{II}} & \text{for } \tau_{II} \geq \tau_{yield} \quad \text{(plastic case)} \end{cases} \tag{49}$$

Equation (48) is equal to (22) for the upper case where no yielding is present. A viscoelastic rheology can thus be modelled by setting an infinitely high yield stress ensuring the bottom criterion is never met. A viscoplastic rheology can be modelled using this formulation by setting the elastic shear modulus $\mu \to \infty$ reducing (48) to (13).

4.2   Implementation of viscoelasto-plasticity

Since the value of the viscosity η' depends on the strain rate, which in turn depends on the used viscosity to solve for the velocity field, non-linear iterations are needed to redistribute stress and focus deformation along the yielding surfaces (the numerical fault planes). The number of iterations is determined by the Euclidean norm of the difference in the velocity field between two subsequent iterations. Once this difference decreases below the error tolerance ϵ, the non-linear iteration loop is exited.

$$\left\|\mathbf{v}^{i} - \mathbf{v}^{i-1}\right\| < \epsilon \tag{50}$$

The schematics of the non-linear iteration loop is given in Figure 3. First, the second invariant of the strain rate and the stress are calculated on the markers. Each marker is then checked for yielding after which viscosity is either recalculated using τ_{yield} and ε_{II} or kept at its prescribed value (49). The viscosity of the markers is interpolated to the nodal points and the finite element expressions are solved to obtain the velocity field. The obtained velocity field is then tested for convergence using (50). If no convergence is reached, the loop is continued recalculating a new strain rate invariant using the newly calculated velocity field. Iterations are repeated until convergence is reached. The non-linear iteration loop is then exited. The implementation of the viscoelasto-plasticity is benchmarked in Section 9.
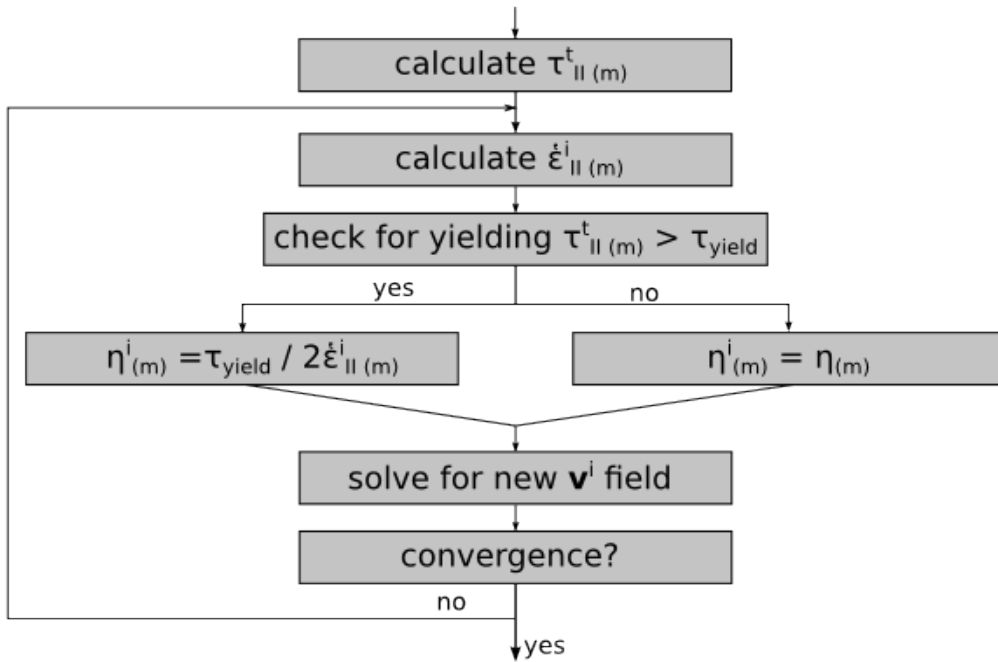
17

Figure 3: *A schematic diagram of the non-linear iteration loop used to obtain the plastic viscosity of the markers.*

4.3 Differences in formulation

As plasticity is an approximate description of failure of brittle material, no unique or correct approach exists in order to implement plasticity. There are therefore differences in the implementations that have previously been used. The approach presented in the previous section has been derived following the method from Gerya (2010). The derivation of expression (39) is equal to the method from Moresi et al. (2002) which obtain the same expression for the stress and plastic viscosity. The approach taken afterwards is however, different. Where Gerya (2010) and our method state that the plastic viscosity can be calculated using (43), Moresi et al. (2002) defines the plastic viscosity as

$$\eta' = \frac{\tau_{yield}}{2\dot{\varepsilon}_{II}^{eff}} \tag{51}$$

with $\dot{\varepsilon}_{II}^{eff}$, the second invariant of the effective strain rate. This effective strain rate is defined as

$$\dot{\varepsilon}^{eff} = \dot{\varepsilon}^{t+\Delta t} + \frac{1}{2\mu\Delta t}\boldsymbol{\tau}^t + \frac{1}{2\mu}\left(\boldsymbol{\omega}^t\boldsymbol{\tau}^t + \boldsymbol{\tau}^t\boldsymbol{\omega}^t\right) \tag{52}$$

so that equation (39) can be written as

$$\boldsymbol{\tau}^{t+\Delta t} = 2\eta'\dot{\boldsymbol{\varepsilon}}^{eff} \tag{53}$$

Comparing (43) and (51), it becomes clear that the only difference in the method lies in the definition of the second invariant of the strain rate. The method adopted here calculates the invariant of all separate components while Moresi et al. (2002) calculates the second invariant of the total expression. As $(\mathbf{a}+\mathbf{b})_{II} = \mathbf{a}_{II} + \mathbf{b}_{II}$ is not satisfied for all $\mathbf{a}$ and $\mathbf{b}$, the methods yield different plastic viscosities.

It is beyond the scope of this work to research and test both methods, and a choice between the two has been made based on computational and implementation advantages. The viscoplastic code adapted to include elasticity (ELEFANT, Thieulot (2014)) does not have the ability to calculate the effective strain rate $\dot{\varepsilon}^{eff}$ in the routine used during the calculation of the plastic viscosity. The method using only the second invariant of the strain rate (49) only uses variables which are known in the routine. As this makes the implementation less difficult, the method employed by Gerya (2010) is favoured over the approach taken by Moresi et al. (2002). The benchmarks performed to test the plastic implementation indicate that the choice made regarding the calculation of the plastic viscosity has the desired effect and results in plastic failure of the material (see Section 9.4 and 9.5). The expected results are obtained and it can be concluded that the method employed produces correct results and has been successfully implemented.
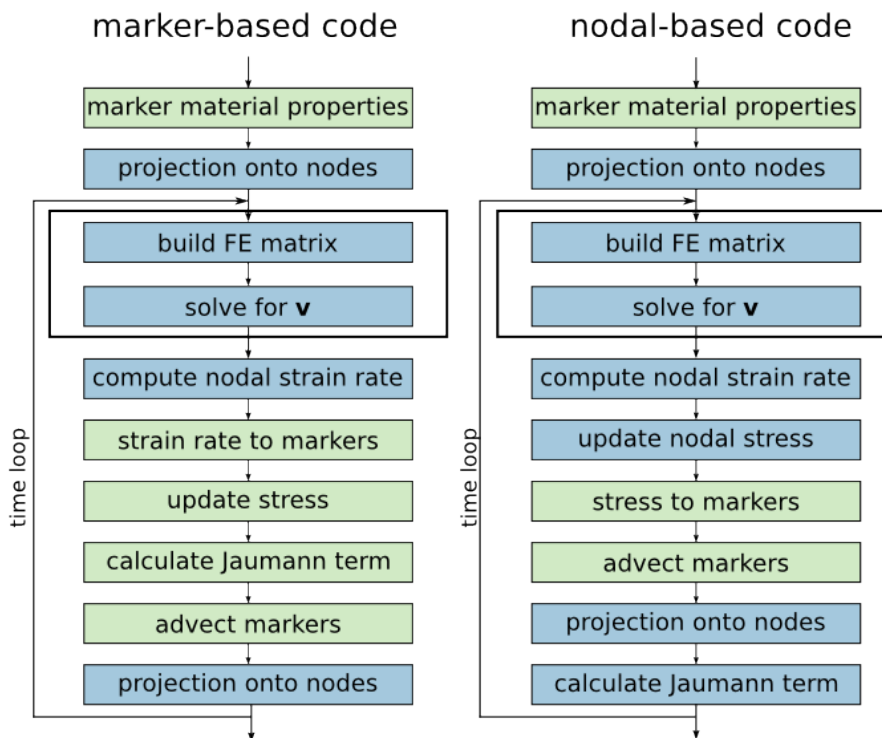
Figure 4: *Diagrams showing the structure of the marker- (left) and nodal- (right) based code. Green shows actions taken on markers, blue actions on the nodal points.*

5   Discussion on the elasticity implementation

5.1   Improving the elasticity implementation

In order to improve the viscoelastic-plastic implementation and stabilise the stress and velocity fields, several additional methods necessary to improve the results discussed below.

5.1.1   Using a marker- or nodal-based approach

Two approaches can be taken towards storing the stress memory of the modelled material, the marker- and the nodal approach. The most intuituve approach is the marker-approach. This method stores all quantities on the markers which act as material particles. All material properties and quantities such as stress and strain rate are stored on the material points (represented by the markers) and the nodal points are used solely for finite element interpolation purposes and calculation of the velocity field.

In contrast, when using a nodal approach, all quantities are stored and updated on the nodal points, and markers are used passively to advect the quantities needed during the next time step. Markers solely store their material properties and the accumulated stress field. The structure of both approaches is given in Figure 4. The differences between the two approaches becomes noticeable after the calculation of the strain rate on the nodes. For a marker-based code, the nodal strain rate (velocity gradient tensor) is interpolated onto the markers after which it is used to update the stress. A new Jaumann term is then calculated and the markers are advected. Where in the marker-approach the strain rate is interpolated to the markers in order to update the stress, the nodal approach continues on the nodes. The calculated nodal strain rate is used to update the accumulated stress which is then interpolated to the markers so the stress field can be advected along the velocity field (for the details on this interpolation, see Section 5.1.2). After advection, the stress field is projected onto the nodal points, and the Jaumann term is recalculated using the advected stress field (more information concerning the calculation of the Jaumann field in the nodal-based approach can be found in Section 5.1.3). Both approaches then reenter the core of the code where the finite element matrices are build and the governing equations are solved.

We compare both methods by performing the bending of an elastic beam benchmark from Gerya (2010) (see Section 8.1). The results of this comparison are given in Figure 5. It is clear that the marker-based approach produces unstable results with fluctuations in velocity of approximately 0.09 m yr^{-1}. On the other hand, the nodal-based code results in a smooth velocity decrease which is more regular and smooth than the results
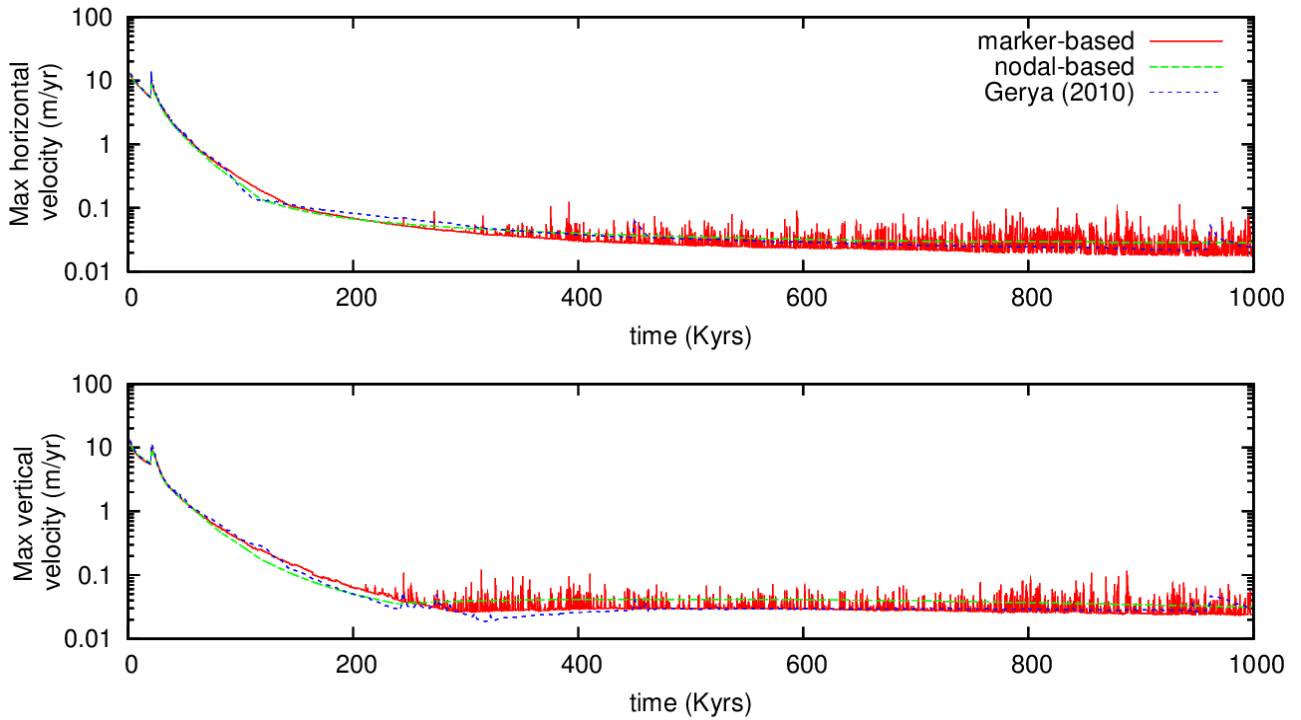
Figure 5: *Results of the marker- and nodal-based approaches of a viscoelastic-plastic code. The upper panel shows the maximum horizontal velocity (u) reached in the domain. The bottom panel shows the maximum vertical velocity (v) reached in the domain. The results from Gerya (2010) are also given.*

obtained by Gerya (2010). This difference in smoothness of the velocity curves can be explained by the fact that the accumulated stress field in the nodal case is more regular and uniform than in the marker case (Figure 6). The interpolation of the stress field from nodal point to marker causes a smoothing of the field. Due to the fact that in the nodal case the stress field is interpolated back and forth between the nodes and markers in order for it to be advected, the stress field is smoothed out and becomes more uniform. As the stress field is cumulative, smooth patterns build upon new smooth patters, resulting in a regular stress distribution.

In the marker case, the stress is accumulated on the markers. Interpolation only occurs during the stress field projection onto the nodes which is needed in the core of the code in order to solve for the velocity field. This smoothed stress field is however not used after solving for the velocity field. The old, non-smooth, field on the markers is updated and no smoothing takes place resulting in a build up of non-smooth stress. The difference is clearly visible in Figure 6. The xx component of the stress field τ_{xx} is given calculated after projection on the nodes (last and second to last step in Figure 4). It can be seen that the nodal-based code produces a cleaner and smoother stress distribution. The marker-based stress field shows many disturbances inside the beam and the edge of the beam is blurry. The stress field in the nodal-based approach follows the edges of the beam more accurately, resulting in a cleaner stress field. As the surrounding weak medium should not accumulate stress (it behaves viscous), a clear distinction between beam and medium is expected.

Besides producing more regular maximum velocities and stress fields, the nodal-approach has another advantage. Due to the fact that the markers are solely used to trace the materials and to advect the stress field, less fields have to be stored on the markers decreasing the memory needed throughout the model run. The nodal approach only stores the type of material and all components of the stress field on the markers while the marker approach stores the type of material, the stress field, the Jaumann field, the strain rate field and the rotation rate field on the markers. As all fields have 3 (2D) or 6 (3D) components, using the nodal approach is computationally much more attractive in terms of memory. The structure adopted in the nodal-based code is also very similar to the method in which advection of markers is replaced by advection of fields (see Section 6). Using the nodal approach, one can easily implement a marker-in-cell and/or field-based branch without having to adapt the interpolations.

Due to the computational advantages of, and the smoothness of the results obtained by the nodal-approach, it is strongly advised to adopt the nodal approach as described above.
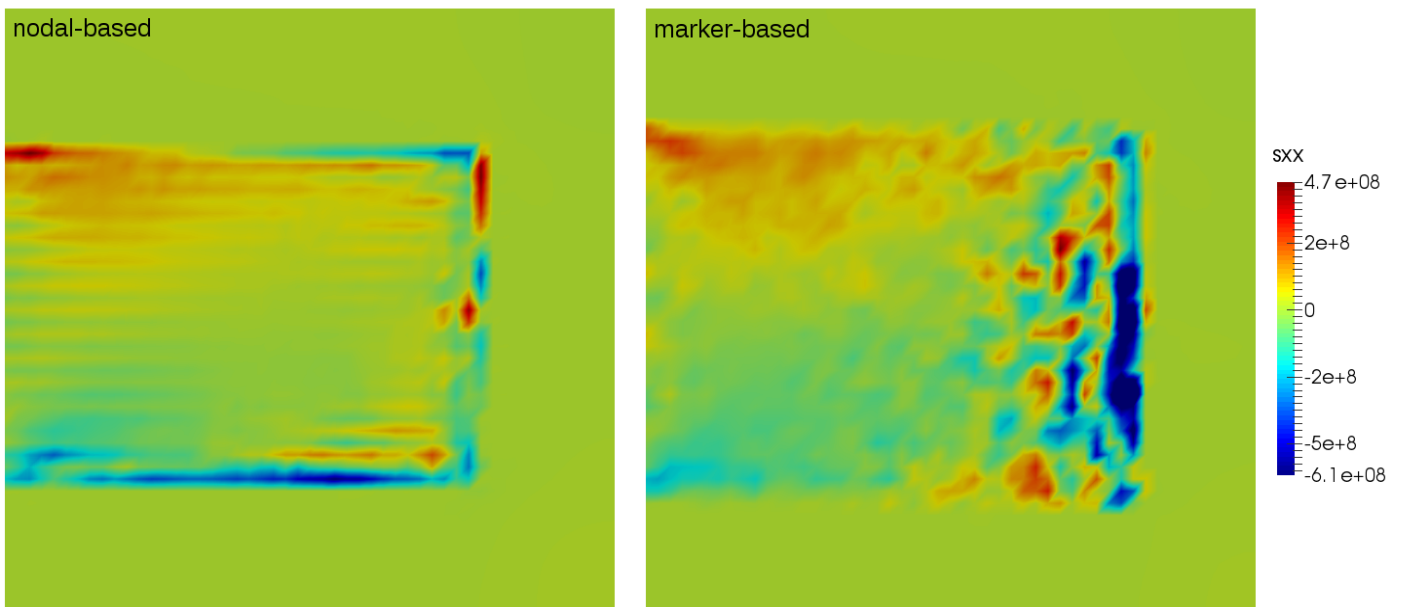
Figure 6: *The stress field (τ_{xx}) at t=2000 kyr for the nodal-based code (left) and the marker-based code (right).*
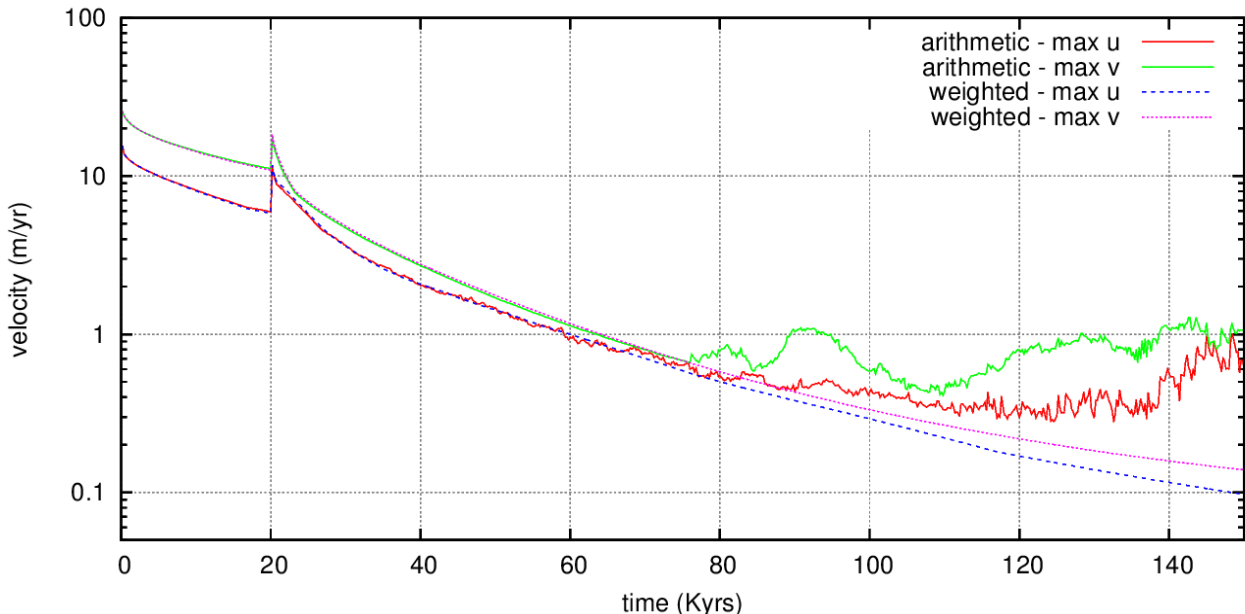
Figure 7: *The effect of using a weighted arithmetic averaging in comparison to an arithmetic averaging scheme for the maximum horizontal and vertical velocities in the domain.*

5.1.2 Interpolation of nodal stress on markers

Several additional remarks must be made concerning the interpolation and advection of the accumulated stress. When adopting the nodal-approach discussed in the previous section, it is important that a weighted arithmetic averaging is used during the back-and-forth interpolation between nodes and markers. The basis functions used in the finite element method act as weights. The effect of using a non-weighted arithmetic scheme on the maximum velocity in the domain during the sinking beam benchmark (Section 8.1) is given in Figure 7. It can be seen that the maximum velocity curves of the non-weighted averaging method are more irregular and less smooth than the weighted curve. It is thus advised to use a weighted averaging scheme for the interpolation and projection of the fields between markers and nodes. The effects of a harmonic and geometric averaging scheme are more erroneous than the non-weighted arithmetic (not shown).

The back-and-forth interpolation between the nodes and markers causes numerical diffusion. This numerical diffusion results in a decrease of amplitude for peaks and a smearing effect of sharp transitions (a more thorough discussion on diffusion is given in Section 7.1). When interpolating the absolute nodal values onto the markers using a first order interpolation scheme, subgrid variations are lost (Figure 8a). The diffusion caused by the interpolation can be minimised by interpolating not the absolute value of the field that needs to be advected (in this case, the accumulated stress), but only the change of the considered field on the nodal points. The interpolation of these increments ($\Delta\tau$, the stress change that takes place in this timestep) is added to the previous value recorded on the markers which can then be advected. The field can be projected back onto the nodes after advection. The use of these incremental values instead of absolute values counteracts the smoothing effect of the subgrid variations. Differences existing between markers are retained and stress is not diffused away limiting the possible effect of the elastic force. This limiting effect becomes visible when looking at the previously mentioned return-of-a-sinking-slab benchmark. Figure 9 shows this effect when absolute values are used. It can be seen that the maximum velocity in this case decreases significantly faster due to the decreased forcing from the diffused stress field. As the amplitude of this forcing is solely dependent on the accumulated stress field, diffusion of this field diminishes the elastic effect and thus the velocity with which the beam returns towards its original position. After 400 kyrs, the maximum stress for the absolute interpolation is already more than three orders of magnitude lower than for the incremental interpolation. The diffusion of the stress could even possibly result in diminishing the elastic effect and preventing the beam from fully returning to its starting configuration.

22
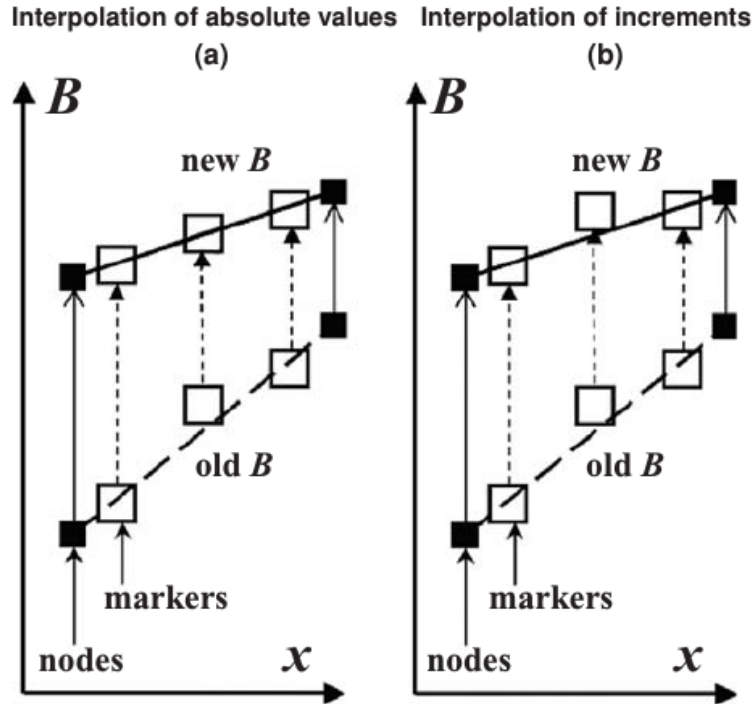
Figure 8: *The effect of the type of interpolation from nodes to markers. a) The absolute values are interpolated from the nodes. The old marker values are not used during the interpolation and previous subgrid variations are smoothed out. b) Interpolation of the nodal incremental values to the markers. The previous marker value is reused retaining the subgrid variations. Here, x represents the distance between two nodes and B represents the parameter that is interpolated. From Gerya (2010).*

Figure 9: *The effect of the absolute vs incremental interpolation on the maximum horizontal and vertical velocity in the domain.*

Figure 10: *Difference (%) in maximum horizontal and vertical velocity between the advected Jaumann field or the rebuilt Jaumann field approach.*
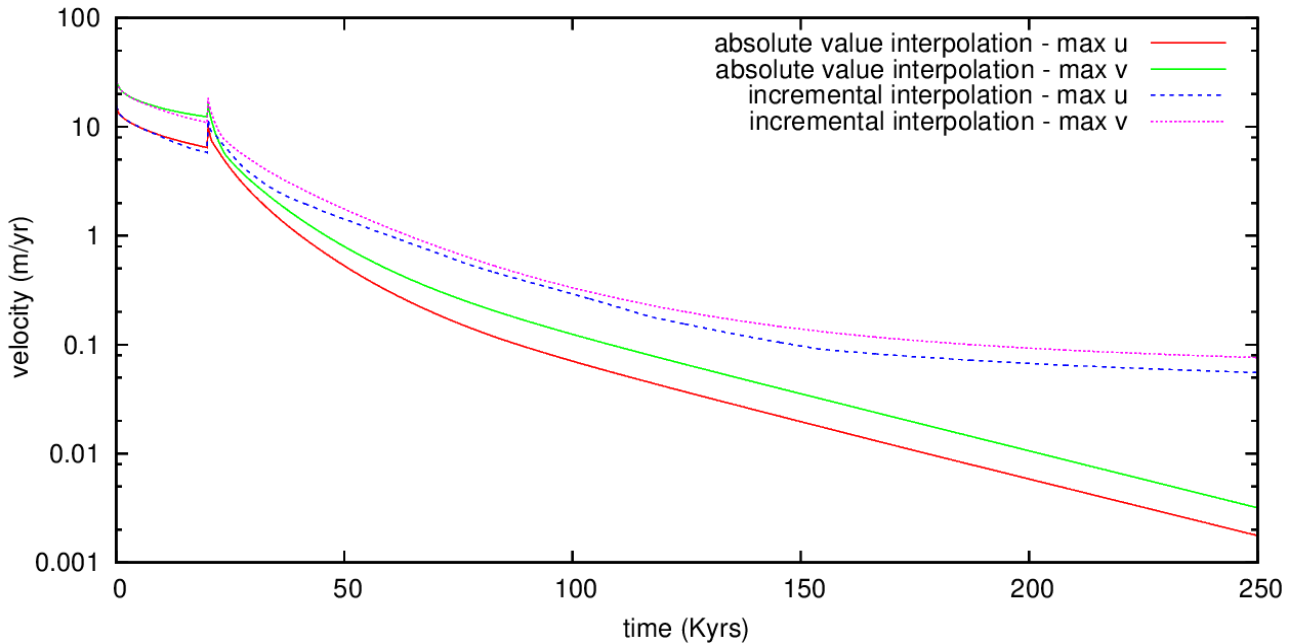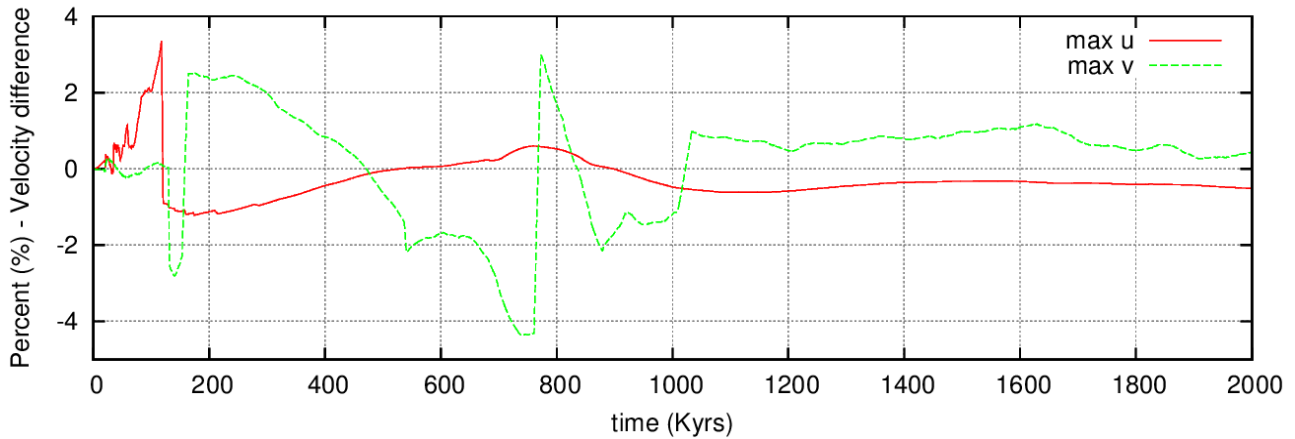
5.1.3 Calculation of the Jaumann term in a nodal-based code

Another remark that must be made when adopting the nodal-based approach for a viscoelasto-plastic code concerns the calculation of the Jaumann term. Due to the fact that the stress and Jaumann term of the previous time step are needed to solve the velocity field and to calculate the new stress, both need to be stored and advected along the velocity field in order to be used in the next time step. As the storage of such fields on markers requires a significant amount of memory, it is computationally better to store as little fields on the markers as possible. The material properties and the accumulated stress field need to be stored on the markers as the stress field needs to be advected together with the material. Saving computational power and memory could possibly be reached by researching the effect of the advection of the Jaumann term.

Two possible approaches can be adopted concerning the calculation of the Jaumann term.

1. Advecting the Jaumann field

2. Rebuilding the Jaumann field

In case 1, the Jaumann field is calculated using the current rotation rate field and the updated stress field ($\boldsymbol{r}^{t+\Delta t} = \boldsymbol{\omega}^{t+\Delta t}\boldsymbol{\tau}^{t+\Delta t} - \boldsymbol{\tau}^{t+\Delta t}\boldsymbol{\omega}^{t+\Delta t}$). The newly calculated Jaumann term is then interpolated to the markers which are advected along the current velocity field. After advection, the Jaumann term (and stress) is projected on the nodes and a new time step can be started.

In case 2, the updated stress is advected using the markers and projected back on to the nodes after which the advected stress and the non-advected rotation rate field are used to rebuild the Jaumann field which is then used in the finite element formulation and the calculation of the accumulated stress of the next time step. Since the stress field undergoes smoothing, the Jaumann field is also smoothed as a result.

Case 1 is the correct implementation as the Jaumann field is calculated before advection using the correct rotation rate field. However, it is computationally heavy due to the fact that the Jaumann term has to be stored on the markers and extra interpolation schemes are necessary. As the Jaumann term contains 3 (2D) or 6 (3D) components, it is computationally very expensive Case 2 is computationally lighter but uses an incorrect rotation rate field as it has not been advected together with the material field. It is assumed that for a sufficiently small time step resulting in small advection steps (ensured by using a Courant-Friedrichs-Lewy condition, Section 5.1.5) the differences arising due to neglecting the advection of the rotation rate field are trivial.

The effects of rebuilding the Jaumann term after advection and thus neglecting the advection of the rotation rate field given in Figure 10 and Figure 11. Again, the bending of an elastic beam benchmark from Gerya (2010) has been used (Section 8.1). Figure 10 shows the relative velocity difference for the horizontal and vertical velocity when using the second case in comparison to the results obtained for case 1. It can be seen that the velocity difference does not exceed 4% and stays constant at 0.5% after 1 Myrs. Figure 11 shows the effect on the accumulated stress field (τ_{xx} at $t = 2000\ kyrs$. It can be seen that rebuilding the Jaumann field following the case 2 approach does not cause significant alterations to the calculated stress field. The overall patterns are equal and differences that do arise are trivial. As no significant differences arise, it is therefore advised to adopt the second approach for the calculation of the Jaumann field. The differences arising in the accumulated stress field are not big enough to justify the use of extra memory and increased computational power needed. Note that the assumption made for case 2 may not be valid when extremely focused (local) high rotation rate zones are present and that a conservative CFL condition must be applied.
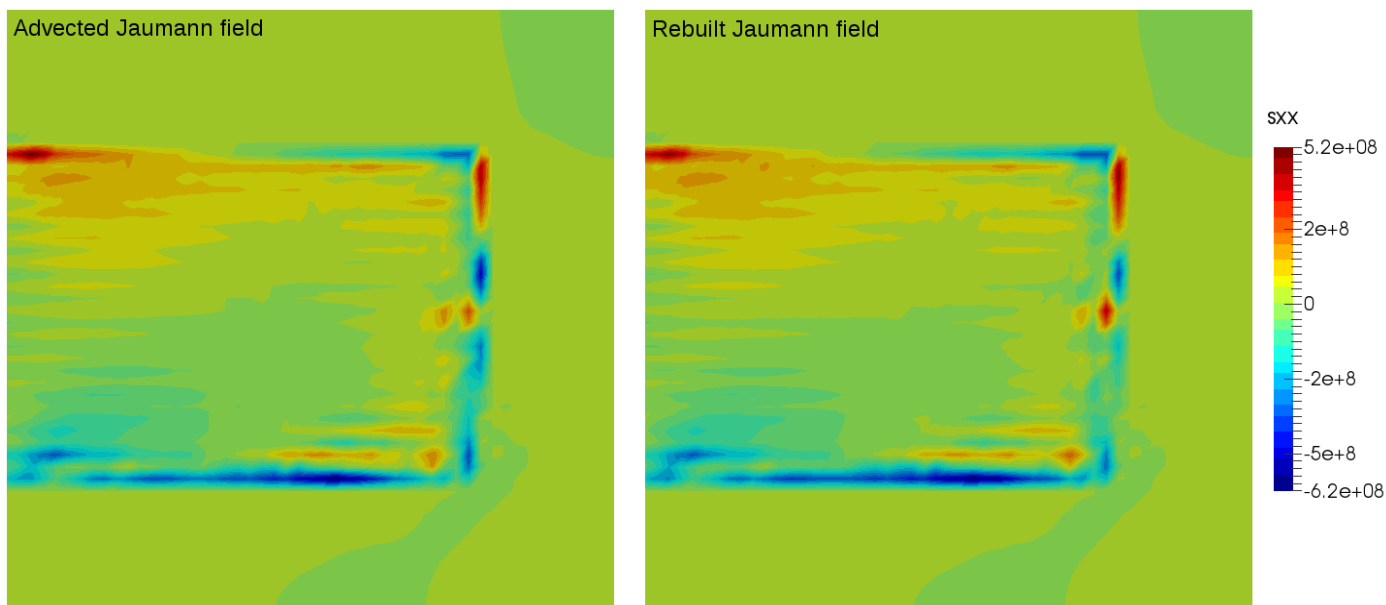
24

Figure 11: *The stress field (τ_{xx}) at t=2000 kyr for the advected Jaumann field (left) and the rebuild Jaumann field approach (right).*

5.1.4 Nodal versus elemental values

Another important remark that needs to be made concerns the use of nodal versus elemental properties. Material properties such as viscosity and density are often interpolated from markers and calculated as elemental properties meaning that the marker values are averaged over the element in which they reside. The same goes for strain and rotation rate calculations. As the strain rate is calculated using derivatives of the basis functions (see Appendix A.1) which are not known directly at the nodal points, an elemental strain rate is often calculated which is equal to the strain rate in the centre of the element.

Unfortunately, the use of elemental values for material properties and strain and rotation rates gives rise to a set of problems when elasticity is involved. As elemental fields are discontinuous (values jump when crossing from one element to the next) this can pose problems when calculating the stress field, especially around sharp discontinuities. This can be seen in Figure 12. An example is given using the shortening of an viscoelastic-plastic block (Section 9.5). There, a nodal viscosity model is shown together with a model using elemental viscosities. It can be seen that the strain rate field is strongly discontinuous and has much higher values in the weak layers present at the top and bottom of the domain (for a lay-out of the model, see Section 9.5). Note that the scale for the strain rate has been capped off at the maximum and minimum values of the nodal viscosity. The maximum and minimum strain rate for the elemental case are more than two orders of magnitude higher. It can bee seen in the bottom of the Figure that convection cells have arisen in the top and bottom layers which are the cause of the high strain rates in the weak medium. As the applied velocity field leads to pure shear, the onset of convection cells is erroneous and the elemental case thus produces incorrect results.

The error can be explained using the sharp viscosity discontinuity present at the interface. The sharp interface is smoothed out in the case using the nodal viscosity but when an elemental viscosity is used, the interface is sharp and discontinuous. As the viscosity is used during solving for the velocity field, the discontinuity can persist into the velocity field itself. As the velocity field is used to calculate the strain rate, and the elemental strain rate and viscosity are used to calculate the accumulated stress which is in turn used to calculate the velocity field, the error builds up and increases with every consequent time step. A runaway process is set in motion that increases through the cumulative nature that accompanies elasticity. This also explains why using elemental values is no problem when a viscoplastic rheology is used.

Due to the cumulative effect of the elasticity implementation that needs smoothing of the fields, it is thus advised to use nodal values instead of elemental values when elasticity is incorporated in a model. The nodal values must be used for material properties such as viscosity, density and the shear modulus, as well as the strain and rotation rate. How to calculate nodal strain and rotation rates is explained in Appendix A.1.
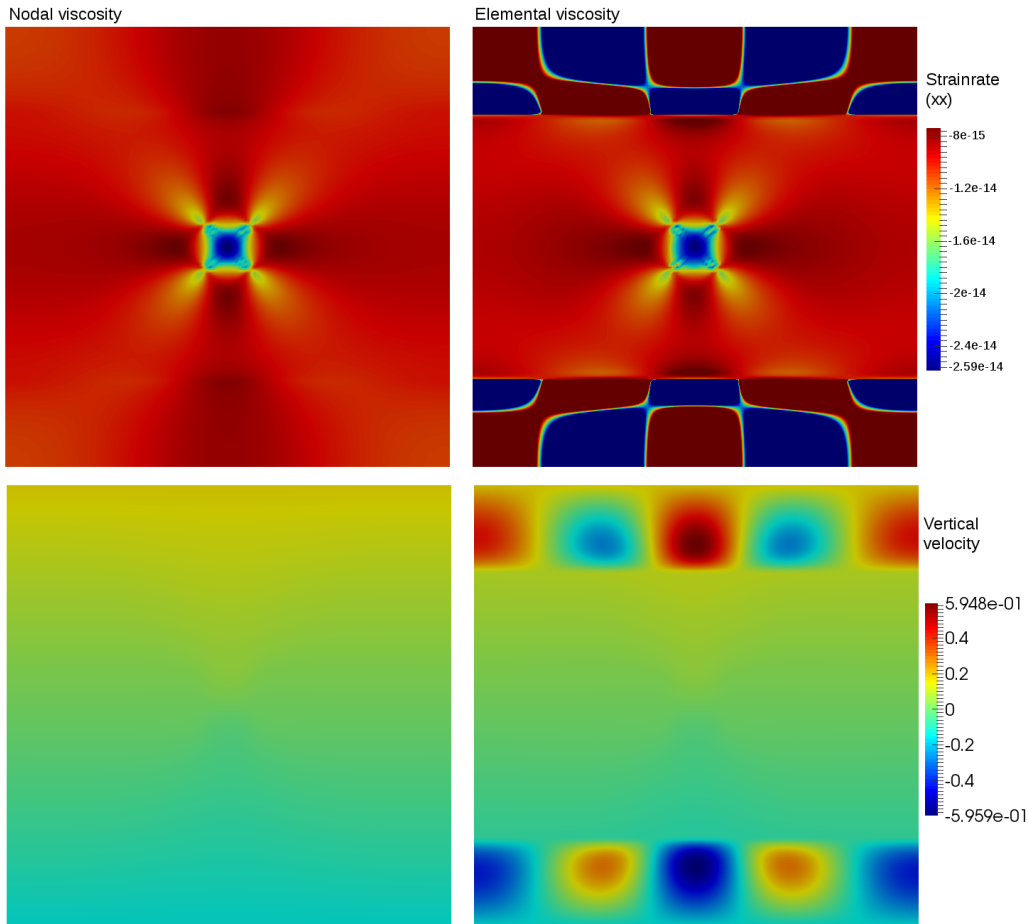
Figure 12: *The effect of using a nodal viscosity (left) and an elemental viscosity (right) for the strain rate (upper row) and the vertical velocity (bottom row). Note that for the strain rate the scale has been adjusted to the max and min of the nodal viscosity. The value of the strain rate for the elemental case is, in the weak medium, more than two orders of magnitude larger.*

5.1.5 Using a numerical advection time step

When incorporating elasticity into the rheology used in a model, the employed time step plays an important role due to the time dependence of the stress tensor. This elastic time step (Δt) appears when calculating the effective viscosity (η_{eff}, equation (21)), which is used when solving for the velocity field and during the calculation of the accumulated stress (embedded in the effective viscosity and the Jaumann term). The results obtained with an elastic model thus have a strong dependence on the chosen Δt.

Due to the fact that the time step directly influences the viscosity of the material, it determines the stiffness of the materials in the model. This means that the employed time step must be chosen from a physical perspective and cannot be chosen from a numerical perspective. Choosing a small time step to ensure that markers are not advected too far during one time step would result in a decrease in viscosity.

In order to prevent this while simultaneously ensuring that the advection of markers lies between chosen bounds, a distinction is made between the elastic time step (Δt_e) and a numerical (displacement/advection) time step (Δt_a). The elastic time step is chosen on physical grounds to ensure correct material behaviour and the latter is only used during the advection of the markers and is based on the advection distance.

With the chosen Δt_e, is used to calculate the effective viscosity and used where it appears in the right hand side (equation (32)) and the finite element formulation is used to solve for the velocity field. After solving for the velocity field, the Courant-Friedrichs-Lewy condition (Anderson, 1995) is applied to calculate the CFL time step Δt_{CFL} that ensures markers are not advected too far through the domain during one single time step.

$$\Delta t_{CFL} = C \frac{h}{\max |\mathbf{v}|} \tag{54}$$

The CFL time step depends on the prescribed Courant condition C, the element height h and the maximum velocity present in the domain.

26

The displacement time step is then defined using the following condition:

$$\begin{cases} \Delta t_a = \Delta t_{CFL} & \text{for} \Delta t_{CFL} < \Delta t_e \\ \Delta t_a = \Delta t_e & \text{for} \Delta t_{CFL} \geq \Delta t_e \end{cases} \tag{55}$$

If the CFL time step is larger than the prescribed elastic time step, the elastic time step is used during advection. However, if it is smaller than the elastic time step, the CFL time step is used during advection.

After defining the advection time step Δt_a, the effective viscosity is recalculated and the stress and Jaumann term are updated using the newly calculated effective viscosity and Δt_a. The markers are then advected and a new time step is entered. At the beginning of this new time step, the elastic time step Δt_e is used again to recalculate the effective viscosity and to solve for the velocity field. The whole process then repeats it self until the end of the time loop is reached.

Implementing a distinction between the elastic time step and the advection time step ensures that the viscosity used to solve for the velocity is not dependent on computational considerations while simultaneously ensuring that the amount of deformation (advection) in a single time step lies within acceptable bounds.

5.2 Advantages and disadvantages of adding elasticity to an existing code

Several advantages and disadvantages arise while adding elasticity to an existing viscoplastic code. These advantages and disadvantages are discussed below and which can be used when deciding whether or not to implement elasticity.

5.2.1 Advantages

The biggest advantage of adding elasticity to an existing viscoelastic code is that it provides the ability to model elastic behaviour of materials. As it is still unknown whether elasticity plays a major role in, for example, subduction dynamics, adding elasticity provides the opportunity to test the influence of elasticity and to numerically model situations where elasticity is known to play an important role (such as flexure).

Adding elasticity to a viscoplastic code does not eliminate the ability to model non-elastic materials. When no elasticity is desired in a model, the code can be made viscoplastic by setting the elastic shear modulus $\mu \to \infty$ reducing (47) to the viscous case (13).

Another advantage of adding elasticity concerns the onset of plastic behaviour. Due to the stress memory of an elastic material, stress levels gradually increase and approach the plastic threshold. This is a more accurate representation of reality in comparison to the viscoplastic case where the plastic threshold is reached instantaneously after strain rate levels become high enough. In the elastic case, strain bands gradually build up and increase in size whereas they suddenly arise as a whole in the an-elastic case.

The simplicity of adding elasticity to an existing code is another advantage. The finite element formulation needs only to be changed on the right hand side by adding a memory term and the left hand side needs the effective viscosity instead of the prescribed material viscosity. After solving the velocity field, the only change that needs to be made is the calculation of the stress. The memory and rotational term need to be added in order to obtain stress memory.

The occurrence of the effective elastic viscosity instead of the prescribed material viscosity in the finite element formulation used to solve for the velocity field has a significant influence on the model results. The effective (numerical) viscosity is lower than the prescribed material viscosity due to its dependence on the used shear modulus μ and time step Δt.

$$\eta_{eff} = \frac{\mu \Delta t}{1 + \frac{\mu \Delta t}{\eta}} = \frac{\eta}{1 + \frac{\eta \Delta t}{\mu}} \tag{56}$$

The effect of Δt becomes visible in Figure 13. It can be seen that, in this case, for large time steps ($\Delta t > 10^7$) no changes to the used viscosities arise making the model equal to the viscous case. For smaller time steps, the effective viscosity is lower than the prescribed material viscosity. This decrease in the viscosity (difference) makes it easier for the solver used to solve for the velocity field. Solving the linear system of equations will be faster and less computationally expensive. It is therefore computationally advantageous to implement elasticity as it decreases the viscosity difference that arises in mantle-lithosphere models.

5.2.2 Disadvantages

Besides giving a computational advantage, the dependence of the effective viscosity on the shear modulus and the time step also has a disadvantage.
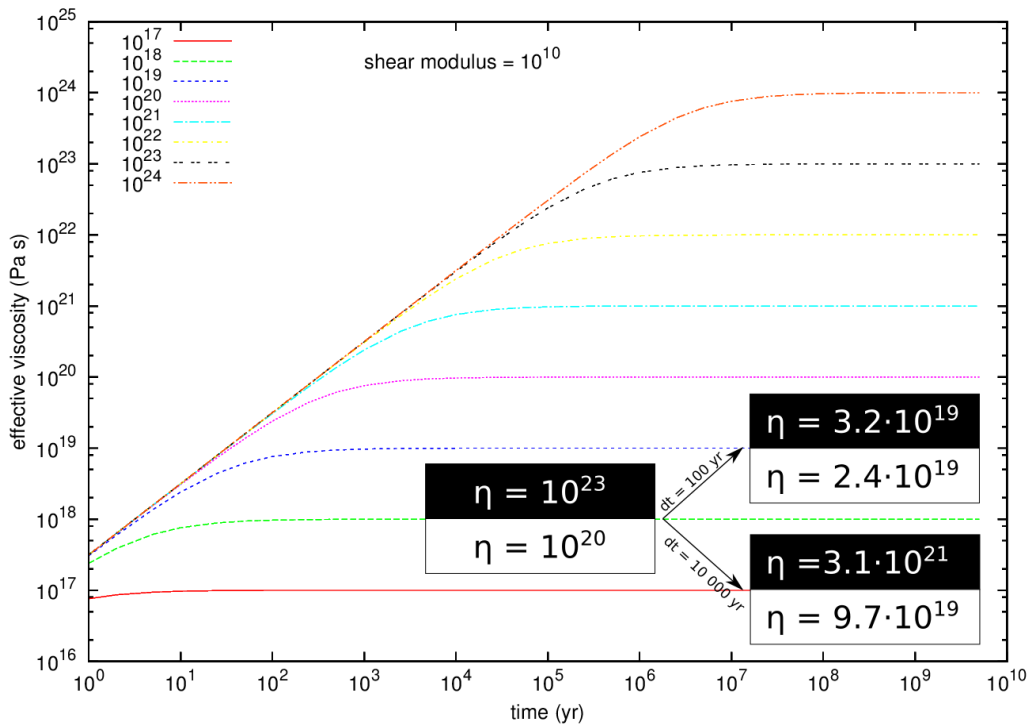
Figure 13: *The effect of the time step (x-axis) on the effective viscosity. A shear modulus of $10^{10} Pa$ has been used. Different prescribed material viscosities are plotted (prescribed value equal to their value at 10^{10}). The inset shows the effect of the choice of the time step for a specific lithosphere/mantle case: The viscosities on the left are the prescribed materal viscosities. The viscosities on the right are the effective elastic viscosities for a case where $\Delta t = 100$ year and $\Delta t = 10\ 000$ yr.*

When looking at the inset in Fig. 13 this disadvantage of the influence of the time step on a prescribed lithosphere/mantle system becomes clear. In the upper case ($\Delta t = 100$ yr) the initial viscosity contrast of three orders of magnitude has been reduced to a 1.3 times difference. As no significant difference exists anymore between the materials, they will behave alike and a stiff lithosphere is no longer present. When choosing a larger time step $\Delta t = 10000$ yr (lower case) the viscosity difference is larger, but still an order of magnitude smaller than initially prescribed.

The choice of time step is thus very important as it affects material behaviour. The fact that the choice of time step directly influences the outcome of the model is a serious disadvantage of incorporating elasticity. The arising subjectivity is an unwanted effect of elasticity.

Fortunately there is a guideline that can be followed when choosing a time step. The elastic time step Δt_e must lie between the Maxwell time t_M of the weakest material and the strongest material Gerya (2010). It must be significantly larger than the smallest Maxwell time and significantly smaller than the largest Maxwell time present in the model. This ensures that materials with a long Maxwell time behave elastic and materials with a small t_M behave viscous.

A last disadvantage accompanying the implementation of elasticity concerns the implementation of a stress memory. As discussed in Section 5.1.2 there are several methods towards storing and advecting the accumulated stress. As no correct method exists, a subjective choice has to be made based on computational and implementation considerations.

5.3 Conclusion on the viscoelastic-plastic implementation

The previous sections discussed the difficulties arising during the implementation of a viscoelastic-plastic rheology and the accompanying advantages and disadvantages. It has become clear that the implementation in itself is trivial and does not pose significant problems but that the choices made regarding averaging and interpolation between markers and nodes can have a significant impact on the outcome of the models. It is important to use a nodal approach and to use nodal averages for the strain rate and viscosity in order to smooth the solution fields. The problems arising during averaging and interpolation between nodes and markers are not uniquely existent for elastic codes. Viscoplastic codes also struggle with averaging problems (Schmeling et al., 2008) but because no memory term is present, errors do not tend to build up and increase with time. This means that the

errors arising during averaging are less persistent and do not lead to the problems which arise when elasticity is included.

The viscoelastic-plastic implementation is benchmarked in Section 9 using five different benchmarks which have an analytical solution or of which an approximate solution exists in the form of comparable available codes or communicated results.

6   Compositional fields and the advection equation

Materials can be tracked and advected throughout a domain by various approaches. The marker-in-cell technique is often used due to its intuitivity and the simplicity of its advection schemes. As shown in the previous sections, it does however exhibit problems when interpolating properties between markers and nodes, especially when large discontinuities are present (Schmeling et al., 2008).

An alternative method to advect and track materials is through the use of compositional fields. For this approach, the advection equation (57) is used to passively advect the prescribed field along the velocity field assuming zero diffusivity and incompressibility. This method does not use particles that trace the fluid making interpolation schemes redundant.

$$\frac{\partial C}{\partial t} + \mathbf{v} \cdot \nabla C = 0 \tag{57}$$

Here, $\mathbf{v}$ is the velocity field and C the field that is advected. The advection equation is derived from the heat transport equation (equation 2) with k and H zero.

6.1   Finite element formulation

The finite element formulation (weak form) corresponding to the advection equation (57) is

$$\mathbf{M} \, \frac{\partial \mathbf{C}}{\partial t} + \mathbf{K} \, \mathbf{C} = 0 \tag{58}$$

with

$$\mathbf{M} \quad = \quad \int_{\Omega} \mathbf{N}^T \, \mathbf{N} \, d\Omega \tag{59}$$

$$\mathbf{K} \quad = \quad \int_{\Omega} \mathbf{N}^T \, \mathbf{V} \, \mathbf{B} \, d\Omega \tag{60}$$

where $\mathbf{N}$ is the shape function vector and $\mathbf{B}$ the matrix of the spatial derivatives of the basis functions (30) and $\mathbf{V}$ the velocity vector.

In order to describe the time derivative of the field, a mid-point implicit scheme ($\alpha = 0.5$) is used with α a parameter describing the type of scheme. When $\alpha = 0$ the scheme is fully implicit and for $\alpha = 1$, the scheme is fully explicit. The finite element expression then becomes

$$[\mathbf{M}(t) + \alpha \mathbf{K}(t) \, \delta t] \, \mathbf{C}(t + \delta t) = [\mathbf{M}(t) - (1 - \alpha) \mathbf{K}(t) \, \delta t] \, \mathbf{C}(t) \tag{61}$$

or

$$\mathbf{A} \, \mathbf{C} = \mathbf{B} \tag{62}$$

with

$$\mathbf{A} \quad = \quad \mathbf{M}(t) + \alpha \mathbf{K}(t) \, \delta t \tag{63}$$

$$\mathbf{B} \quad = \quad \mathbf{M}(t) - (1 - \alpha) \mathbf{K}(t) \, \delta t \tag{64}$$

6.2   The SUPG stabilization scheme

It is a known problem when advecting fields that in cases where advection dominates over diffusion, non-negligible oscillations arise. To improve the stability of the solution, a stabilization scheme is often adopted. The streamline-upwind Petrov Galerkin stabilization method is one such method which is easily implemented in a finite element code. In this method, the $\mathbf{N}^T$ matrix in equation (60) is replaced by a modified version called $(\mathbf{N}^*)^T$ defined as

$$(\mathbf{N}^*)^T = \mathbf{N}^T + \tau \, \mathbf{v} \cdot \mathbf{B} \tag{65}$$

with τ a dimensionless stabilization parameter. For $\tau = 0$, no stabilization is used.
Multiple definitions for the stabilization parameter τ exist. Tezduyar and Osawa (2000) propose the following definition:

$$\tau = \left(\frac{1}{(\tau_1)^r} + \frac{1}{(\tau_2)^r} + \frac{1}{(\tau_3)^r} \right)^{-\frac{1}{r}} \tag{66}$$

where $r = 1$. τ_1, τ_2 and τ_3 are defined as

$$\tau_1 = \frac{h}{2 |\mathbf{v}|} \tag{67}$$

$$\tau_2 = \theta dt \tag{68}$$

$$\tau_3 = \frac{h^2 \rho c_p}{k} \gg 1 \tag{69}$$

h represents the minimum element size in the domain and θ relates to the time discretization scheme used which, in this case, is the mid-point implicit scheme resulting in $\theta = 0.5$. Because we assumed $k = 0$ in the advection equation, τ_3 approaches infinity resulting in a zero contribution of τ_3 to (66).

Hughes and Brooks (1982) and Braun (2003) argue for a τ dependent only on the diameter of an element and the velocity field. They use the following definition for the stabilization parameter

$$\tau = \frac{h}{|\mathbf{v}| \sqrt{15}} \tag{70}$$

The effect of the different definitions on advecting fields are shown by Thieulot (2011). The schemes can be compared using the dimensionless coefficient $\gamma = \tau |\mathbf{v}| / h$. For the non-stabilized Galerkin scheme, $\gamma = 0$, strong oscillations arise. With an increasing γ, the diffusion in the model increases which smooths the oscillations. The stabilization parameter as defined by Hughes and Brooks (1982) has $\gamma \approx 0.258$ and leads to a larger diffusion of the discontinuous boundary than the definition by Tezduyar and Osawa (2000) $\gamma \approx 0.04$. The implementation of the compositional fields and advection equation is benchmarked in Section 7. There the influence of both the stabilization schemes is researched.

6.3 Stabilizing by an artificial cut-off

Another method used to reduce the oscillations arising during the advection of a field is by artificially setting overshoots and undershoots back to their desired value. This means that compositional values above 1 are set to 1 and values below 0 are set to 0. This method reduces the oscillations and prevents the compositional fields obtaining negative values resulting in negative densities or viscosities. This method does not affect the oscillations with values between 0 and 1 which will continue to exist. The compositional fields are first extrapolated from the nodal points to the quadrature points (see Section 6.4) after which they are cut-off to contain values between the limits 0 and 1. The effect of the artificial cut-off is researched in Section 7.2.

6.4 Calculating material properties from compositional fields

In order to solve the finite element expression of the momentum conservation equation (Section 3) for the velocity, material properties such as density, viscosity (and for the viscoelastic case: effective viscosity, shear modulus and the accumulated stress) need to be known at the integration points. As shown in Appendix A.2, the accumulated stress can be calculated on the nodal points after calculation of the strain and rotation rate. The accumulated stress on the nodal points can then be extrapolated to the quadrature points which are used when solving the finite element equations. The compositional fields which track the materials are known at the nodal points and are thus also extrapolated from the nodal points to the quadrature points after which they are related to the material properties. The extrapolation from nodal points to a quadrature point is given in equation (71) for a compositional field. The same extrapolation is used for the accumulated stress and other fields. It is done using all four nodal points surrounding a quadrature point and basis functions in the considered element.

$$c_\alpha (\mathbf{x}_q) = \sum_{i=1}^{4} N_i c_\alpha (\mathbf{x}_i) \tag{71}$$

Here, $c_\alpha (\mathbf{x}_q)$ represents compositional field α at quadrature point $\mathbf{x}_q$ and $c_\alpha (\mathbf{x}_i)$ represents the same field on one of the four nodal points in the element. N_i represents the corresponding basis function.

In order to obtain the material properties from the compositional fields advected by the advection equation, the properties need to be related to the fields that carry the position of the different materials in the domain. For a model with two different materials as presented in Section 7.2, two compositional fields are advected (c_1 and c_2), each representing a material. The fields equal 1 at the positions containing that material, and zero for the positions where the considered material is not present. Therefore, in an ideal situation, the compositional fields would have a value of $c_1 = 1, c_2 = 0$ or $c_1 = 0, c_2 = 1$ indicating the presence of material 1 for the first

case and material 2 for the second case. However, due to the development of oscillations during advection, this is often not the case and the values deviate from 1 or 0. The material properties must therefore be calculated by averaging the contribution of each field.

In order to calculate the density at position $\mathbf{x_q}$, an arithmetic averaging is used.

$$\rho(\mathbf{x_q}) = \frac{\rho_1 c_1(\mathbf{x_q}) + \rho_2 c_2(\mathbf{x_q})}{c_1(\mathbf{x_q}) + c_2(\mathbf{x_q})} \tag{72}$$

For the viscosity, a geometric average is used due to the large viscosity differences arising when using realistic values.

$$\eta(\mathbf{x_q}) = 10^{\dfrac{c_1(\mathbf{x_q}) \, ^{10}\log(\eta_1) + c_2(\mathbf{x_q}) \, ^{10}\log(\eta_2)}{c_1(\mathbf{x_q}) + c_2(\mathbf{x_q})}} \tag{73}$$

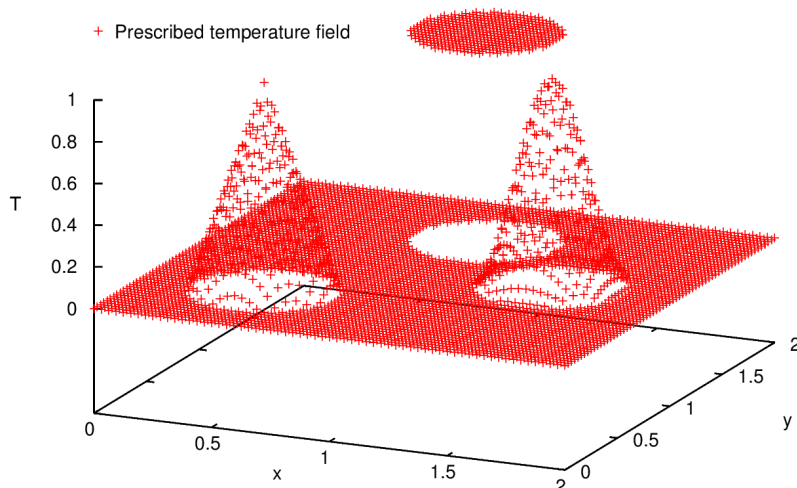The implementation of the compositional fields is benchmarked in the upcoming section.

Figure 14: *The prescribed temperature field for the advection benchmark on a 2 by 2 domain.*

7 Benchmarking the compositional fields implementation

The implementation of the compositional fields is tested using the rotating field problem from Donea and Huerta (2003) in Section 7.1 and van Keken's Rayleigh-Taylor instability (van Keken et al., 1997) (Section 7.2)

7.1 Benchmarking the compositional fields implementation using the rotating field problem

The implementation of the advection of the compositional fields is benchmarked using a set-up similar to Donea and Huerta (2003). The previously mentioned problems that arise during the advection of discontinuous fields are clearly demonstrated during this benchmark. It considers the advection of a prescribed (temperature) field in a purely rotating velocity field. The prescribed field is set to zero throughout the domain with the exception of a cone at $(\frac{1}{2}, \frac{1}{2})$, a cosine hill at $(1\frac{1}{2}, 1)$ and a disk at $(1, 1\frac{1}{2})$, all with a radius of 0.3 and a height of 1 (as shown in Figure 14). The velocity field in the domain is prescribed and equals:

$$
\begin{aligned}
u &= -(y-1) \\
v &= (x-1)
\end{aligned}
\tag{74}
$$

giving a purely rotational field. After a 2π radians rotation, the perturbations in the temperature field should be located at their initial positions and the effects of the advection scheme can be easily seen. The results of the advection of the field are compared to a test using the marker-in-cell technique and are shown in figure 15.

7.1.1 Results

In Figure 15A, markers have been used to track the rotation of the prescribed field while for Figure 15B to D, compositional fields have been used. The effect of advection using compositional fields becomes clear when comparing Figure 15A to Figure 15B and C. While the final configuration for 15A is identical to the initially prescribed field, it can be seen that this is not the case for the advection of fields. Figure 15B shows the oscillations that arise during the advection of compositional fields. When comparing Figure 15B to Figure 15C, it becomes evident that the oscillations are more pronounced for discontinuous fields, as is the case for the disk included at (1,1.5). The oscillations occur around the discontinuity which spread further throughout the domain as the disk is advected. The oscillations in Figure 15B have a non-negligible size. The largest oscillation results in an under- and overshoot of 31%. The continuous field as prescribed in Figure 15C does not lead to spurious oscillations. There, the disk has not been included and the prescribed field only includes the continuous cosine hill and non-smooth cone. It can be seen there that the end result lies very close to the prescribed initial field. Small oscillations can be seen surrounding the cone. The cone is non-smooth at the top resulting in the occurrence of oscillations with an overshoot of 3%. This error is significantly smaller than the error arising for the discontinuous field. The smooth and continuous cosine hill does not create oscillations while being advected.

The previous results show the problems that arise when using fields to advect a material or a temperature field which is discontinuous or non-smooth. When considering a smooth distribution, the oscillations arising due

33

to advection are minor and pose no problems. However, when considering a discontinuous or non-smooth field (as is the case when advecting material compositional fields), oscillations of significant size appear. In order to reduce these oscillations, a stabilizing scheme can be used as described in Section 6.2.

The use of the streamline-upwind Petrov Galerkin (SUPG) method from Tezduyar and Osawa (2000) results in a slight numerical diffusion diffusing the arising oscillations during advection. The SUPG stabilization scheme has been used in the model runs shown in Figure 15D and E. It can be seen there that the amplitude of the oscillations has decreased significantly, even when a discontinuous field is used as in Figure 15D. There, the maximum overshoot has decreased to 10%. When considering the field without the discontinuous disk, no oscillations are present. The SUPG scheme proposed by Tezduyar and Osawa (2000) thus completely removes the oscillations for a (non-)smooth, continuous field and decreases the oscillations by 20% for a discontinuous field.

However, despite the near absence of oscillations, due to the diffusion now playing a role, the prescribed fields have diffused resulting in a shape change of the perturbations. The boundaries of the discontinuous disk have diffused and its edges are no longer sharp. The diffusion of the cone and cosine hill results in a decrease of their height by 20% for the cosine hill and 25% for the non-smooth cone. The effect of the diffusion on the cosine hill and cone is visualized in Figure 16. It can be seen there that the diffusion decreases the height of the perturbation. When comparing the decrease in height between the cosine hill and the cone, it can be seen that for every method, the height of the cone decreases more than the height of the cosine hill. When comparing the results from the models using no SUPG stabilization scheme, it can be seen that the height of the cosine hill fluctuates around zero with a maximum deviation of 1%. The cone on the other hand decreases in height after which it remains constant at a height around 0.92. The difference between these two perturbations can be explained by the fact that sharp, small scale structures such as the top of the cone are difficult to preserve when advecting a field. A high resolution is needed to capture these small scale structures and the resolution used in this benchmark has not been sufficient to achieve this.

Comparing the results from when the SUPG scheme of Tezduyar and Osawa (2000) was used, it can be seen that the decrease in height of the cosine hill perturbation is slightly less than 20% and 35% for the cone. This increased decline of the height of both perturbations can be attributed to diffusion. When the SUPG method from Braun (2003) is used, the height has decreased with more than 50% for the cosine hill and 60% for the cone. This difference can be explained by the fact that the second SUPG method introduces a diffusion term in the advection which is larger than the term introduced by Tezduyar and Osawa (2000). These results show that for continuous fields, the SUPG schemes are best not used due to their introduction of undesirable diffusion.

Due to the arising oscillations when discontinuous and non-smooth fields are considered, it is advised to use a stabilization scheme. When only smooth fields are considered, it appears to be better not to use the SUPG method since it diffuses the field leading to significant decrease in amplitudes of the perturbations. The SUPG scheme from Braun (2003) leads to a greater diffusion than the stabilizing scheme proposed by Tezduyar and Osawa (2000). In this case it is advised to use the scheme from Tezduyar and Osawa (2000) which leads to the least diffusion.
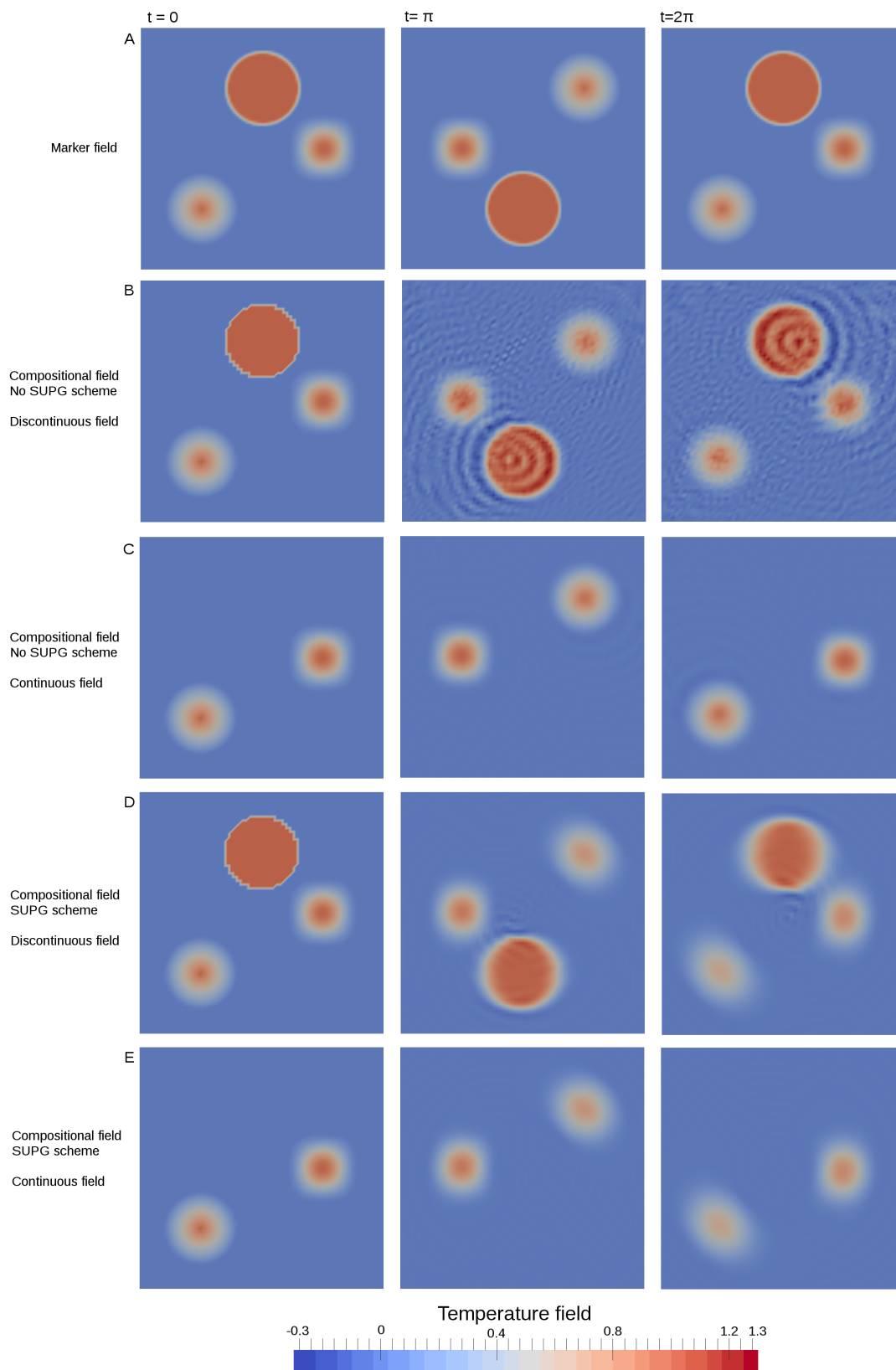
Figure 15: *The results of the rotating cone problem given at t=0, t=π and t=2π where the temperature field is tracked by markers in **A** and compositional fields in **B** to **E**. **C** and **E** do not include the disk anomaly and thus represent continuous fields. **D** and **E** use the SUPG stabilization scheme from Tezduyar and Osawa (2000).*
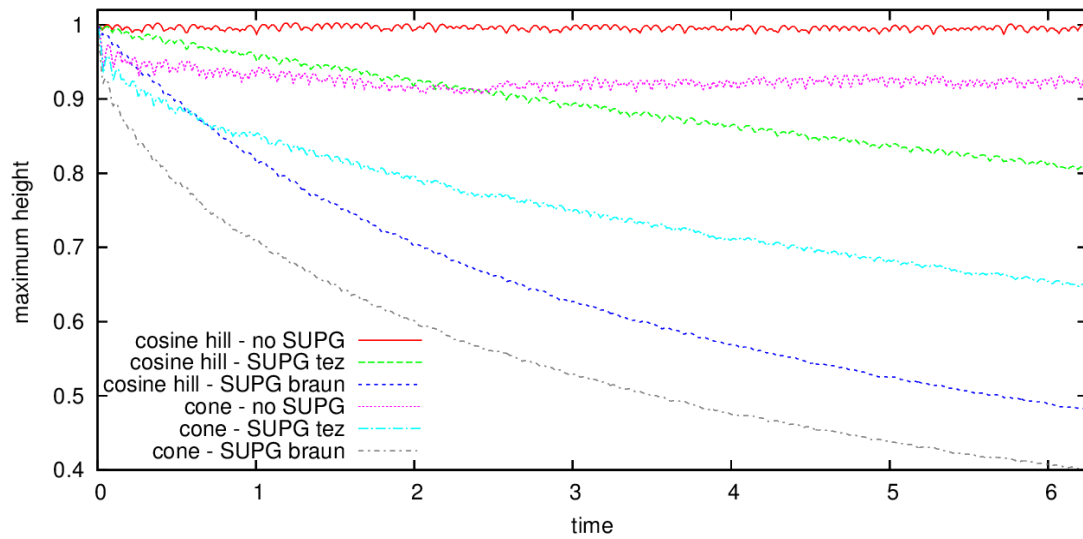
Figure 16: *The height of the peak of the cosine hill and cone through time using different methods. Both start at a height of 1. Tez stands for the SUPG scheme proposed by Tezduyar and Osawa (2000), braun for the scheme proposed by Braun (2003).*
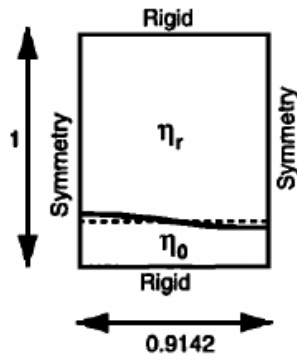
Figure 17: *Set up of the van Keken benchmark. A dense fluid lies on top of a more buoyant fluid with a cosine shaped interface.*

7.2 Benchmarking the compositional fields implementation using a Rayleigh-Taylor instability

In order to benchmark the advection of the compositional fields when large deformations are considered, a Rayleigh-Taylor instability benchmark is done. This benchmark was first performed by van Keken et al. (1997) and is therefore referred to as the Van Keken benchmark.

In this benchmark a Rayleigh-Taylor instability is prescribed to a 2-D domain of size λ by 1 where λ is chosen as 0.9142. The fluid in the domain is assumed to be incompressible and two different density compositions are prescribed. The high density layer lies on top creating a gravitationally unstable configuration. The height of the interface is given by:

$$y_c = 0.2 + 0.02 \cos\left(\frac{\pi x}{\lambda}\right) \tag{75}$$

The viscosity of both layers is $\eta = 100 \ Pas$, the density of the bottom layer is $\rho_1 = 1000 \ kg/m^3$ and the density of the top layer is set to $\rho_2 = 1010 \ kg/m^3$. A vertical gravity of $g_y = 9.81 m/s^2$ is prescribed to drive the flow. No-slip boundary conditions are applied to the bottom and top of the domain and free-slip boundary conditions to both sides. The set-up of the benchmark is shown in Figure 17.

In order to compare the outcome of the benchmark to the results of van Keken et al. (1997), the root-mean-square velocity is calculated for the domain as a function of time.

$$v_{rms} = \sqrt{\frac{1}{A} \int_A |\mathbf{v}|^2 \, \mathrm{d}A} \tag{76}$$

with A the surface of the domain and $\mathbf{v}$ the velocity field in the domain.

The benchmark is run for a model using markers to track materials (as is used by van Keken et al. (1997)) and for several models using compositional fields to track materials. The results are then compared to see how well the compositional model performs.

7.2.1 Markers

The results of the benchmark from the marker model are shown in Figure 18. It can be seen there that the result of our model is equal to the results from van Keken et al. (1997). All small scale structures are present and are located at the positions as obtained by van Keken et al. (1997).

7.2.2 Compositional fields

In order to test the compositional implementation and the effect of the different SUPG schemes on the outcome of the benchmark, multiple models are run. The model abbreviations and details are given in Table 1. All models except 9 and 10 are run with a resolution of 151 by 151 and all models besides 7 and 8 use a Courant number of 0.05. Models 1, 2 and 3 are run in order to test the influence of the different stabilization schemes. Models 4, 5 and 6 use an artificial cut-off as described in Section 6.3. The different SUPG schemes are applied in these models as well. Models 7 and 8 are used to research the influence of the time step (which is calculated using the Courant number) and models 9 and 10 to research the influence of the resolution on the model. An under - and overshoot error of 5% are accepted as adequate results.
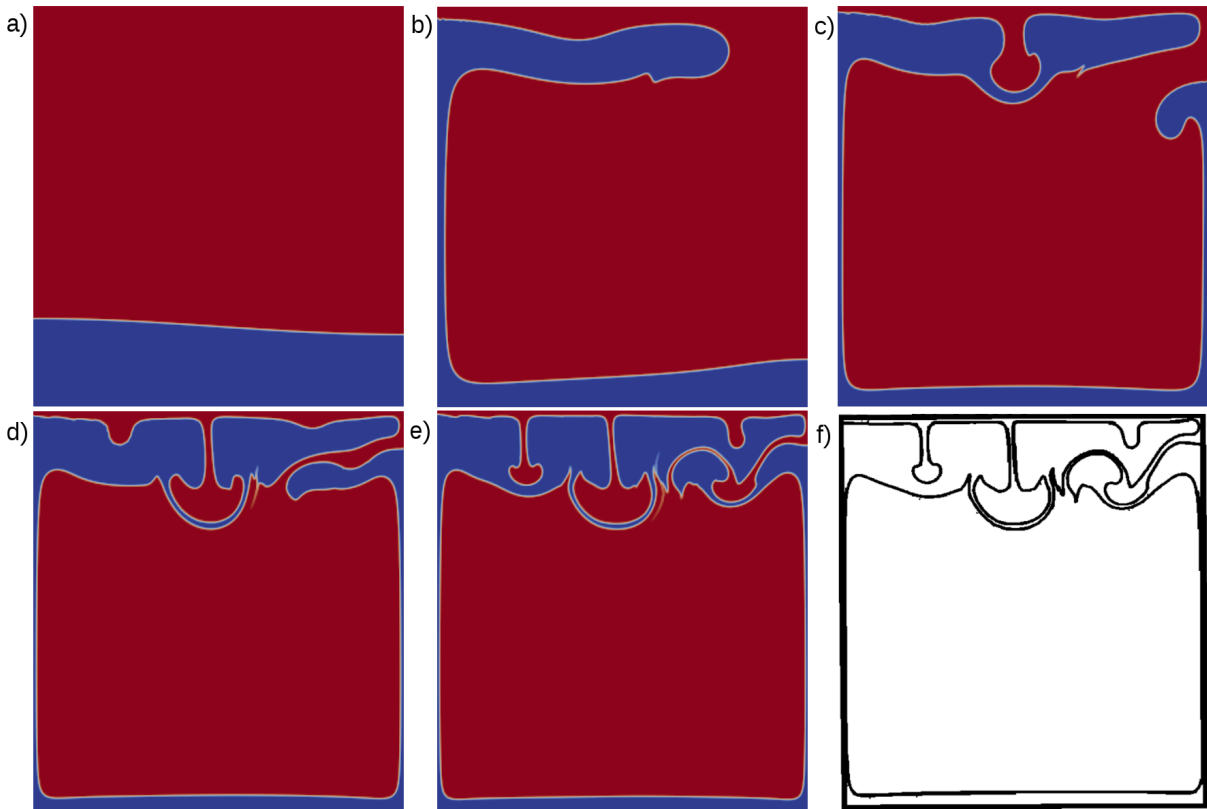
Figure 18: *The results of the Van Keken benchmark using markers to track the materials. Configurations at: a) t= 0, b) t= 500, c) t= 1000, d) t= 1500, e) t=2000, f) result from van Keken et al. (1997) at t= 2000.*

The end results of all models at $t = 1400$ are given in Figure 19. The effect of a stabilization scheme becomes visible in Figure 19. The compositional fields in model run 1noSUPG which uses no stabilization reach values from $C = $ -1.424, meaning an undershoot of 114%, to 2.123 (112% overshoot). A very large amount of non-negligible oscillations have occurred throughout the domain. The oscillations in general have an overshoot smaller than 40%. When comparing these results to model run 2SUPGtez, it becomes clear that the field has become slightly smoother. The oscillations are still present, but there is less interference between the oscillations. The maximum overshoot has decreased by 30%, but still lies above 88%. The undershoot has decreased to 113%. The general amplitude of the greater part of the oscillations has decreased below 30%. The SUPG method as proposed by Tezduyar and Osawa (2000) does not appear to be sufficient to suppress the oscillations in this benchmark. When considering the model run 3SUPGbr using the SUPG method as proposed by Hughes and Brooks (1982) and Braun (2003), the maximum overshoot has now decreased to 22% and 14%. The oscillations in general now have an amplitude of less than 5%, which is below our threshold for the error.

When only considering the amplitude of the oscillations, it becomes evident that the SUPG method proposed

Table 1: *Model descriptions for the compositional fields models.*

Model	Description
1noSUPG	no stabilization
2SUPGtez	stabilization scheme from Tezduyar and Osawa (2000)
3SUPGbr	stabilization scheme from Braun (2003)
4noSUPGlimit	artificial cut-off prescribed at 0 and 1
5SUPGtezlimit	artificial cut-off prescribed at 0 and 1, stab scheme Tezduyar and Osawa (2000)
6SUPGbrlimit	artificial cut-off prescribed at 0 and 1, stab scheme Braun (2003)
7SUPGtezcour	Courant num. = 0.01, stabilization scheme from Tezduyar and Osawa (2000)
8SUPGbrcour	Courant num. = 0.01, stabilization scheme from Braun (2003)
9noSUPGres	resolution of 201 by 201, no stabilization
10SUPGbr-res	resolution of 201 by 201, stabilization from Braun (2003)

by Braun (2003) suppresses the oscillations to such an extend that the majority lies below the overshoot threshold of 5%. However, when looking at the effects on a visual level, it becomes apparent that the diffusion greatly influences the distribution of the materials. The location of the centre down welling at the top of the domain has deviated to the left. The formation of a rising plume on the right of the domain has not progressed as far as in model runs 1 and 2. The spatial error due to diffusion is also large around the plumes. The boundary between the two compositions has faded resulting in a continuous field. This change in spatial evolution of the model and the diffusion of the compositional boundaries due to the use of the SUPG stabilization scheme are undesirable side-effects which should be kept at a minimum.

When considering the models using the artificial cut-off (19 d to f), it can be seen that the amount of oscillations has not changed. The minimum and maximum compositions are still at 0 and 1 since the fields are artificially set back to the closest limit value when they surpass theses limits. The overall amplitude of the oscillations is lower than in model 1, generally not surpassing an overshoot of 20%. No differences arise between model run 4 and 5 again implying that the SUPG method proposed by Tezduyar and Osawa (2000) is insufficiently effective for this benchmark. When considering model run 6SUPGbrlimit, the oscillations have disappeared with the exception of one along the left, bottom and right side located right beside the upwelling. Model 6SUPGbrlimit gives smaller errors than model 3SUPGbr. Again, the use of the SUPG scheme has affected the lay-out of the up- and down-wellings and caused a diffusion of the compositional boundaries.

Comparing Figure 19g and h to b and c respectively, the effects of a smaller Courant number becomes visible. It can be seen that decreasing the size of the time step does not significantly decrease the amplitude of the oscillations or the overall appearance of the compositions. However, choosing a higher resolution does result in a lower amplitude for both the standard compositional fields as well as the SUPG stabilized model run (compare Figure 19 j and k to a and b). Especially combining the higher resolution with the SUPG stabilization from Braun (2003) results in a decrease of the number of oscillations.

Figure 20 shows the maximum amplitude of the over/undershoots during the model run for each model (artificial cut-off models excluded). It can be seen that the models with the SUPG stabilization scheme from Braun (2003) exhibit significantly different behaviour staying under the 20% overshoot error during the whole model run. The error of the other models increases during run time, exhibits severe fluctuation and all reach an overshoot error greater than 100%.

Besides a visual comparison of the end results and the overshoot of the amplitudes, the root mean square velocity in the domain can also be used to determine the effects of using compositional fields on the results of the benchmark. The results of the root mean square velocities during the benchmark are given in Figures 21 and 22. In the following discussion concerning the evolution of the root mean square velocity of the domain, the differences in the timing and height of the second peak will be ignored. They have been shown by Bangerth et al. (2016b) to be greatly dependent on the resolution of the model. For a more thorough discussion on the second peak, the reader is referred to Section 7.2.3 and Bangerth et al. (2016b)/Bangerth et al. (2016a). The difference in timing of the onset of the second peak explains the difference in progression of the upwelling on the right side of the domain in Figure 19 between the compositional fields (Figures 19 a to h) and the marker-based model (Figure 19i). As shown below, the second peak occurs later in a marker-based model explaining the fact that the right plume has developed to a lesser extend.

Figure 21 shows the evolution of the root mean square velocity (equation 76) trough time of models 1 to 6. The results from the marker benchmark and the benchmark by van Keken et al. (1997) are also shown. The results of the marker model and the model by van Keken et al. (1997) are very similar. Differences are present in the height of the first peak and the timing and height of the second peak. When comparing the compositional field models to the two models that are marker-based, one can observe that the results differ significantly. The peaks of models 1, 2 and 3 have shifted by 10 time units and occur later in time. The height of the first peak has also increased by approximately 5%. It can be seen that the results of model 1noSUPG and 2SUPGtez are the same. However, model 3SUPGbr deviates from the first two models. It has a lower v_{rms} thus lying closer to the marker-based models but the value is still too high. The graph of the models using an artificial cut-off (models 4noSUPGlimit, 5SUPGtezlimit and 6SUPGbrlimit) all exhibit different behaviour when compared to the previous three models. The entire evolution of the v_{rms} of models 4 and 5 is significantly delayed. The height of the first peak has declined slightly in comparison to model 3SUPGbr. The model that lies closest to the v_{rms} evolution of the marker-based methods is model 6SUPGbrlimit. It has a comparable root mean square velocity during the first peak but the timing is still off.

The influence of the resolution and the size of the time step on the root mean square evolution can be seen in Figure 22. It can be seen there that the size of the time step (represented by the Courant number C) does not affect the evolution of the v_{rms}. Both the curves from models 7 and 8 lie on top of their corresponding models using a higher Courant number, models 2 and 3 respectively. However, the resolution does influence the outcome of the model. It can be seen that when using a higher resolution, the height of the peak decreases and is shifted slightly to the left, lying closer to the two marker-based models.

When only considering the overshoot error and the v_{rms} of the different models, it can be concluded that the SUPG scheme proposed by Hughes and Brooks (1982) and Braun (2003) gives the best results. This method results in the smallest overshoot error and in a root mean square velocity that resembles the original benchmark closest. The results can be improved by using a higher resolution or by using an artificial cut-off.

It has been shown that the use of the SUPG scheme from Braun (2003) leads to diffusion of the compositional boundaries. This results in a change in the spatial evolution of the model as shown in Figure 19. The influence of the different methods (SUPG/cut-off) on the spatial evolution and diffusion of the boundaries can be visualized by plotting the value of the compositional fields across a cross-section. The locations of the cross-sections are given in Figure 19i (1) and l (2).

Figure 23 visualizes the effect of several methods on the value of the compositional fields along the left domain boundary. It clearly visualizes the oscillations that arise due to the advection of the compositional field. It can be seen that the standard method of model 1 produces the most pronounced oscillations. Models 2, 4 and 5 produce oscillations with the same amplitude, where 4 and 5 do not go below the threshold of 0 due to their artificial cut-off. Note that all models produce an equal number of oscillations. The models producing oscillations with the lowest amplitude which go to zero after $x = 0.05$, are models using the SUPG method by Braun (2003). Model 6 using both this SUPG method and the artificial cut-off and as a result produces oscillations with the lowest amplitudes.

The cross section in Figure 23 is made in a relatively undisturbed area of the domain. Figure 24 shows a cross-section in a location of large deformation, where heavy mixing has taken place and where the compositional boundaries have diffused due to stabilization. The location of cross-section number two is given in Figure 19l.

The models have very different compositional values along cross-section 2. The spatial variation regarding the rightmost upwelling visible in Figure 19 can be seen in this cross-section. In the cross-section (0 lies at the top op the domain, and the end 0.35 below the starting point. It can be seen that the second upwelling from the top has progressed further for models 1, 2 and 5. The second upwelling in the models using the stabilization by Braun (2003) has risen to a smaller height. This difference is caused by the timing of the second plume which has been shown by Bangerth et al. (2016b) to depend on resolution and chosen method.

This plot clearly shows the negative side-effects of the stabilization methods. When no, or insufficient stabilization is used, oscillations of significant height arise with some reaching an overshoot of 40%. When the stabilization scheme from Braun (2003) is used, which is sufficient to suppress the oscillations, the compositional boundaries are less sharply defined making the transition between different materials more gradual. The diffusion also causes whole sections of the compositional field to be in between the two materials, as seen between 0.05 and 0.15 in the Figure.
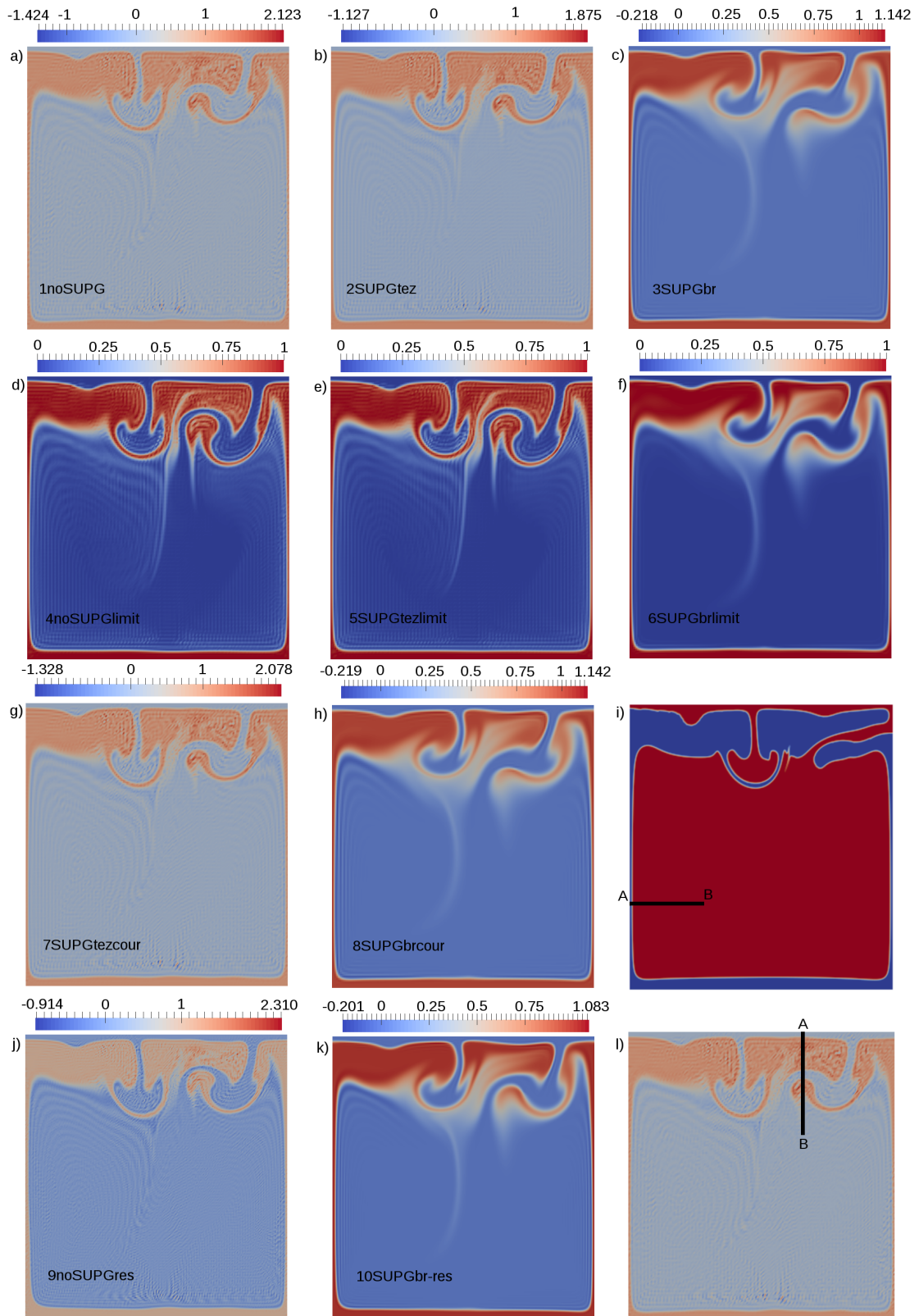
Figure 19: *The results of the Van Keken benchmark using compositions to track the material fields. All figures are at t = 1400, a) model 1noSUPG, b) model 2SUPGtez, c) 3SUPGbr, d) 4noSUPGlimit, e) 5SUPGtezlimit, f) 6SUPGbrlimit, g) model 7SUPGtezcour, h) model 8SUPGbrcour, i) location of cross-section 1, j) 9no-SUPGres, k) 10SUPGbr-res, l) location of cross-section 2. The scale for each model is given above each figure.*
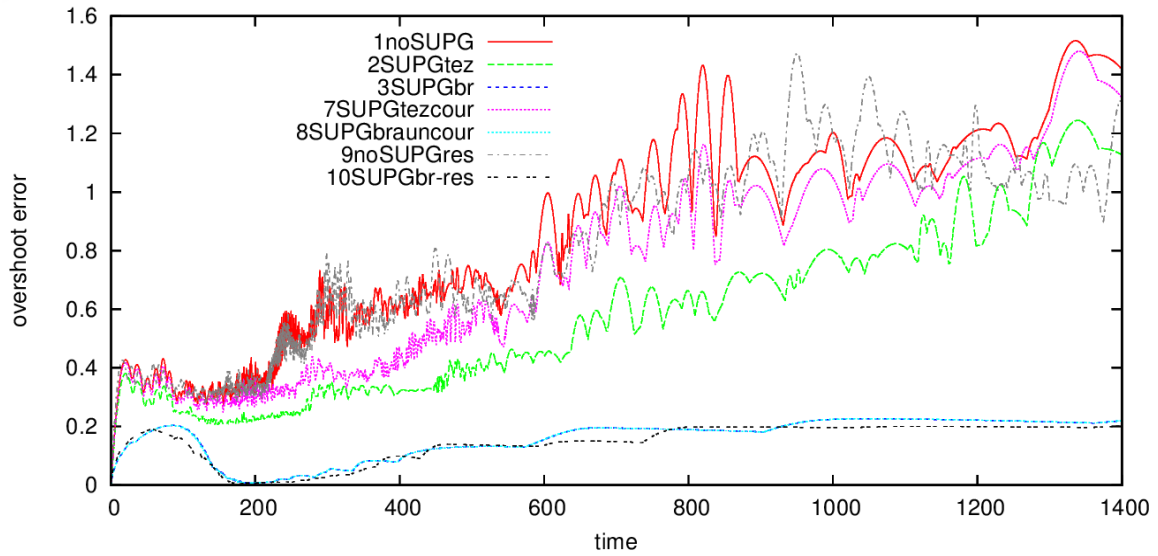
Figure 20: *The maximum overshoot error for models 1 to 4 and 9 and 10 during model run time.*
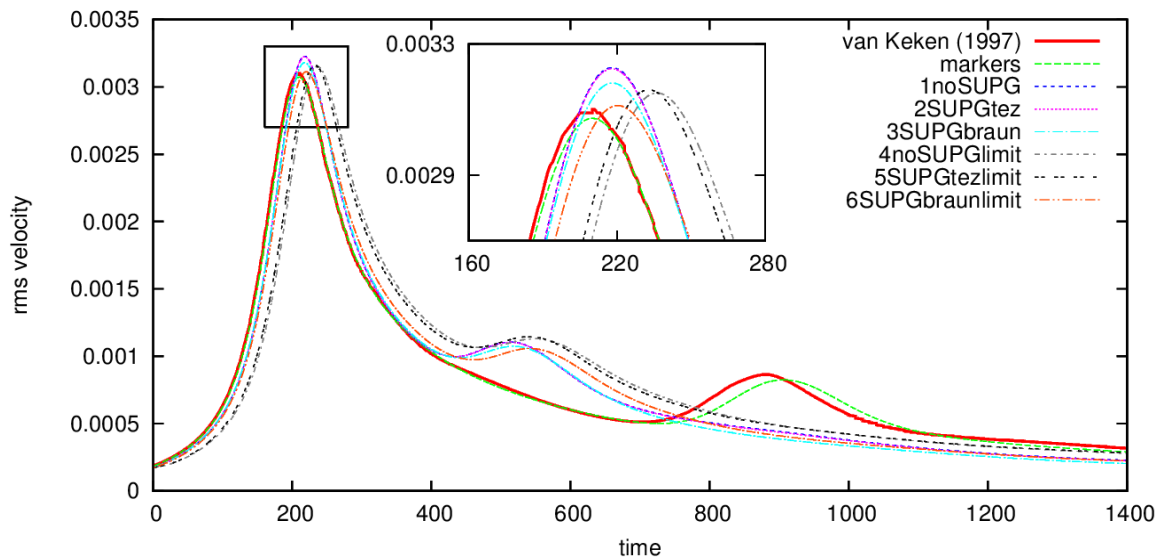

Figure 21: *The evolution of the root mean square velocity through time for model runs 1 to 6, the marker model and the results from the benchmark by van Keken et al. (1997). The inset shows a zoom-in of the first maximum v_{rms} peak.*
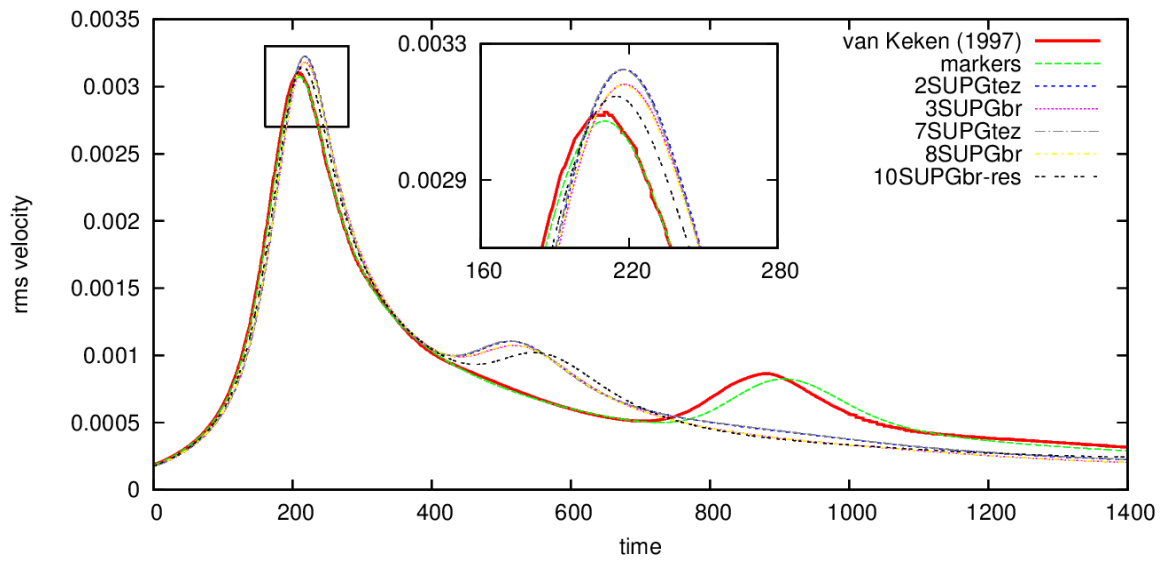
Figure 22: *The evolution of the root mean square velocity through time for model runs 2,3,7,8 and 10, the marker model and the results from the benchmark by van Keken et al. (1997). The inset shows a zoom-in of the first maximum v_{rms} peak.*
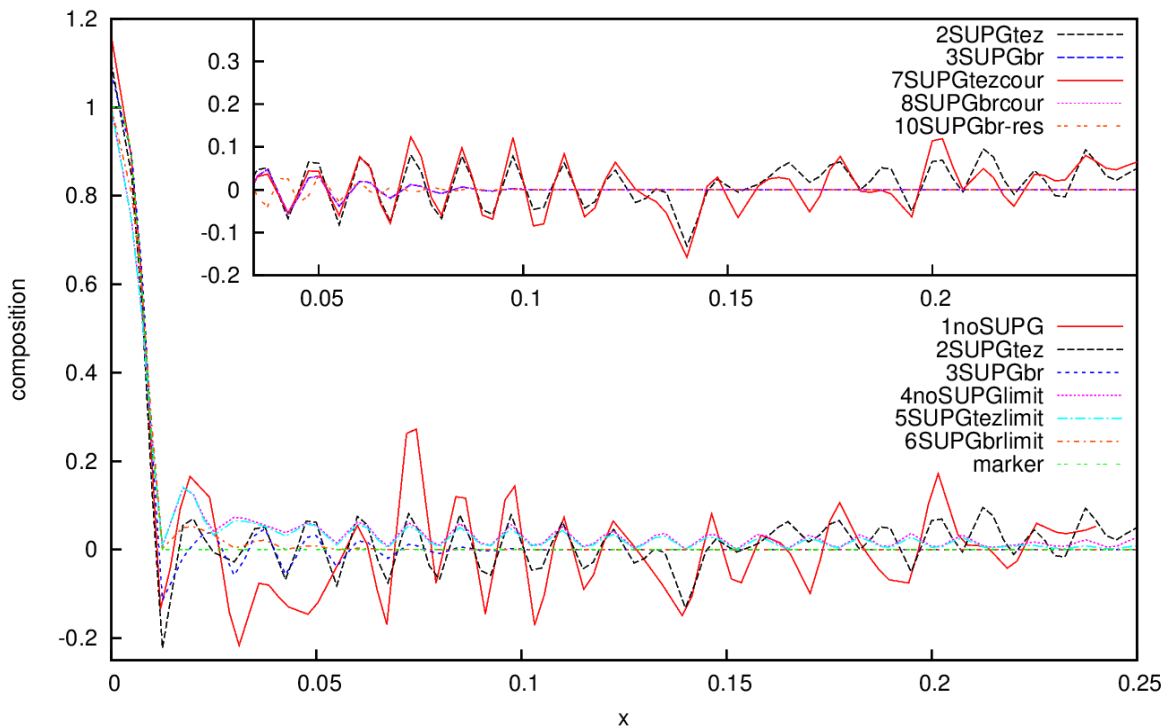

Figure 23: *Cross-section 1 from A: $x = 0$ to B: $x = 0.25$ at a height of $y = 0.3$ at t=1400. Models 1, 2, 3, 4, 5, 6 and the marker model are plotted in the main figure. The inset shows model 2, 3, 7, 8 and 10.*
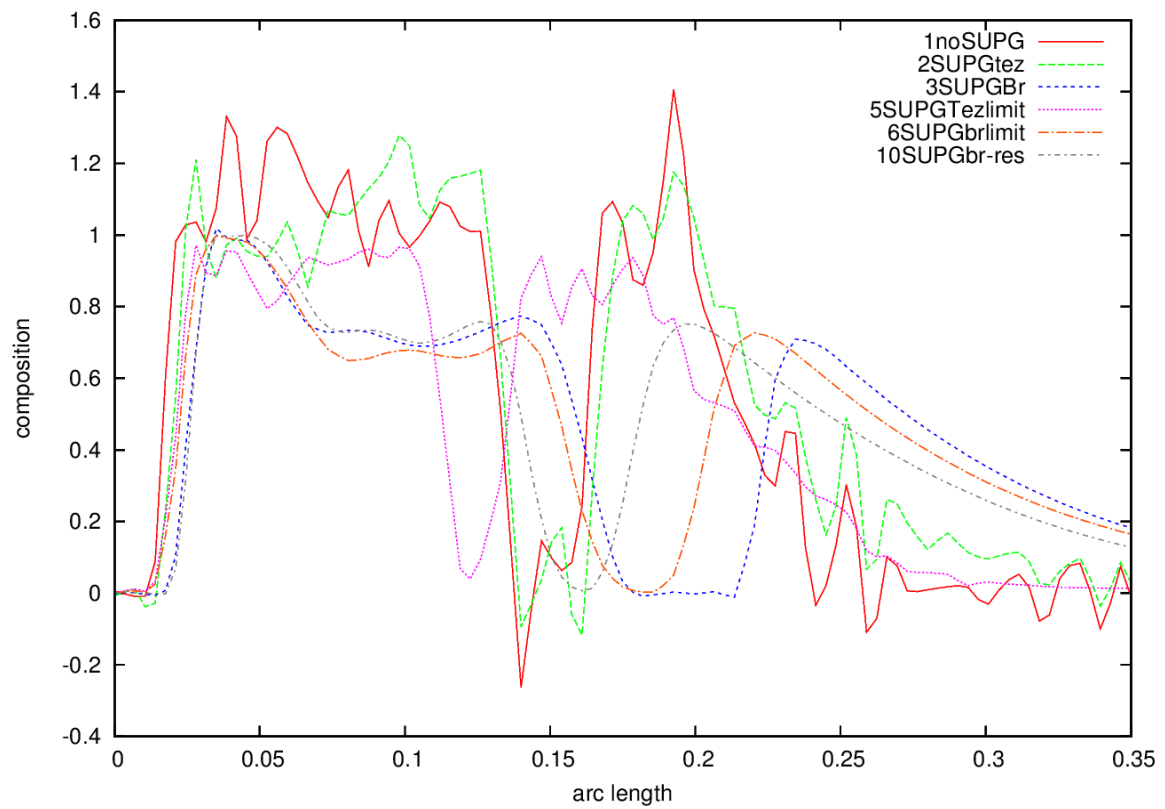
Figure 24: *Cross-section 2 from A: $y = 1$ to B: $y = 0.65$ at $x = 0.6$ at $t = 1400$. Models 3, 4, 5 and 6 are plotted.f*
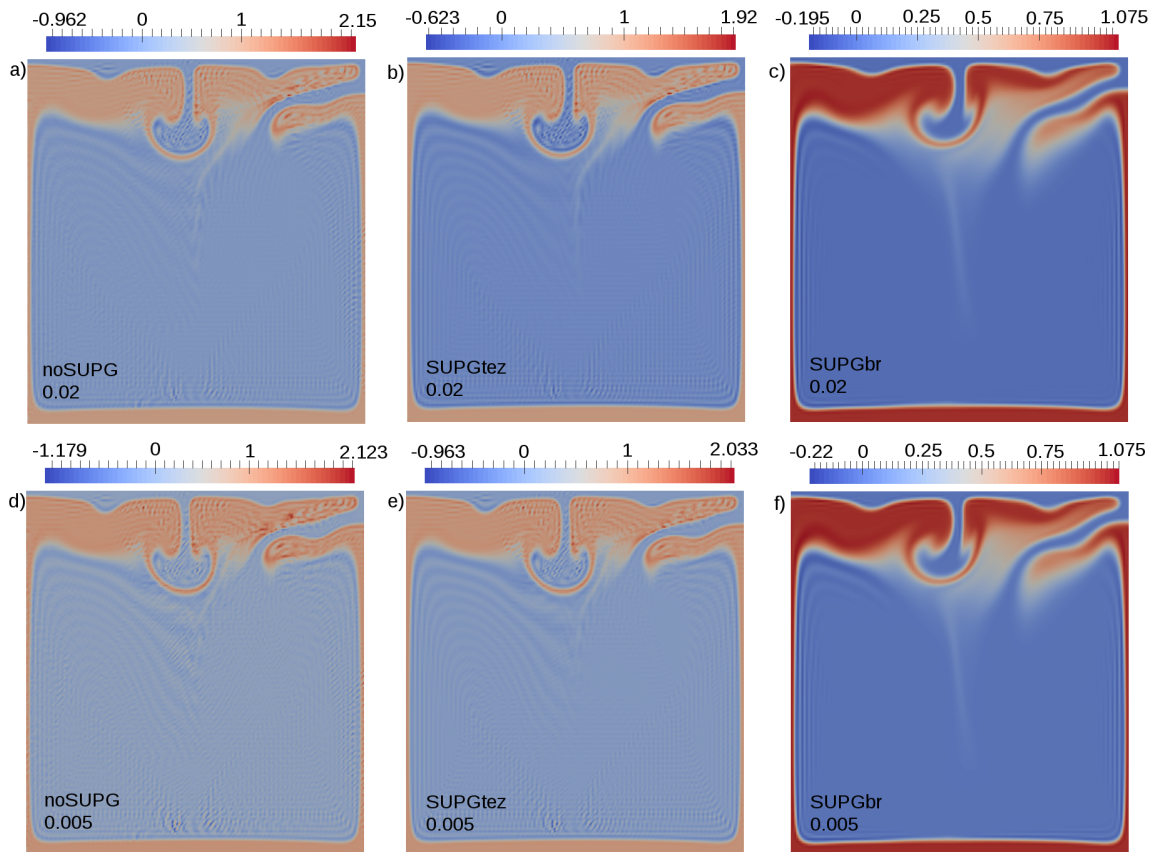
Figure 25: *The end result of the van Keken benchmark using a smooth interface between the materials given by eq. (77). a to c use a smoothing parameter of 0.02, d to f a parameter of 0.005. In a & d) no SUPG stabilizing scheme was used, in b & e) the SUPG scheme from Tezduyar and Osawa (2000) was used, in c & f) the stabilizing scheme from Braun (2003) has been used.*

7.2.3 The second $\mathbf{v}_{rms}$ peak

As previously mentioned, the second velocity peaks of the compositional field-model in the van Keken benchmark do not match the peaks produced by the marker models. There are discrepancies in the timing and height of these peaks. Bangerth et al. (2016b) showed that both the timing and height are dependent on the resolution used. This is due to the fact that the interface between the materials is described by a discontinuous function which is then interpolated between the nodal points resulting in an interface dependent on the resolution. With a higher resolution, the discontinuous boundary between the two materials is represented more accurately. Instead of an infinitely large slope between the materials, a gradual transition occurs which becomes smoother with decreasing resolution. This small scale difference determines the location of onset of the second plume as shown by Bangerth et al. (2016b) and explains the fact that the timing of the second peak does not converge.

A solution proposed by Bangerth et al. (2016b) to make the benchmark results less dependent on the resolution is to replace the discontinuous interface with a smooth one. A coarse resolution will in this case be able to correctly represent the smooth interface while a higher resolution will represent the interface using multiple elements. This solution decreases the difference in interface representation between different meshes and will thus result in a convergence of the second peak. Whether the timing and height of the second peak will agree with the marker models is a question that still stands. In order to test this, a new compositional field is defined given in equation (77).

$$c_\alpha = \frac{1}{2}\left(1 \pm \tanh\left(\frac{y_c - z}{0.02}\right)\right) \tag{77}$$

Here, c_α represents the compositional field 1 or 2 corresponding to either the + or - in the equation respectively, y_c represents the equation given by 75 and z the location in the domain with λ the domain ratio. The smoothing parameter which determines the slope of the interface is represented by the division by 0.02. This number can be increased (decreased) to decrease (increase) the slope of the interface.

Figure 25 shows the end results of the van Keken benchmark when using a smooth interface between the two
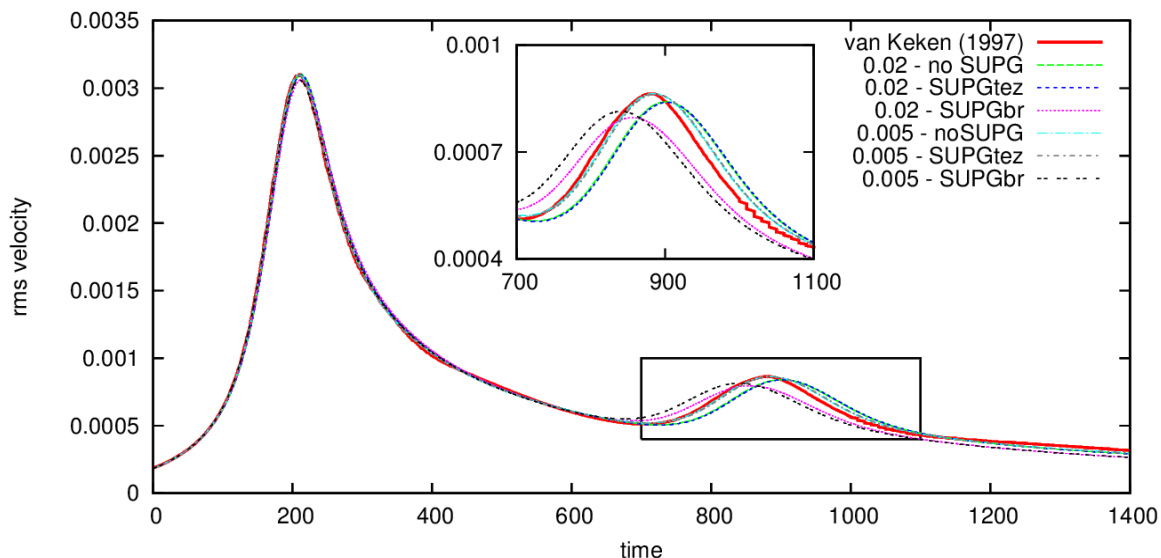
Figure 26: *The evolution of the root mean square velocities of the different models. The inset shows a zoom of the area located in the rectangle.*

materials. It can be seen that the outcome of the models using a discontinuous material boundary (Figure 19) do not differ significantly from the models using a smooth field. The biggest difference lies in the location and advancement of the second upwelling. Because this second upwelling occurs at a later time in the model (see Figure 26), it is located at a different position than the discontinuous models. The introduction of a smooth interface thus only affects the position of the second upwelling. No major changes in oscillations are observed besides a minor decrease in amplitude.

When comparing the top row of end results to the bottom row in Figure 25, it can be seen that using a steeper slope (0.005 with respect to 0.02) results in a higher over- and undershoot error. The effect on the spatial positions of the different up- and down-wellings is negligible.

Regarding the v_{rms} curves in Figure 26, it can be seen that its evolution differs significantly when using a smooth interface with respect to a discontinuous one. It can be seen that the timing and height of the first peak have converged to the results by van Keken et al. (1997). The timing and height of the second peak have also converged and lie close to the results of van Keken et al. (1997). The two models using the SUPG scheme from Braun (2003) give the least accurate results. The peak occurs too early and is lower than the peak from the original benchmark. Although the smaller smoothing parameter gave higher overshoot errors, it does give better results when looking at the root mean square evolution when compared to the results from the larger smoothing parameter.

7.2.4 Conclusion

I conclude that the SUPG stabilization scheme from Braun (2003) gives the best results when considering the overshoot error and the root mean square velocity evolution in the domain. The results can be improved by using a higher resolution or an artificial cut-off keeping the compositional values between 0 and 1.

The results can significantly be improved when using a smooth interface instead of a discontinuous interface. Both v_{rms} peaks converge and lie close to the original peaks. While the SUPG stabilization scheme from Braun (2003) gives the most accurate results in relation to the overshoot error, it does deviate when regarding the root mean square evolution and the spatial evolution of the model. The spatial evolution is affected due to the introduction of diffusion and the timing of the second plume. Cross-section 2 showed the significance of the diffusion as the locations of the material boundaries have faded and are located at entirely different positions. This effect must be kept in mind when using this stabilization scheme.

The choice of stabilization scheme depends on the use of a smooth interface or a discontinuous interface. When a discontinuous interface is used, the best results are obtained by using the Braun (2003) SUPG scheme and an artificial cut-off in combination with a high resolution. One has to keep in mind that due to diffusion, the results will be a smoothed-out version of the marker solution. When using a smooth interface, the choice is not as obvious. Although the Braun (2003) scheme produces the results with the smallest overshoot error, it does deviate from the root mean square results. The timing of the second peak is off, which could be due to the spatial evolution which is changed because of diffusion.

To conclude, no perfect solution exists for this problem. Concessions have to be made for each method but when using the right combinations of methods, it is possible to obtain results that lie very close to the marker-model results. The fact that such good results can be obtained with a first order approach is very promising for future models.
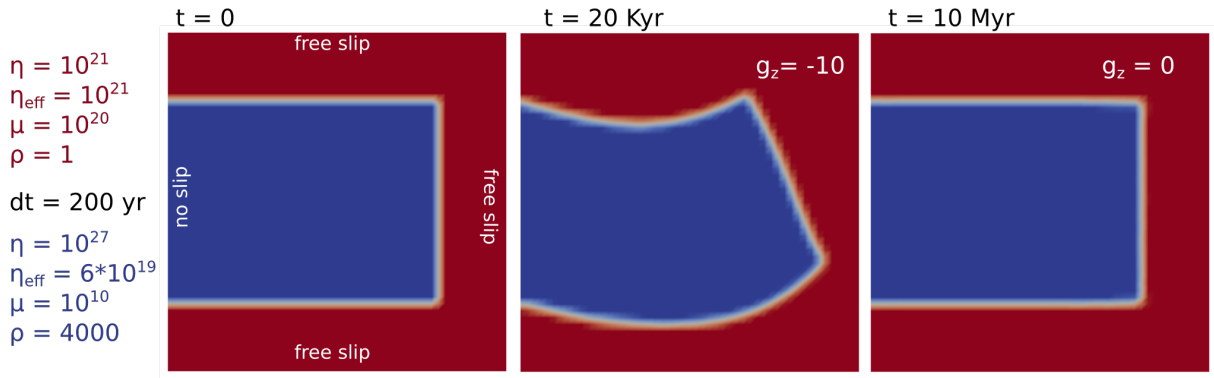
Figure 27: *Set-up and evolution of the benchmark from Gerya (2009). The properties of the two materials are given on the left, together with the initial configuration of the benchmark. The middle panel shows the position of the beam at t = 20 kyr, the moment the gravity is set to zero. The right panel shows the end result of the beam after a recovery period of 9980 kyr during the absence of gravity.*

8   Researching the combination of viscoelasticity and compositional fields

Materials and the stored stress in a viscoelastic-plastic model must be advected and followed through the employed domain. This is often done using a marker-based approach (Moresi et al., 2002, 2003; Popov and Sobolev, 2008; Farrington et al., 2014; Thielmann and Popov, 2015) where the material and stress tensor are stored on the markers which are then advected according to the velocity field. Another approach uses a purely Lagrangian grid (Funiciello et al., 2003; Kaus and Becker, 2007; Fourel et al., 2014) where the material boundaries are located on the mesh which is deformed according to the velocity field. The field based method described in Section 6 in combination with a viscoelastic-plastic rheology has not previously been researched. In the following section, the developed marker-based viscoelastic code is adapted in order to run using a combination of markers and compositional fields. The results can then be used to determine whether running a viscoelastic code is possible in combination with compositional fields and if so, are there concessions that have to be made in order to achieve this such as a higher resolution or a small Courant condition. This work presents the first research towards this combination. The effect of using fields in combination with elasticity is researched using the sinking beam benchmark (Gerya and Yuen, 2007; Gerya, 2010) which has also been performed to benchmark the viscoelasticity implementation (Section 9.2).

8.1   Set up of the benchmark

The sinking slab benchmark consists of a beam of elastic material which is placed in a weak and viscous surrounding medium. The initially unstressed beam is attached to the left domain boundary through boundary conditions. A stress is then applied to the beam in the form of gravity. The applied gravity force results in the deformation of the beam through bending. After 20 kyr, the gravity field is turned off and the elastic properties of the beam will then force itself to its original position.

The set-up of the benchmark is given in Figure 27. The beam is surrounded by a low-density, low-viscosity and high shear modulus medium of which the specifications are given in Table 2 and the Figure. The boundary conditions of the domain consist of a no slip condition at the left boundary where the slab is attached and free slip boundary conditions along all other sides. The results are calculated on a grid with a resolution of 51 by 51 nodal points and 25 markers per element. The resolution and Courant number will be varied when using compositional fields to see if the models perform better with a higher resolution/lower time step.

Table 2: *Specifications of the sinking beam benchmark from by Gerya (2009).*

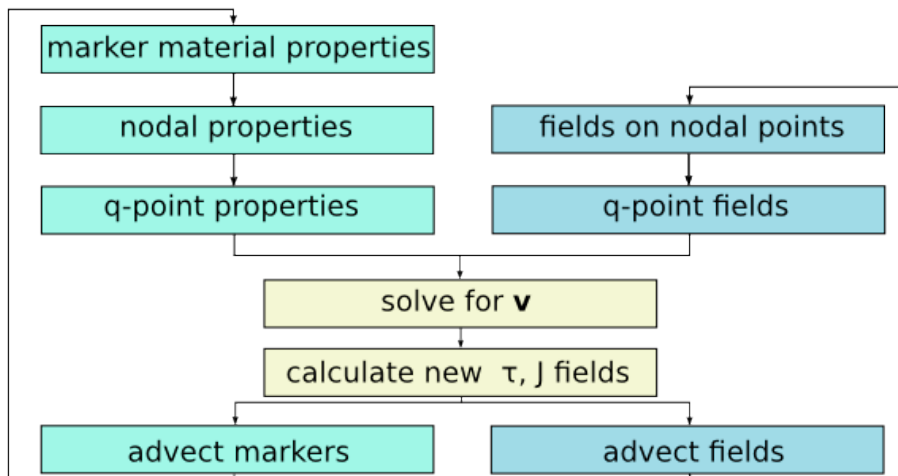| Material properties	Elastic slab	Surrounding medium
Density ρ [kg/m^3]	4000	1
Viscosity η [Pa· s]	10^{27}	10^{21}
Shear modulus μ [Pa]	10^{10}	10^{20}

Figure 28: *Diagram showing the structure of the hybrid viscoelastic model. The left column represents the marker based part of the code, the right column the field based part of the model. The yellow centre part shows when the two approaches join to solve for the velocity field.*

8.2 A hybrid viscoelastic model

A hybrid model using a marker and compositional field combination is first tested. In this hybrid version, the materials are traced using markers which contain the material properties. The stress and Jaumann field are tracked and advected using compositional fields. This hybrid model is used to circumvent the problems which arise when advecting discontinuous fields as is the case for material fields. It has been shown in earlier benchmarks that the advection of continuous smooth fields does not exhibit the problematic oscillations that arise for discontinuous fields. The stress and Jaumann field are both continuous fields and we should thus be able to advect them without difficulties. No fully field-based code is tested due to the oscillations that arise when advecting discontinuous material fields. Existing field based codes have more sophisticated methods to keep this under control and this therefore does not need to be tested. This test is solely developed in order to research the possibility of advecting the stress- and Jaumann fields using the advection method.

Besides researching the influence of the resolution and time step on the accuracy of the models, the influence of the introduction of an advection term in the stress expression is also tested (see Section 8.3).

8.2.1 Set-up of the hybrid viscoelastic code

The marker-based model is adapted to use fields to track and advect the stress and Jaumann fields. A schematic representation of the structure of the code is given in Figure 28. This hybrid code simultaneously works with markers and fields. The material properties are contained by the markers and the stress and Jaumann fields are stored on the nodes and advected using fields. In the schematic diagram, the green, left column shows the marker-based part of the code. The blue, right column represents the field-based part of the model. The yellow column represents the part where the two methods combine.

First, the material properties contained by the markers are extrapolated to the nodal points by averaging over all markers in the elements surrounding the nodal point. These nodal properties are then extrapolated to the quadrature points (equation 71) to be used in the finite element formulation to solve for the velocity field. The fields stored on the nodal properties (accumulated stress field and Jaumann field) are interpolated to the quadrature points and also used to solve for the velocity field. Then, the new accumulated stress and rotation rate are calculated on the nodal points and the velocity field is used to advect the markers using a 4th order Runge-Kutta scheme and the advection equation is used to calculate the stress and Jaumann fields.

The first model will be run with the specifications used in the original benchmark. A resolution of 51 by 51 will be used together with a Courant number of $C = 0.333$. After this model, the resolution will be increased while the Courant number will be decreased to find the dependence of the hybrid model on these variables. The model specifications are given in Table 3. 1model_st is the model using the original specifications as used in the marker-based model.

8.2.2 Testing the marker- and field-based combination

The maximum velocities of the benchmark models are shown in Figure 29. It can be seen in the top Figure that the maximum velocities of the hybrid model lie close to the results produced by the marker model. In order to determine the accuracy of the hybrid model, two insets are given that contain an enlargement of parts of the curve from the top panel. The position of the left inset is shown by the rectangle projected in the top panel. The right panel shows a zoom of the final 250 kyr of the model run which are not shown in the top panel. The two bottom panels clearly show that the hybrid models tend to be faster than the marker models. It can also be seen that the results are grouped according to the resolution used. The models using the lowest resolution (51 by 51), models 1, 4 and 5, lie furthest away from the marker model results. The models using the highest resolution, 151 by 151, models 3, 6 and 9, lie closest to the marker model results.The models using a resolution of 101 by 101, models 2, 5 and 7, lie in between these two groups. It can also be seen that the used Courant number provides a fixed contribution to the maximum velocity. Within the resolution groups, the lowest Courant number lies furthest away from the marker model and the highest Courant number lies closest to the marker model results. Increasing both the resolution and Courant number thus leads to a result which lies closer to the marker model outcome. The same conclusions can be drawn when looking at the right panel showing the last 250 kyr. The same trend concerning the resolution and Courant number are observed here.

The decrease in maximum velocity when using a larger resolution is also observed for the marker model. $marker\_model\_101$ shows the maximum velocity for a resolution of 101 by 101. It can be seen that the maximum velocity is lower as was previously observed when using the marker model. Using a lower Courant number does not affect the outcome for the marker model (not shown in the graph).

The relative difference in velocity between the model lying closest to the marker model results ($3model\_03$) at 20 kyr is 0.03%. At the end of the model, at 1 Myr, the error is approximately 17%. The hybrid model thus produces accurate results up to the moment the gravity is set to zero. This is verified by Figure 30 where the positions of the beam at $t = 20$ kyr and $t = 1$Myr are given. It can be seen that the results at $t = 20$kyr are equal to the marker model but deviate at $t = 1$Myr. The beam is twisted at the corners. Both the twisted corners and the velocity deviation could be explained by erroneous stress fields in the hybrid model since the stress field is the sole force acting upon the beam after switching off the gravity. This means that it greatly influences the velocity and shape in which the beam returns. Oscillations present in the stress field could then explain the large error that arises after switching off the gravity field.

Considering the stress fields shown in Figure 31, it can be seen that at $t = 20$kyr, the stress fields of the two hybrid models are very similar to the marker model stress field. There are some oscillations at the lower and right boundary of the beam, but their amplitude is small. No large differences are visible between the two hybrid models. However, when looking at second row, at $t = 1$Myr, the oscillations have grown to a significant size. The large scale structures present in the marker model stress field are still visible, but they are disrupted by large oscillations. Note that the scale of the marker model has been used for all three figures and that the maximum amplitude size of the two hybrid models is an order of magnitude larger than the marker model. This disturbed stress field could explain the deviating velocity field. The oscillations arising in model 9, using a lower Courant number, are larger than the ones in model 3. They have a larger wavelength and are more pronounced resulting in higher forcings from the stress field which could explain the larger velocity.

Table 3: *Model specifications for the sinking beam benchmark using the hybrid viscoelastic model.*

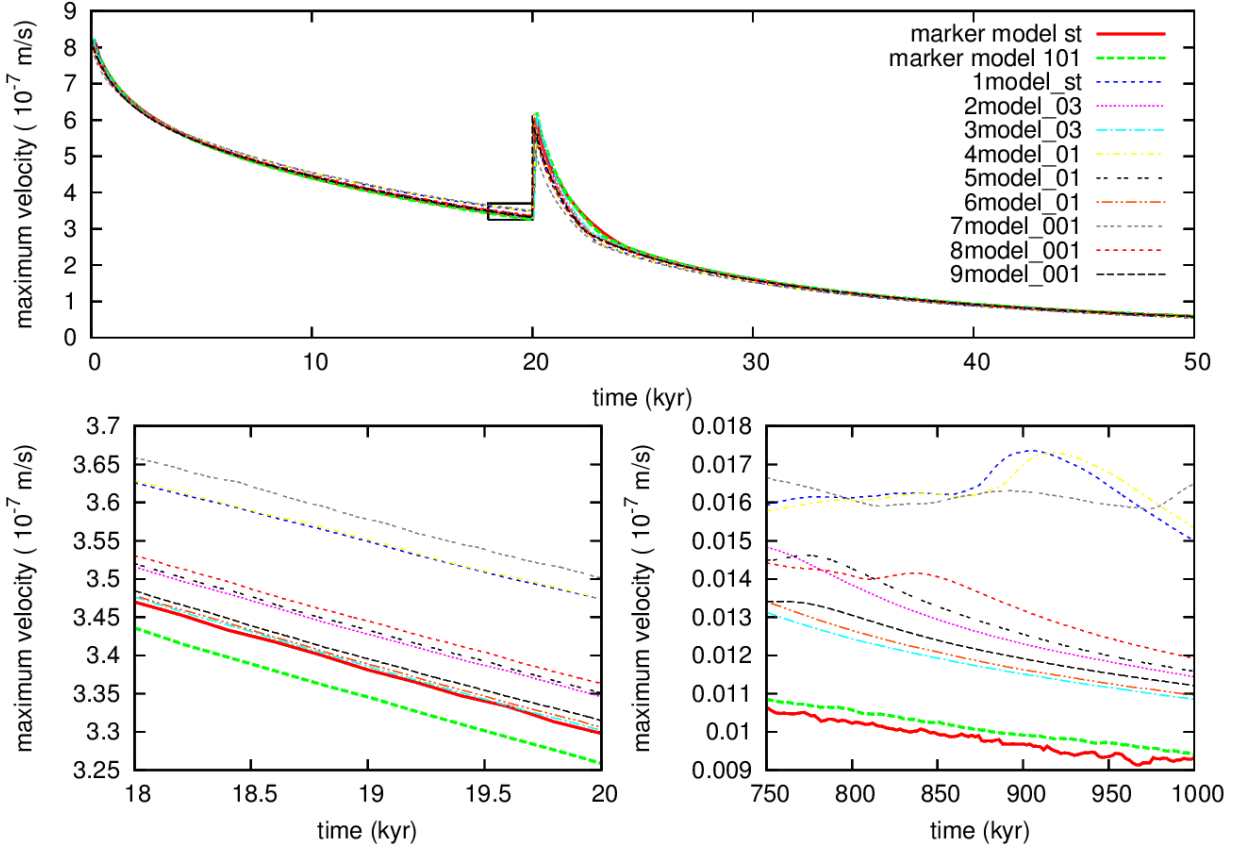| Model	Resolution	Courant number
1model_st	51 x 51	0.333
2model_03	101 x 101	0.333
3model_03	151 x 151	0.333
4model_01	51 x 51	0.1
5model_01	101 x 101	0.1
6model_01	151 x 151	0.1
7model_001	51 x 51	0.01
8model_001	101 x 101	0.01
9model_001	151 x 151	0.01

Figure 29: *Three panels showing the maximum velocity from the hybrid model together with the maximum velocity from the marker model. The top panel shows the maximum velocity up to 50 kyr. The bottom left panel shows an enlargement of the area enclosed by the box in the top panel. The bottom right panel gives the maximum velocities from 750 kyr to 1 Myr which are not shown in the top panel. All hybrid models are given, together with two marker models. Marker_model_st uses the original specifications. Marker_model_101 uses a resolution of 101 by 101.*

8.2.3 Conclusion

The hybrid model performs very well up to $t = 20$kyr after which the gravity is set to zero. The stress then becomes the sole forcing which returns the beam to its original position. Possibly due to the arise of oscillations, the model misbehaves slightly resulting in a 17% error in maximum velocity. The results from this first-order hybrid model are very promising. The model works up to $20kyrs$ and when a more sophisticated stabilization is used to suppress the oscillations arising during the return of the beam, it is very likely that it will lead to results which lie within the error margin. The use of fields to advect the stress and Jaumann field does require the use of a higher resolution in order to agree with the marker results. When choosing between a fully maker based model, or using a hybrid model, this downside has to be taken under consideration. However, since the field approach requires less memory storage, the higher resolution might weigh up to the decrease in memory needed when running high resolution 3D models. It must be noted that the results obtained for the marker-based code also vary for different resolution and that this benchmark has a dependence on resolution and no unique solution exists.

8.3 Benchmarking using an additional advection term

von Tscharner and Schmalholz (2015) showed that when a Lagrangian approach is used, the advection term which is present in the material derivative can be neglected leading to the following definition of the objective stress rate:

$$\dot{\boldsymbol{\tau}}^{t+\Delta t} \approx \frac{\boldsymbol{\tau}^{t+\Delta t} - \boldsymbol{\tau}^t}{\Delta t} - \boldsymbol{\omega}^t \boldsymbol{\tau}^t + \boldsymbol{\tau}^t \boldsymbol{\omega}^t \tag{78}$$

However, when using compositional fields to track and advect materials or the accumulated stress fields, the model can no longer be described as being Lagrangian, but is now Eulerian. Neglecting the advection term in
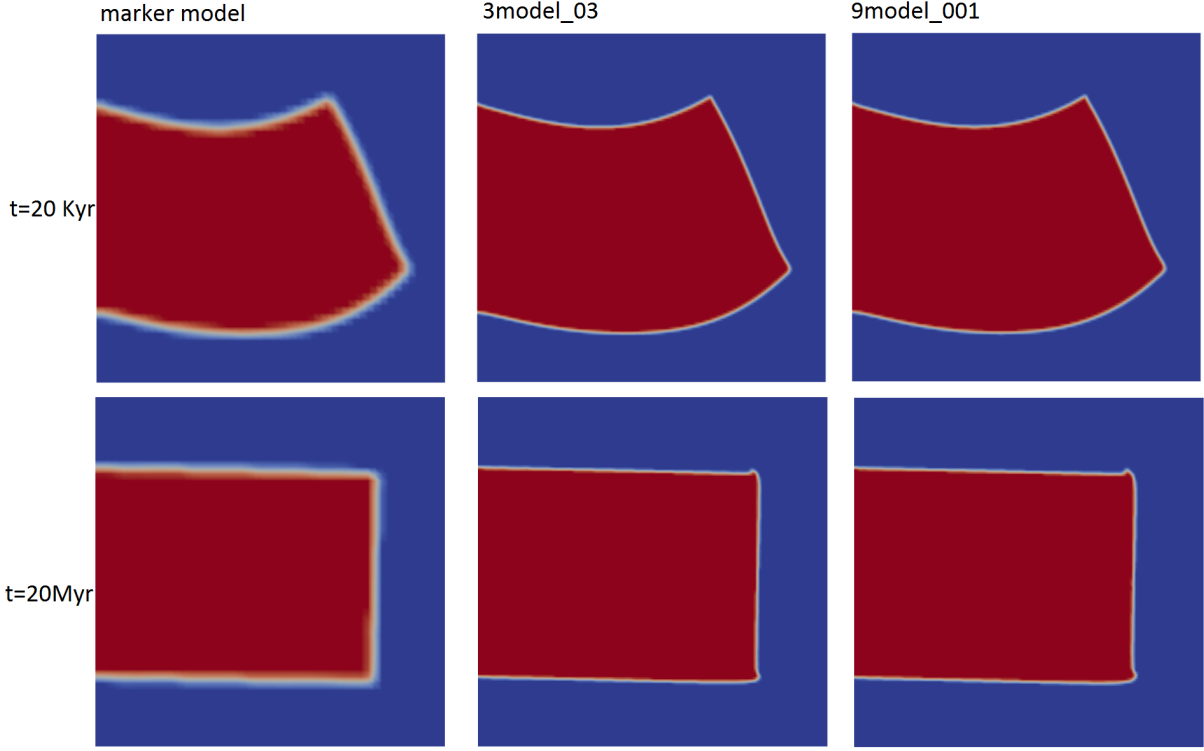
Figure 30: *The position of the beam at $t = 20kyr$ and $t = 1Myr$ for the marker model, 3model_03 and 9model_001.*

the material derivative is in this case no longer allowed. This means that the expression for the stress rate has to be adapted. The expression for the material derivative now becomes

$$\frac{D\tau_{ij}}{Dt} = \frac{\partial \tau_{ij}}{\partial t} + v_k \frac{\partial \tau_{ij}}{\partial x_k} \tag{79}$$

resulting in the following expression for the objective stress rate:

$$\dot{\boldsymbol{\tau}}^{t+\Delta t} \approx \frac{\boldsymbol{\tau}^{t+\Delta t} - \boldsymbol{\tau}^t}{\Delta t} - \boldsymbol{\omega}^t \boldsymbol{\tau}^t + \boldsymbol{\tau}^t \boldsymbol{\omega}^t + \mathbf{v}^t \cdot \nabla \boldsymbol{\tau}^t \tag{80}$$

Implementing this definition of the material derivative in equation (15) and following the same steps as in Section 3.2, leads to the following expression for the accumulated stress

$$\boldsymbol{\tau}^{t+\Delta t} = 2\eta_{eff} \, \dot{\boldsymbol{\varepsilon}}^{\,t+\Delta t} + \frac{\eta_{eff}}{\mu \Delta t} \, \boldsymbol{\tau}^t + \frac{\eta_{eff}}{\mu} \left(\boldsymbol{\omega}^t \boldsymbol{\tau}^t - \boldsymbol{\tau}^t \boldsymbol{\omega}^t \right) - \frac{\eta_{eff}}{\mu} \left(\mathbf{v}^t \cdot \nabla \boldsymbol{\tau}^t \right) \tag{81}$$

where the last term represents the added advection term. It can be written as

$$\mathbf{v}^t \cdot \nabla \boldsymbol{\tau}^t = u^t \begin{pmatrix} \frac{\partial \tau_{xx}^t}{\partial x} \\ \frac{\partial \tau_{yy}^t}{\partial x} \\ \frac{\partial \tau_{xy}^t}{\partial x} \end{pmatrix} + v^t \begin{pmatrix} \frac{\partial \tau_{xx}^t}{\partial y} \\ \frac{\partial \tau_{yy}^t}{\partial y} \\ \frac{\partial \tau_{xy}^t}{\partial y} \end{pmatrix} = \mathbf{A}^t \tag{82}$$

The advection term appears in the finite element equation on the right hand side.

$$\left\{ \int_{\Omega_e} \lambda \mathbf{B}^T \mathbf{K} \mathbf{B} \, d\Omega + \int_{\Omega_e} \eta_{eff} \mathbf{B}^T \mathbf{C} \mathbf{B} \, d\Omega \right\} \mathbf{V}^{t+\Delta t} = \int_{\Omega_e} \mathbf{N}_f - \frac{\eta_{eff}}{\mu \Delta t} \mathbf{B}^T \left[\mathbf{T}^t + \Delta t \mathbf{R}^t - \Delta t \mathbf{A}^t \right] d\Omega \tag{83}$$

The additional advection term has to be implemented in both the finite element formulation and the calculation of the stress. The calculation of the spatial derivatives is given in Appendix A.2.
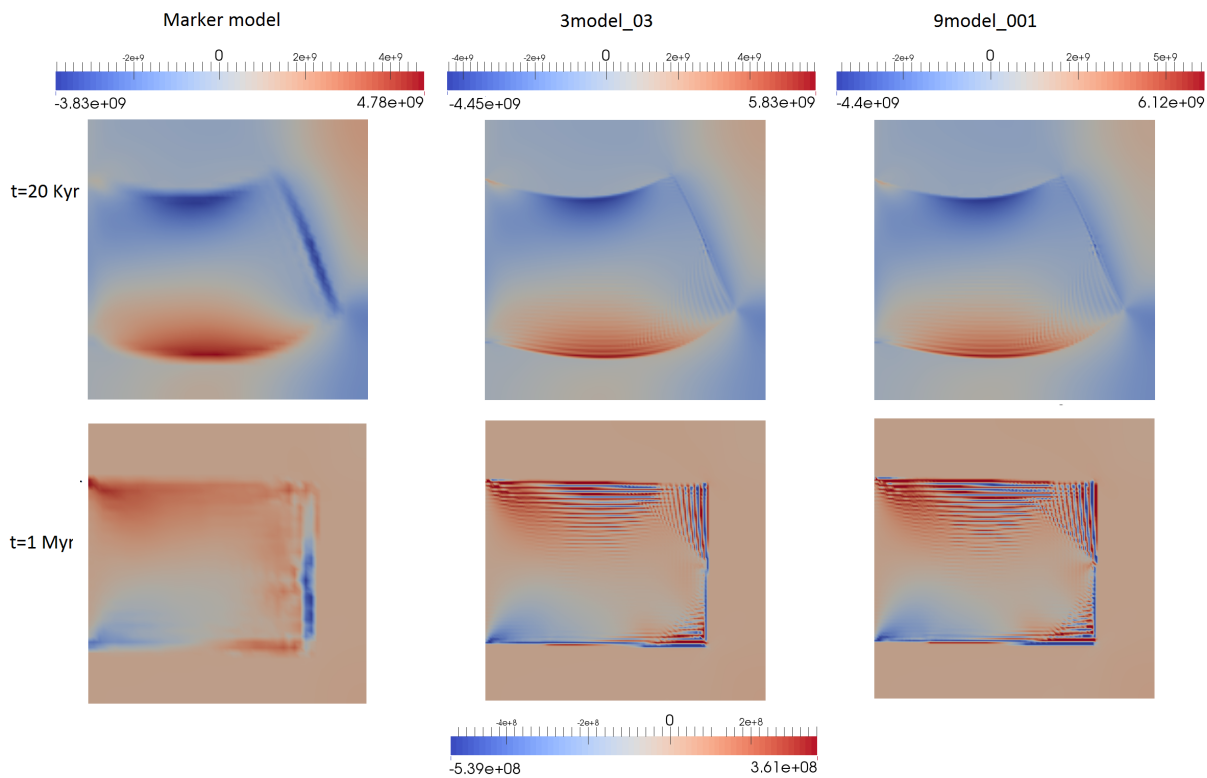
52

Figure 31: *The stress distribution (τ_{xx}) through the beam at $t = 20kyr$ and $t = 1Myr$ for the marker model, 3model_03 and 9model_001. Note that the same scale is used for the bottom three figures but that the amplitudes in the middle and left figure may exceed this scale.*

8.3.1 Set-up of the hybrid viscoelastic code with the additional advection term

The set-up of the benchmark is equal to the set-up presented in Section 8.2.1. The difference lies in the presence of the additional advection term in the expression for the accumulated stress and the finite element expression. In order to research the effect of the advectional term and whether it increases the accuracy of the model, several models from the previous section will be compared to models run with the same set-up using the extra advection term. These models are called 1amodel, 2amodel and 3amodel and carry the same specifications as their non-advection term counterparts, 1model_st, 2model_03 and 3model_03 respectively.

8.3.2 Results

The maximum velocity results of the advection models are shown in Figure 32. There, the maximum velocity of the advection models together with their non-advection counterparts is plotted. Due to the similarity of the curves to Figure 29, only the enlargements are shown. The left panel shows a zoom of the box drawn in Figure 29, the right panel gives the evolution of the maximum velocity for the last 500kyrs. It can be seen in the left panel that using an advection term lowers the maximum velocity. The maximum velocity of 3amodel is slightly too low. The right panel shows that after the removal of the gravity, the advection models give significantly worse results. Where the best non-advection model deviates by 17% from the marker model, the best performing advection model, 3amodel, produces an error of approximately 61%. These results are confirmed when looking at the spatial evolution of the beam through time (Figure 33). The panels in the middle show the position of the beam at the moment the gravity is turned off, and at the end of the model. Where 3model_03 is equal to the marker model at 20kyrs, the advection term model deviates. It has been bend further down causing the right of the beam to bend upwards more than the other two models. The right side of the beam also shows a different curvature. Looking at the end results, the advection model performs worse than the hybrid model. The corners of the beam in the hybrid model are only slightly curved, the corners of the advection model have been curved further resulting in a twist of the right edge of the beam.

When looking at the stress field (τ_{xx}) for the advection term model in Figure 34 the effect of adding the advection term becomes visible. The stress field is distorted and large peaks are present in locations where they are not expected to be. The maximum amplitude of the stress field is three times as high as the hybrid
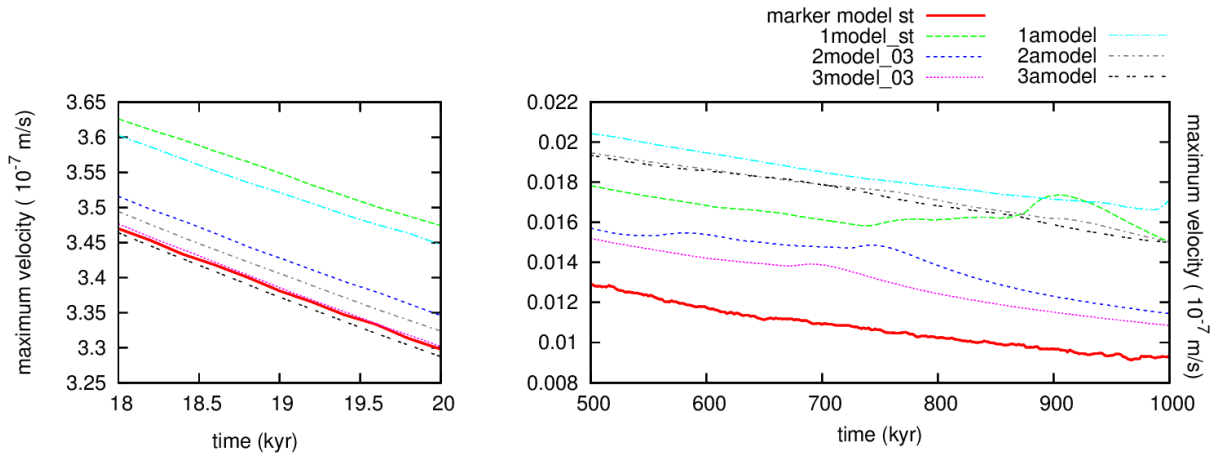
Figure 32: *The maximum velocity curves when using the additional advection term for the marker model and the hybrid models 1model_st, 2model_03, 3model_03 using no additional advection term, and the models 1amodel, 2amodel, 3amodel, using the advection term. The Courant number used in all models is $C = 0.333$ and the resolution is 51 by 51 for models 1 and 1a, 101 by 101 for models 2 and 2a and 151 by 151 for models 3 and 3a. The left panel shows a zoom of the maximum velocity in the box shown Figure 29. The right panel shows the maximum velocity in the last 500kyrs*

3model_03 model. Both are more than an order of magnitude larger than the maximum stress in the marker model.

Looking at the stress field produced by the advection term model, the curved corners of the beam present at the end of the model run and the error of 61% of the maximum velocity, it seems that it is advisable to disregard the use of the advection term as it does not increase the accuracy of the model. The erroneous fields arising after the implementation of the advection term might be caused by the fact that the advection term is already captured in the advection equation solved to advect the fields. This results in a double contribution of the advection resulting in an overcompensation and runaway patches in the obtained fields. The additional advection term that is necessary in Eulerian codes based on deformable grids might therefore be redundant in field-based codes which already incorporate advection effects.

8.4   Using a fully field-based elastic code

Due to the problems arising when advecting discontinuous fields as is the case for the advection of compositional material fields when using a first order approach, it is beyond the scope of this work to develop a fully field-based viscoelastic code. However, the results obtained using the very simple, hybrid model implemented here, are surprisingly accurate up to 20 kyrs. The fact that such a high accuracy can be reached for a first order model leads to the expectation that a viscoelastic rheology can be successfully implemented together with the field advection approach. When more sophisticated methods are used to suppress the arising oscillations, the results are expected to resemble those from marker-based models.
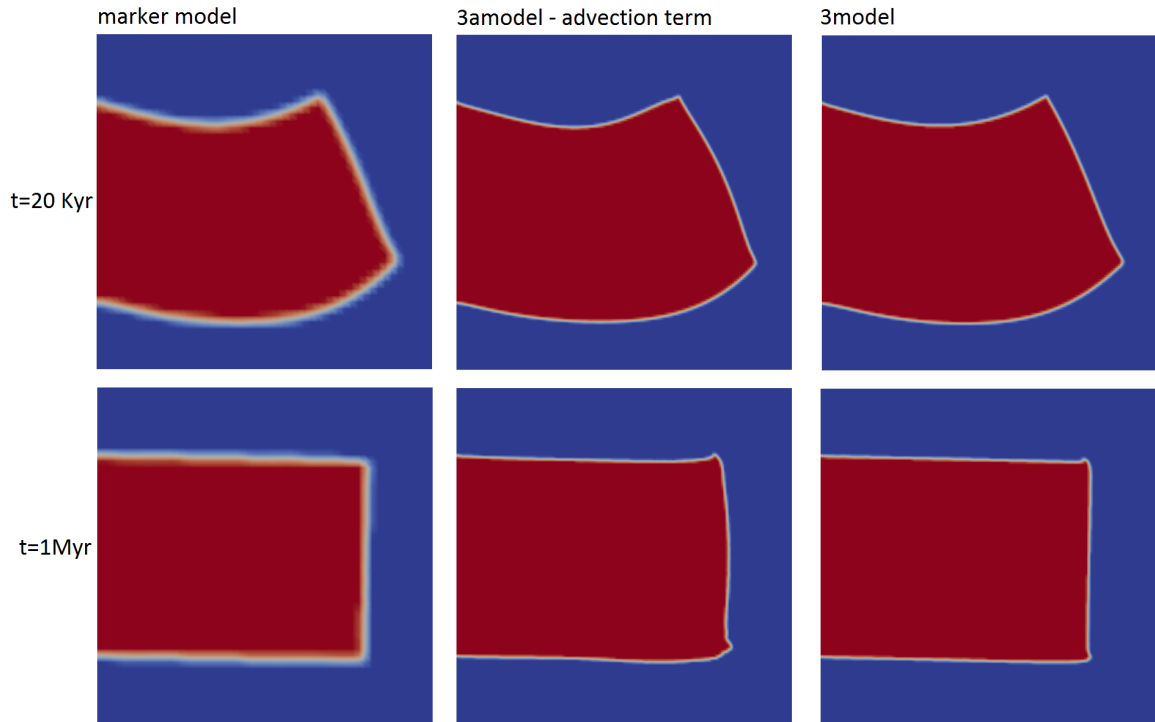
Figure 33: *The position of the beam at t = 20kyr and t = 1Myr for the marker model, the advection model 3amodel and the non-advection model 3model_03.*
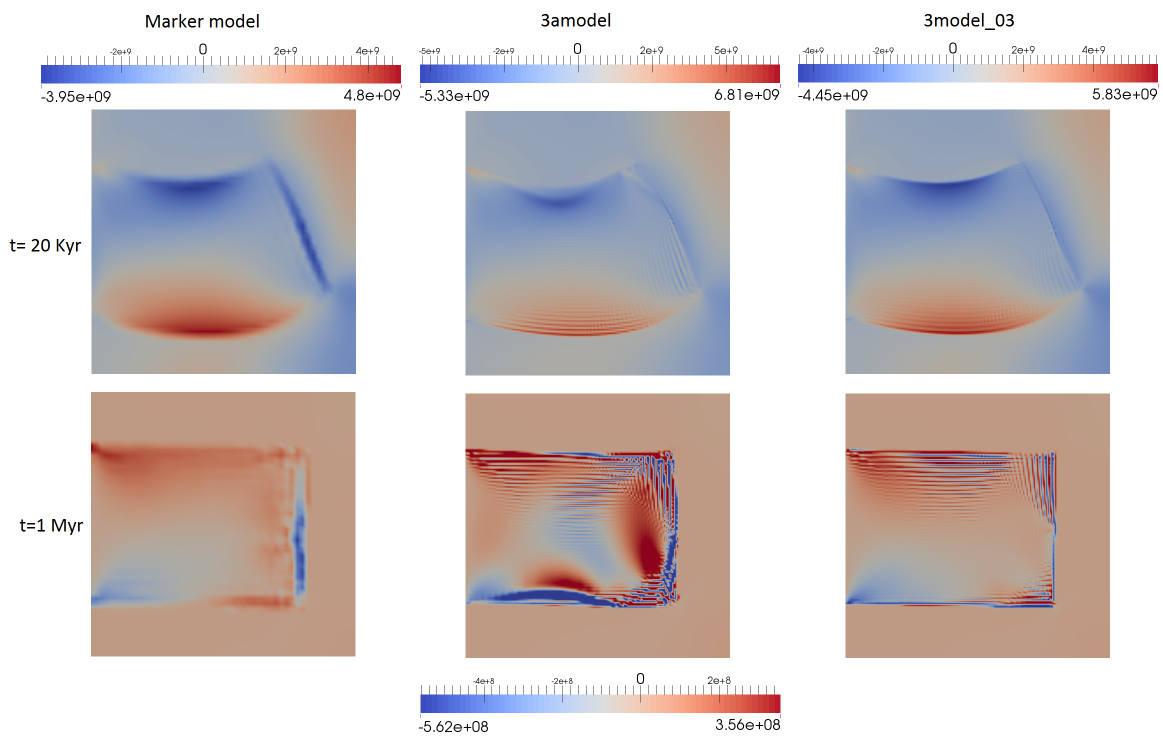

Figure 34: *The xx stress fields (τ_{xx}) for the marker model, the advection model 3amodel and 3model_03 without the advection term. The top row shows the stress field at t = 20kyr just before the gravity field is switched off. The bottom row shows the stress field at the end of the model run. Note that the same scale is used for the bottom row, and that the maximum amplitude of the oscillations for the 3model_03 and 3amodel lie an order of magnitude higher.*
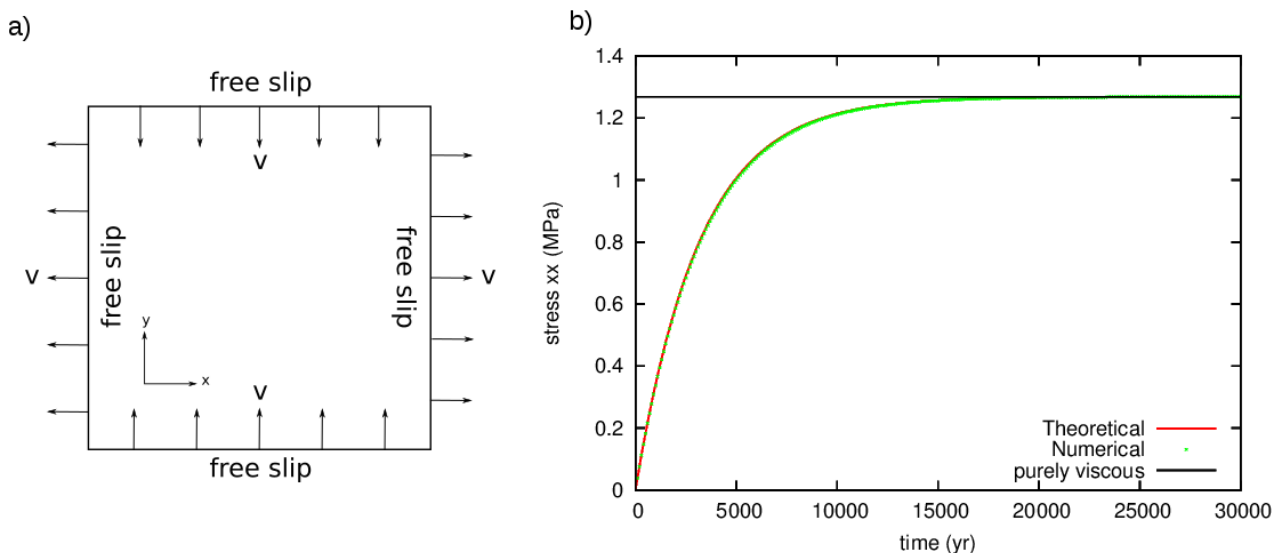
55

Figure 35: *The set up of the stress build-up benchmark is shown on the left. a) All domain sides have a free slip boundary condition, and pure shear velocity conditions are prescribed. Adapted from Gerya (2010). b) The results of the benchmark. The deviatoric stress τ_{xx} build-up with time is shown for the analytical and numerical solutions. The stress evolution for the purely viscous case is also shown.*

9 Benchmarking the viscoelastic(-plastic) implementations

In this section, several benchmarks are performed to validate the viscoelastic(-plastic) implementation. All benchmarks have either an analytical solution or available solutions that the obtained results can be compared with. The viscoelastic-plastic implementation is benchmarked using the following benchmarks:

- Elastic stress-build-up in a viscoelastic Maxwell body by Gerya and Yuen (2007); Gerya (2010); Choi et al. (2013)

- The sinking beam benchmark by Gerya (2010)

- Flexure of an elastic plate Choi et al. (2013)

- The brick experiment from Kaus (2010)

- Shortening of a viscoelastic-plastic block by Gerya (2010)

9.1 Stress build-up in a viscoelastic Maxwell body

The first benchmark performed to test the viscoelastic implementation considers the stress build-up present in a viscoelastic Maxwell body. Contrary to stressed viscous materials, viscoelastic materials gradually build-up stress when sheared after which a transition to viscous deformation occurs.

An unstressed, incompressible viscoelastic Maxwell medium is subjected to a velocity field resulting in pure shear. The increase of the accumulated stress with time is given by an analytical solution:

$$\boldsymbol{\tau} = 2\eta \, \dot{\boldsymbol{\varepsilon}} \left(1 - e^{\frac{-\mu t}{\eta}} \right) \tag{84}$$

with t time, η the prescribed material viscosity and μ the prescribed material shear modulus. The velocity prescribed at all boundaries equals $v = 1$ cm/yr in magnitude yielding a constant background strain rate of $\dot{\varepsilon} = 3.171 \times 10^{-15}$. The prescribed viscosity $\eta = 10^{21}$ Pa s, the shear modulus $\mu = 10^{10}$ Pa and a zero gravity is prescribed. The domain set-up is given in Figure 35 on the left.

Figure 35 shows the results of the benchmark. It can be seen that the numerical stress build-up obtained agrees with the analytical solution validating our adopted numerical method for this benchmark.

9.2 The sinking beam benchmark

The implementation of the viscoelastic formulation is also benchmarked using the sinking beam set-up from Gerya (2010). As described in Section 8.1, the sinking slab benchmark comprises of an elastic beam placed in a
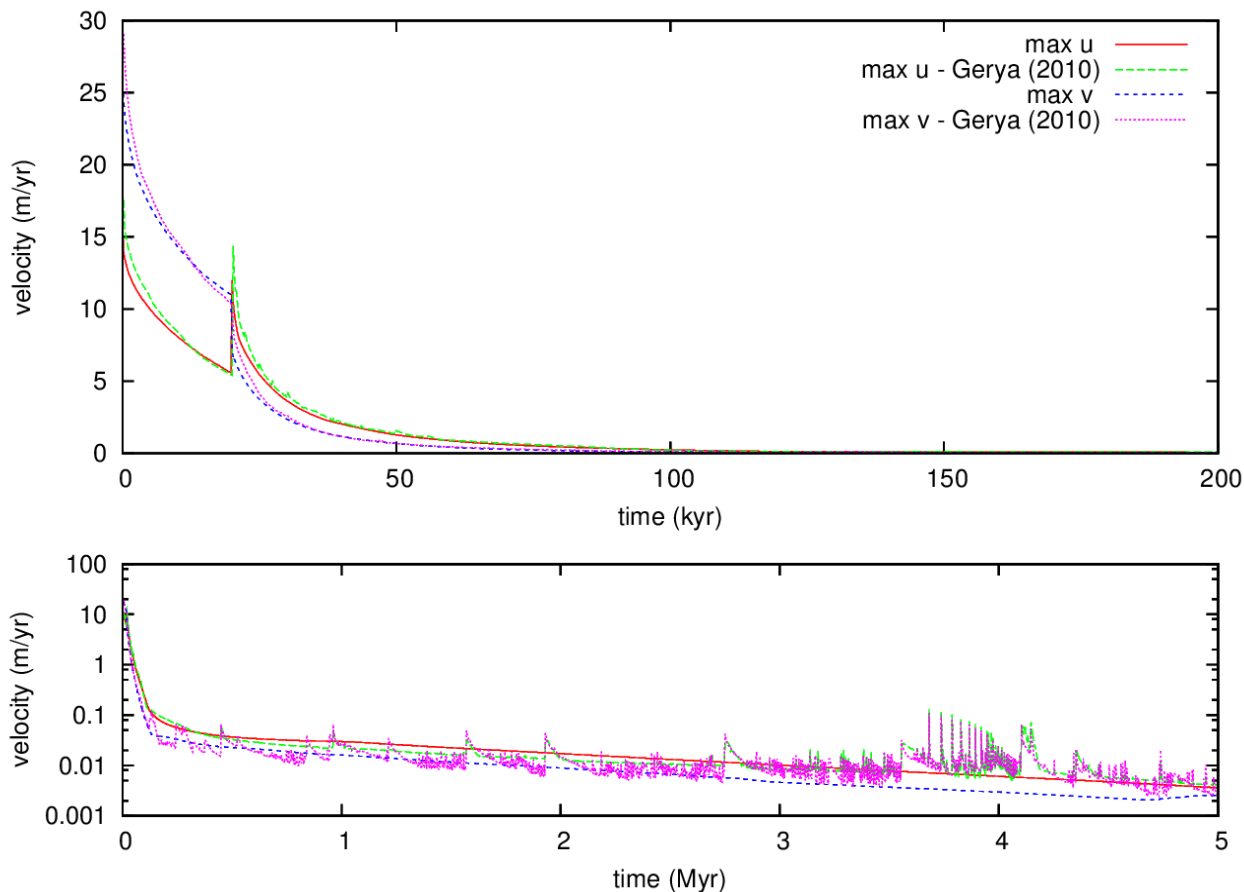
Figure 36: *Results of the sinking beam benchmark. Top panel shows the maximum horizontal and vertical velocity up to 200 kyr obtained from this study and the code used in Gerya (2010), the bottom panel shows the maximum horizontal and vertical velocity up to 5 Myr. Note the logarithmic scale in the bottom panel.*

weak viscous medium. The elastic beam is stressed by applying a gravity force resulting in the bending of the beam. After 20 kyr, the gravity is set to zero. Because the Maxwell time of the elastic beam is longer than the time of deformation (3170 Gyr compared to 20 kyr), stresses are stored throughout the deformation time and subsequently released after cessation of the applied body force. This results in the beam returning to its original position. The properties of the two materials and the prescribed boundary conditions are given in Figure 27. The details of this benchmark can be found in Section 8.1. The Courant condition applied is $C = 0.03$ and a resolution of 50 by 50 elements is used.

9.2.1 Results

Figure 36 shows the maximum horizontal and vertical velocity in the domain through time obtained for the model from this study and the code used in Gerya (2010). The first 200 kyr is shown in the top panel. The bottom panel shows the evolution of the maximum velocity through 5 Myrs. It can be seen in the top panel that the results are in agreement with the results from Gerya (2010). The bottom panel shows that the velocities obtained with the model developed in this study produces smoother and more regular results than the model from Gerya (2010). A steady, smooth decrease in velocity is observed, as is expected due to the fact that the beam slows down as it approaches its original position due to decreasing stresses. Figure 37 shows the beam has returned its original position after $t = 10$ Myr.

The agreement between our results and the results from Gerya (2010) leads to the conclusion that the benchmark has succesfully been performed. The results obtained are smoother and more regular than the reference velocities and the beam wholly returns to its starting position. These results validate the implementation of the viscoelastic rheology.
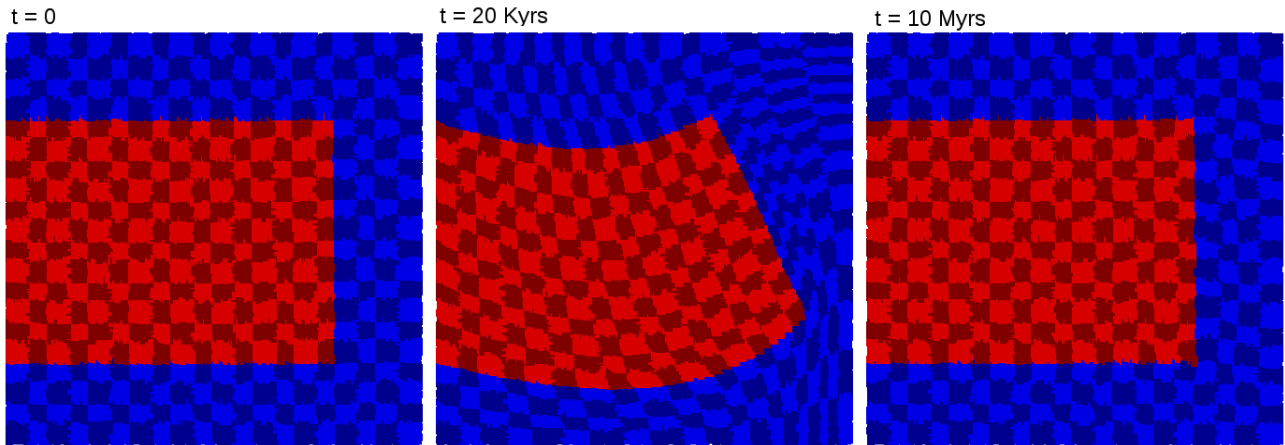
Figure 37: *The position of the elastic beam at t=0 yrs (left), t = 20 kyrs (middle) and t=10 Myrs.*

9.3 Flexure of an elastic plate

The viscoelastic implementation is also benchmarked using a set-up by Choi et al. (2013). An elastic plate is loaded resulting in flexure of the plate.

A plate of 50 km long and 5 km in height is pushed up from below at the right end of the plate by a low density elastic inclusion. The inclusion has the same properties as the plate but with a lower density. The plate and elastic inclusion overlie a viscous mantle. Figure 38 and Table 4 give the initial configuration and the material properties respectively.

The lower density of the elastic inclusion creates a gravitationally unstable situation resulting in an upward movement of the buoyant block pushing the plates right edge up and, due to incompressibility, results in a downward movement of the left side of the plate.

The benchmark is run on a grid of 250 by 55 elements using 25 markers per element. The top boundary has a free surface boundary condition allowing a surface elevation to arise. The two sides of the domain have been prescribed with a free slip boundary condition and the bottom domain with a no slip boundary condition.

Figure 39 shows the surface topography obtained after 7500 yr. A total deflection of 342 m is obtained which is approximately 34 m more than obtained by Choi et al. (2013). This difference is due to the used viscosity for the elastic layer and the model differences: Choi et al. (2013) used a viscosity of 10^{35} Pa s while this study used a viscosity of 10^{25} Pa s. The increased stiffness due to the higher viscosity of the elastic plate from Choi et al. (2013) inhibits the formation of large surface topography. Figure 39b shows the decline in maximum vertical velocity and it can be seen that the velocity converges towards zero approaching a steady state.

Table 4: *Material property values used in the flexure benchmark from Choi et al. (2013).*

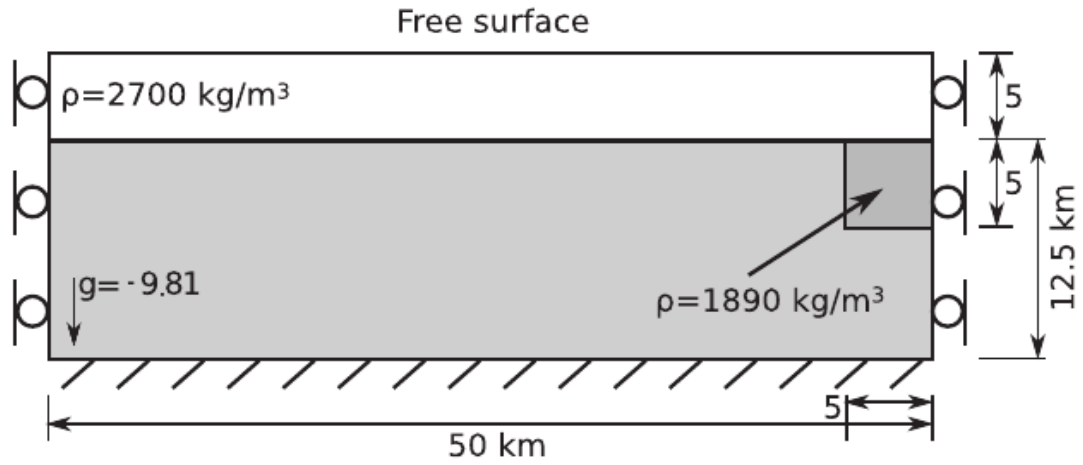| Parameter	Symbol	Elastic plate and inclusion	Viscous mantle
Viscosity	η	10^{25} Pa s	10^{17} Pa s
Density	ρ	2700 kg/m^3 and 1890 kg/m^3	2700 kg/m^3
Elastic shear modulus	μ	30 GPa	10^{50} Pa ($G \to \infty$)

Figure 38: *The set-up for the flexure of an elastic plate benchmark. The viscous mantle (gray) is overlain by a low density inclusion (dark grey) and the elastic plate (white). Adapted from Choi et al. (2013).*
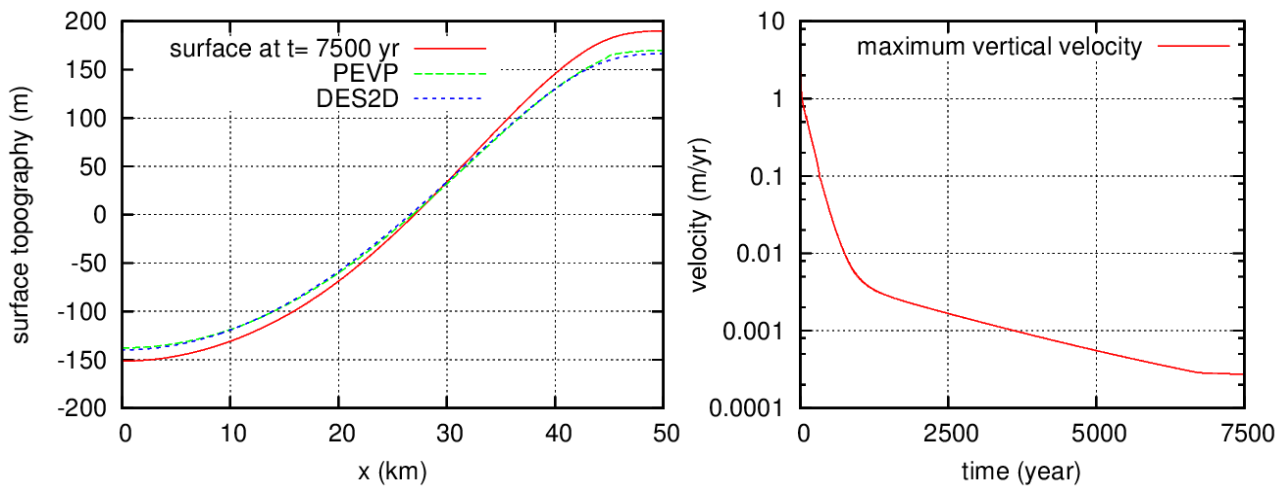

Figure 39: *Left: the surface topography at t= 7500 yrs obtained by this study and the results from Choi et al. (2013) for the incompresisble (PEVP) and nearly incompressible (DES2D) case. Right: the maximum vertical velocity in the domain. (Note the logarithmic scale on the y-axis.)*
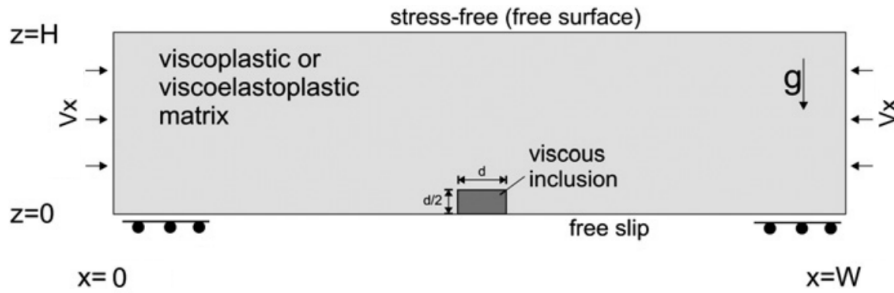
Figure 40: *Set up of the brick benchmark. The model consists of a brick of viscoelastic-plastic material that is compressed. A low viscous heterogeneity is included to localize deformation. From (Kaus, 2010)*

9.4 The brick experiment

In order to test the plasticity implementation, a benchmark called the 'brick experiment' is performed (Hansen, 2003; Popov and Sobolev, 2008; Lemiale et al., 2008; Kaus, 2010; Buiter, 2012). The set-up of this experiment is equal to that used in Kaus (2010) and consists of a block of viscoelastic-plastic material which is subjected to compression (Figure 40). A low viscosity weak zone is included to localize deformation shown in the Figure by the viscous inclusion. The material parameters used in the benchmark are given in Table 5.

A resolution of 400 by 100 is used, a free surface boundary condition is applied on the top boundary and a free slip condition on the lower boundary of the domain. A constant background strain rate $\dot{\varepsilon}$ of 10^{-15} s^{-1} is applied through the compressional velocity condition prescribed as boundary conditions at the sides of the domain.

A von-Mises failure criterion is used where the yield stress is equal to the internal cohesion of the material.

$$\tau_{yield} = C \tag{85}$$

This criterion results in formation of plastic shear bands at an angle of 45 °.

9.4.1 Results

Figure 41 shows the strain rate field that arises during the brick experiment. It can be seen that the shear bands gradually intensify in time until they span from the bottom to the top of the domain. The formed shear bands have an angle of 45° and are very localized.

The results can be compared to results from the viscoelastic-plastic model by Kaus (2010) (Figure 42). It must be kept in mind when comparing these results that the plasticity failure criterion used by Kaus (2010) is a Mohr-Coulomb failure criterion which causes the shear bands to form at a different angle. It must also be noted that Figure 42 shows the second invariant of the strain rate, and not the xx-component.

The results are solely compared to see whether the results match the general expected results which are found in the paper by Kaus (2010). It can be seen that the patterns are roughly similar and that the same order of magnitude in strain rate is reached. Deformation is localized along the shear bands resulting in no deformation outside of the plastic failure zones.

As the results match the anticipated results (correct angle of the shear bands, localized deformation) and globally agree with the results obtained by Kaus (2010), it can be concluded that this benchmark has been performed successfully and that the viscoelastic-plastic implementation is validated for this experiment.

Table 5: *Specifications of the material parameters used in the brick experiment. After Kaus (2010).*

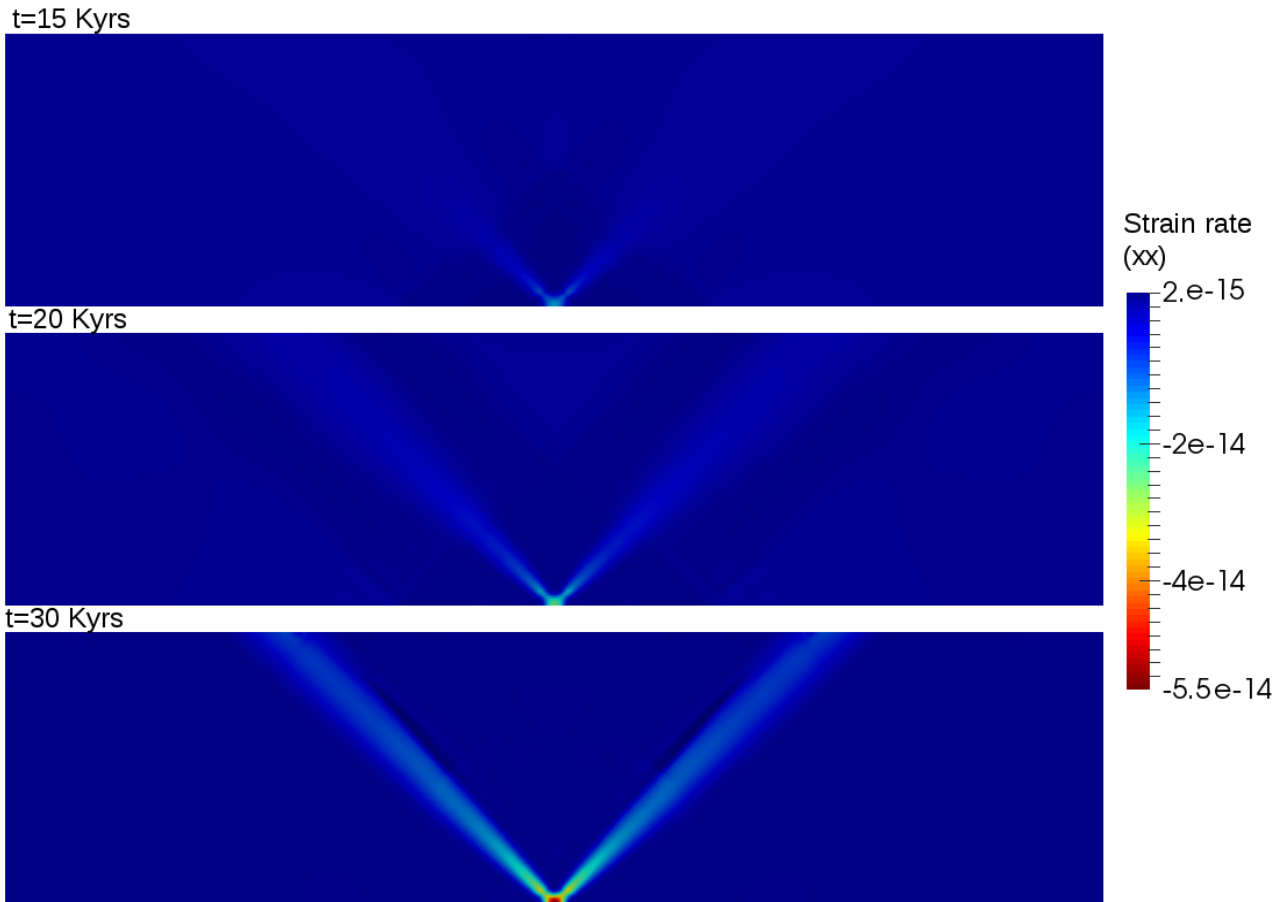| Parameter	Symbol	Prescribed value
Width	W	40 km
Height	H	10 km
Weak inclusion size	d	0.4 x 0.8 km
Gravity acceleration	g_y	-10 m/s
Viscosity of domain	η	10^{25} Pa s
Viscosity of weak seed	η_s	10^{20} Pa s
Density of material and weak seed	ρ	2700 kg/m^3
Elastic shear modulus	μ	5x10^{10} Pa
Initial cohesion	c	40 x 10^6 Pa

Figure 41: *Results of the brick experiment. The xx component of the strain rate ($\dot{\varepsilon}_{xx}$) is given in the domain at t= 10 kyrs , t= 20 kyrs and t= 30 kyrs.*
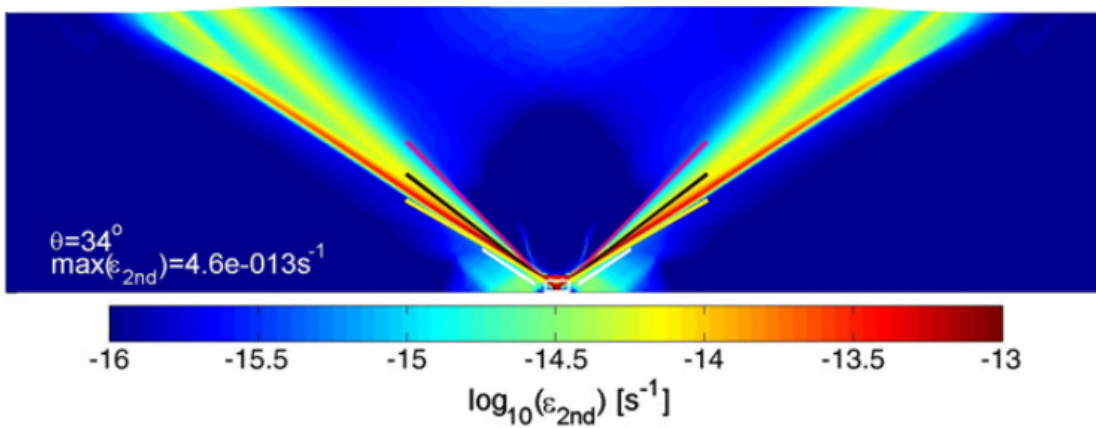

Figure 42: *Result of a compressional brick experiment from Kaus (2010). The second invariant of the strain rate ($\dot{\varepsilon}_{II}$) is given.*
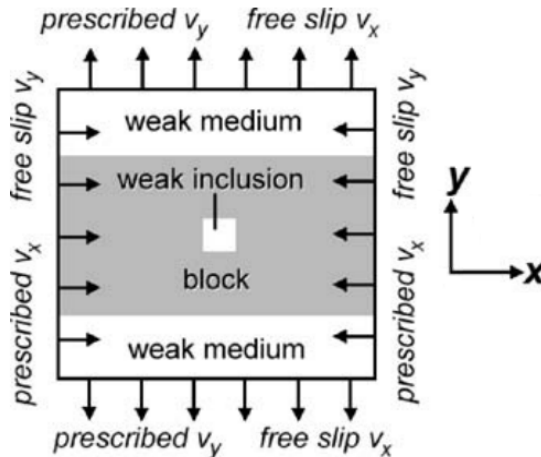
Figure 43: *Set-up of the shortening of a viscoelastic-plastic block benchmark after Gerya (2010). Velocity boundary conditions are applied resulting in a pure shear stress configuration.*

9.5 Shortening of a viscoelastic-plastic block

A second benchmark is done to validate the plasticity implementation. The benchmark is taken from Gerya (2010). The set-up of this benchmark is shown in Figure 43. It consists of a 1000 by 1000 km domain which is stressed under a pure shear configuration under the absence of gravity. The domain consists of a strong material block which is situated between two weak layers and which surrounds a weak inclusion which will accommodate the origin of the arising shear bands. The strong block has a thickness of 600 km and the weak inclusion is situated in the centre with 100 by 100 km dimensions. The used material parameters are given in Table 6. A constant horizontal extension and vertical shortening of of $5 \cdot 10^{-9}$ m s^{-1} is applied. A Von-Mises failure criterion is used (see previous section) resulting in a 45° angle of the arising shear bands.

9.5.1 Results

Our results for this benchmark are shown in Figure 44. The patterns and amplitudes in the results are compliant with the expected results. Narrow shear bands have formed at 45° angles that do not penetrate into the weak medium (right of the Figure). The viscosity in these shear bands (shown on the left) is lower than the viscosity in the surrounding medium that has not undergone yielding.

The results are also very similar to the to the results from Gerya (2010) (Figure 45) The same patterns have emerged with the same viscosity and strain rate. It must be noted however, that the results obtained by this study are much cleaner and smoother and more symmetric. The shear bands that arise and are visible in both figures appear to be more focused in our results. As rocks fail along very narrow faults, it is more realistic to have very focused and narrow shear bands. It can also be seen that the results from this study show less disturbance close to the interface with the weak medium and that the bands visible in the strain rate are more focused and clear.

From the results it can be concluded that this benchmark has been performed successfully and results have been obtained which appear to be better than the results form Gerya (2010). The shear bands are more narrow and focused and less disturbances arise in the surrounding medium that has not reached yielding.

Table 6: *Material property values used in the shortening of a viscoelastic-plastic block from Gerya (2010).*

Parameter	Symbol	Block	Weak medium and inclusion
Viscosity	η	10^{23} Pa s	10^{17} Pa s
Elastic shear modulus	μ	10^{10} Pa	10^{10} Pa
Cohesion	C	10^{7} Pa	10^{10} Pa

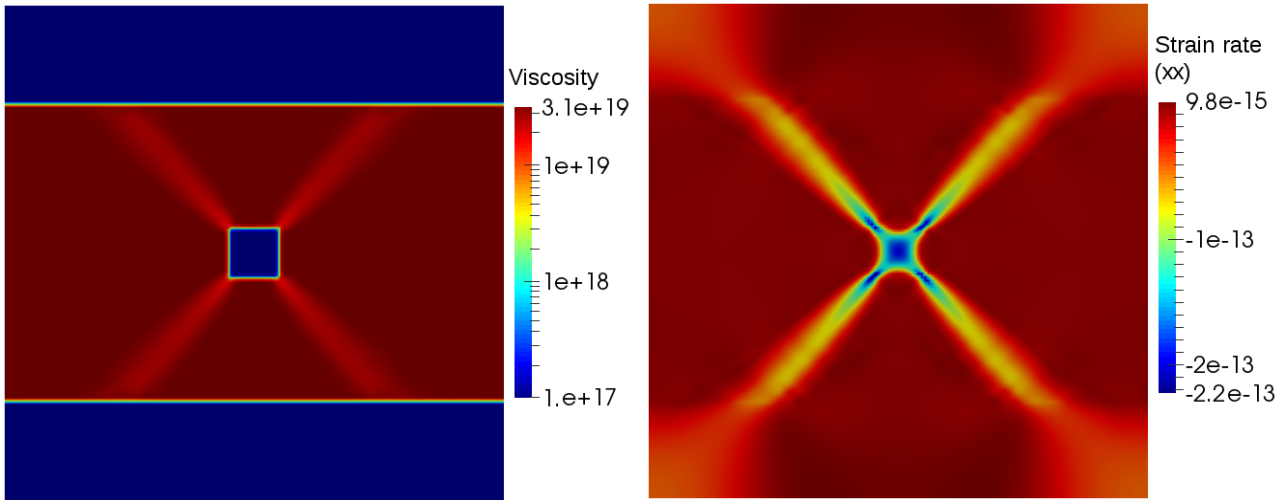**Figure 44:** *Results of the block benchmark obtained in this study at t=2 kyrs. On the left, the (adapted) viscosity is shown, the right shows the xx component of the strain rate.* $\dot{\varepsilon}_{xx}$
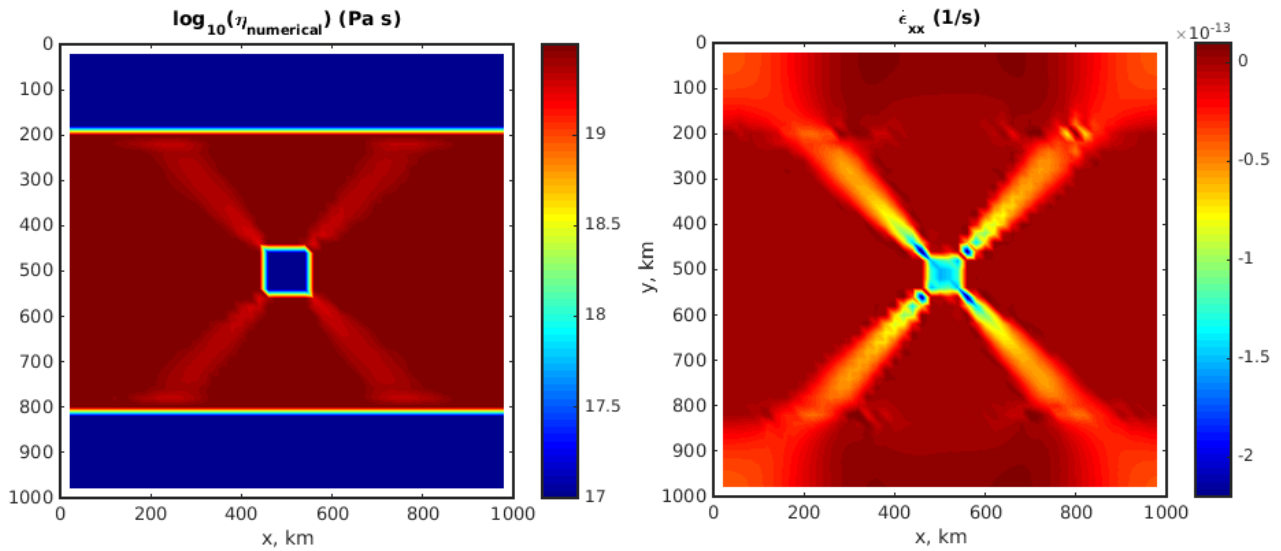

Figure 45: *Results obtained with the code provided by Gerya (2010). The right shows the adapted viscosity (a log scale is used) and on the left the xx component of the strain rate is given* $\dot{\varepsilon}_{xx}$.

63

10 Conclusion

This work contains a thorough documentation on the theory underlying the implementation of elasticity and additionally discusses several numerical points of interest which are bypassed in publications concerning elasticity.

We have shown that it is of utmost importance to use a nodal-based approach (Section 5.1.1): the elasticity implementation produces unstable results when a marker-based approach is adopted. Several additional remarks are made which concern the implementation and which follow from the choice for the nodal-approach. It is important to use nodal properties instead of elemental properties and the interpolation between nodes and markers must be done using incremental values of the stress.

The advantages and disadvantages of implementing elasticity in an existing viscoelastic code have been discussed. From this, it can be concluded that the implementation of elasticity in itself does not pose problems, but that the additional implementational difficulties such as making the code fully nodal may not be forgotten. The dependence of the effective elastic viscosity on the time step also pose problems as the time step has to be chosen from a physical perspective instead of a numerical perspective. The change in viscosity due to this dependence makes it difficult to compare results to viscoplastic models. It is however, of great scientific importance that the influence of elasticity on subduction is further researched and to do this, elasticity has to be more widely available.

From the benchmarks performed in the previous section, it can be concluded that the implementation of elasticity has been successful and that a working viscoelastic-plastic code has been developed.

Furthermore, it has been shown, for the first time, that elasticity can be used in combination with the field advection approach. No research concerning this combination has been done thus far and this novel finding can be used to implement elasticity in codes that do not include markers. These codes were previously thought to not be compatible with elasticity and had to be adapted to include markers. It has been shown that a very simple, first order approach already produces satisfying results indicating that more sophisticated stabilizing methods already present in field-based codes should result in obtaining equal results compared to marker-based codes. As field-based codes are already fully nodal, the difficulties arising when interpolating between markers and nodes do not exist. This makes the implementation of elasticity in a fully functional field-based code easier than a marker based code which has to be adapted to be nodal-based.

This work thus presents an extensive documentation on the theory of viscoelasto-plasticity, the implementation of said rheology and the successfully performed benchmarks. It also presents a novel study towards the combination of elasticity and field-based material tracking methods. It shows that they can be combined and that a very simple, first order approach leads to very promising results. The code developed during this research now includes elasticity and can be used towards researching the influence of elasticity on subduction zones and other geodynamical situations where elasticity might be of importance.

11 Outlook

The viscoelastic-plastic implementation can now be tested further using simple subduction set ups to determine the time step and prescribed material viscosities which lead to the desired lithospheric and mantle-like behaviour. After these simple subduction set ups have been completed, a systematic study towards elasticity on subduction dynamics can be started. This includes, for example, researching its influence on the bending/unbending of the plate, the influence on the subduction velocity, subduction angle and formation of fore bulges.

The elasticity implementation can also be used to research the influence of elasticity in other geodynamically interesting areas and processes such as rifting or on small scale processes.

Regarding the combination of the field-based material tracking method and elasticity, the results of this work are encouraging and recommend the implementation of elasticity in the field-based code ASPECT (Bangerth et al., 2016b). The elastic branch of ASPECT can then be used to perform state of the art research towards mantle and lithosphere dynamics including elastic behaviour.

12 Bibliography

Anderson, J. (1995). Computational Fluid Dynamics. McGraw-Hill.

Bangerth, W., Heister, T., et al. (2016a). ASPECT: Advanced Solver for Problems in Earth's ConvecTion. http://aspect.dealii.org/.

Bangerth, W., Heister, T., et al. (2016b). ASPECT: Advanced Solver for Problems in Earth's ConvecTion. Computational Infrastructure for Geodynamics.

Bello, L., Coltice, N., Tackley, P., Müller, R., and Cannon, J. (2015). Assessing the role of slab rheology in coupled plate-mantle convection models. Earth and Planetary Science Letters, 430:191–201.

Beuchert, M. and Podladchikov, Y. (2010). Viscoelastic mantle convection and lithospheric stresses. GJI, 183:35–63.

Billen, M. (2008). Modeling the dynamics of subducting slabs. Annu. Rev. Earth Planet. Sci., 36:325–356.

Bonnardot, M.-A., Hassani, R., and Tric, E. (2008). Numerical modelling of lithosphere–asthenosphere interaction in a subduction zone. Earth Planet. Sci. Lett., 272:698–708.

Braun, J. (2003). Pecube: a new finite-element code to solve the 3D heat transport equation including the effects of a time-varying, finite amplitude surface topography. Computers and Geosciences, 29:787–794.

Buiter, S. (2012). A review of brittle compressional wedge models. Tectonophysics, 530:1–17.

Capitanio, F. and Morra, F. (2012). The bending mechanics in a dynamic subduction system: Constraints from numerical modelling and global compilation analysis. Tectonophysics, 522:224–234.

Capitanio, F., Morra, G., and Goes, S. (2009). Dynamics of plate bending at the trench and slab-plate coupling. Geochemistry, Geophysics, Geosystems, 10(4).

Choi, E., Tan, E., Lavier, L., and Calo, V. (2013). DynEarthSol2D: An efficient unstructured finite element method to study long-term tectonic deformation. J. Geophys. Res., 118:1–16.

Donea, J. and Huerta, A. (2003). Finite Element Methods for Flow Problems. John Wiley & Sons.

Farrington, R., Moresi, L., and Capitanio, F. (2014). The role of viscoelasticity in subducting plates. Geochemistry, Geophysics, Geosystems, 15(11):4291–4304.

Fourel, L., Goes, S., and Morra, G. (2014). The role of elasticity in slab bending. Geochemistry, Geophysics, Geosystems, 15(11):4507–4525.

Funiciello, F., Morra, G., Regenauer-Lieb, K., and Giardini, D. (2003). Dynamics of retreating slabs: 1. insights from two-dimensional numerical experiments. Journal of Geophysical Research: Solid Earth, 108(B4).

Furuichi, M., Kameyama, M., and Kageyama, A. (2008). Three-dimensional eulerian method for large deformation of viscoelastic fluid: Toward plate-mantle simulation. Journal of Computational Physics, 227(10):4977–4997.

Gerya, T. (2009). Introduction to numerical geodynamic modelling. Cambridge University Press.

Gerya, T. (2010). Numerical Geodynamic Modelling. Cambridge University Press.

Gerya, T. and Yuen, D. (2007). Robust characteristics method for modelling multiphase visco-elasto-plastic thermo-mechanical problems. Phys. Earth. Planet. Inter., 163:83–105.

Hansen, D. (2003). A meshless formulation for geodynamic modeling. J. Geophys. Res., 108:doi:10.1029/2003JB002460.

Harder, H. (1991). Numerical simulation of thermal convection with maxwellian viscoelasticity. Journal of non-newtonian fluid mechanics, 39(1):67–88.

Hughes, T. and Brooks, A. (1982). A theoretical framework for petrov-galerkin methods with discontinuous weighting functions: application to the streamline-upwind procedure. Finite Elements in Fluids, 4:47–65.

Kaus, B. (2010). Factors that control the angle of shear bands in geodynamic numerical models of brittle deformation. Tectonophysics, 484:36–47.

Kaus, B. and Becker, T. (2007). Effects of elasticity on the rayleigh–taylor instability: implications for large-scale geodynamics. Geophysical Journal International, 168(2):843–862.

Lemiale, V., Mühlhaus, H.-B., Moresi, L., and Stafford, J. (2008). Shear banding analysis of plastic models formulated for incompressible viscous flows. Phys. Earth. Planet. Inter., 171:177–186.

Moresi, L., Dufour, F., and Muhlhaus, H. (2002). Mantle convection modeling with viscoelastic/brittle lithosphere: numerical methodology and plate tectonic modeling. Pure and Applied Geophysics, 159(10):2335–2356.

Moresi, L., Dufour, F., and Muhlhaus, H. (2003). A Lagrangian integration point finite element method for large deformation modeling of visco-elastic geomaterials. J. Comp. Phys., 184:476–497.

Moresi, L., Quenette, S., Lemiale, V., Mériaux, C., Appelbe, B., and Mühlhaus, H.-B. (2007). Computational approaches to studying non-linear dynamics of the crust and mantle. Phys. Earth. Planet. Inter., 163:69–82.

Morra, G. and Regenauer-Lieb, K. (2006). A coupled solid–fluid method for modelling subduction. Philosophical magazine, 86(21-22):3307–3323.

Muhlhaus, H. and Regenauer-Lieb, K. (2005). Towards a self-consistent plate mantle model that includes elasticity: simple benchmarks and application to basic modes of convection. Geophysical Journal International, 163(2):788–800.

Popov, A. and Sobolev, S. (2008). SLIM3D: a tool for three-dimensional thermomechanical modelling of lithospheric deformation with elasto-visco-plastic rheology. Phys. Earth. Planet. Inter., 171:55–75.

Ranalli, G. (1995). Rheology of the Earth. Springer.

Royden, L. and Husson, L. (2006). Trench motion, slab geometry and viscous stresses in subduction systems. Geophysical Journal International, 167(2):881–905.

Schellart, W. and Moresi, L. (2013). A new driving mechanism for backarc extension and backarc shortening through slab sinking induced toroidal and poloidal mantle flow: Results from dynamic subduction models with an overriding plate. J. Geophys. Res., 118:1–28.

Schmeling, H., Babeyko, A., Enns, A., Faccenna, C., Funiciello, F., Gerya, T., Golabek, G., Grigull, S., Kaus, B., Morra, G., Schmalholz, S., and van Hunen, J. (2008). A benchmark comparison of spontaneous subduction models - Towards a free surface. Phys. Earth. Planet. Inter., 171:198–223.

Solomatov, V. (2004). Initiation of subduction by small-scale convection. J. Geophys. Res., 109(B01412).

Solomatov, V. and Moresi, L.-N. (1996). Stagnant lid convection on Venus. J. Geophys. Res., 101(E2):4737–4753.

Tezduyar, T. E. and Osawa, Y. (2000). Finite element stabilization parameters computed from element matrices and vectors. Computer Methods in Applied Mechanics and Engineering, 190:411–430.

Thielmann, M. and Popov, B. K. A. (2015). Lithospheric stresses in rayleigh–bénard convection: effects of a free surface and a viscoelastic maxwell rheology. Geophysical Journal International, 203(3):2200–2219.

Thieulot, C. (2011). FANTOM: two- and three-dimensional numerical modelling of creeping flows for the solution of geological problems. Phys. Earth. Planet. Inter., 188:47–68.

Thieulot, C. (2014). ELEFANT: a user-friendly multipurpose geodynamics code. Solid Earth Discussions, 6:1949–2096.

van Keken, P., King, S., Schmeling, H., Christensen, U., Neumeister, D., and Doin, M.-P. (1997). A comparison of methods for the modeling of thermochemical convection. J. Geophys. Res., 102(B10):22,477–22,495.

von Tscharner, M. and Schmalholz, S. M. (2015). A 3-D Lagrangian finite element algorithm with remeshing for simulating large-strain hydrodynamic instabilities in power law viscoelastic fluids. Geochem. Geophys. Geosyst., 16:215–245.

A Implementation of the strain and rotation rate, and the spatial stress derivative

If a viscoelastic rheology is to be implemented in the code, the strain rate and rotation rate are needed to calculate the stress using the viscoelastic expression for the deviatoric stress (86).

$$\boldsymbol{\tau}^{t+\Delta t} = 2\eta_{eff}\, \dot{\boldsymbol{\varepsilon}}^{\,t+\Delta t} + \frac{\eta_{eff}}{\mu\Delta t}\, \boldsymbol{\tau}^t + \frac{\eta_{eff}}{\mu} \left(\boldsymbol{\omega}^t \boldsymbol{\tau}^t - \boldsymbol{\tau}^t \boldsymbol{\omega}^t \right) \tag{86}$$

A.1 Calculating the strain and rotation rate

The strain rate and rotation rate are derivatives of the velocity field. It is impossible to obtain them directly on the nodes since the derivatives of the basis functions are not defined there. In order to calculate the strain and rotation rate on the nodes, an averaging over four surrounding points is used which lie in the vicinity of the considered nodal point (each residing in one of the four surrounding elements). The strain rate is calculated on the surrounding points using the derivatives of the basis functions:

$$\begin{aligned}
\dot{\varepsilon}_{xx} &= \sum_i \frac{\partial N_i}{\partial x} u_i \\
\dot{\varepsilon}_{yy} &= \sum_i \frac{\partial N_i}{\partial y} v_i \\
\dot{\varepsilon}_{xy} &= \sum_i \frac{1}{2}\left(\frac{\partial N_i}{\partial x} v_i + \frac{\partial N_i}{\partial y} u_i \right)
\end{aligned} \tag{87}$$

Here the i denotes the summation over the four nodes using the corresponding velocity component and derivative of the basis function.

The rotation rate is anti-symmetric and thus consists of two components $\omega_{xy} = -\omega_{yx}$. These components are also calculated using the derivatives of the basis functions.

$$\dot{\omega}_{xy} = \sum_i \frac{1}{2}\left(\frac{\partial N_i}{\partial y} u_i + \frac{\partial N_i}{\partial x} v_i \right) \tag{88}$$

A.2 Calculating the spatial stress derivative

When a Eulerian approach is used, as is the case when using compositional fields, the equation for the stress should possibly contain an extra term (see Section (8.3)). This term comes from the advection part in the material derivative. It contains spatial derivatives of the stress tensor.

$$\mathbf{v}\cdot\nabla\boldsymbol{\tau}^t = u^t \begin{pmatrix} \frac{\partial \tau_{xx}^t}{\partial x} \\ \frac{\partial \tau_{yy}^t}{\partial x} \\ \frac{\partial \tau_{xy}^t}{\partial x} \end{pmatrix} + v^t \begin{pmatrix} \frac{\partial \tau_{xx}^t}{\partial y} \\ \frac{\partial \tau_{yy}^t}{\partial y} \\ \frac{\partial \tau_{xy}^t}{\partial y} \end{pmatrix} \tag{89}$$

These spatial derivatives are calculated using the same approach used to calculate the strain rates. As an example, the two spatial derivatives for τ_{xx} are given.

$$\begin{aligned}
\frac{\partial \tau_{xx}^i}{\partial x} &= \sum_i \frac{\partial N_i}{\partial x} \tau_{xx}^i \\
\frac{\partial \tau_{yy}^i}{\partial y} &= \sum_i \frac{\partial N_i}{\partial y} \tau_{xx}^i
\end{aligned} \tag{90}$$

Here the i denotes the summation over the four nodes using the corresponding stress component and derivative of the basis function. Because the derivatives of the basis functions are unknown directly on the nodal point, the same approach is used as done for the strain and rotation rate. The spatial derivatives are calculated on four points which surround the nodal point (one in each element connected to the nodal point) after which the average is calculated.